

Signatures of chaos and integrability in isolated and  
open quantum many-body systems, and controlling  
chaos in the Kicked Top model

A Thesis

Submitted to the  
Tata Institute of Fundamental Research, Mumbai  
Subject Board of Physics  
for the degree of Doctor of Philosophy

by

Mahaveer Prasad

International Centre for Theoretical Sciences  
Tata Institute of Fundamental Research

September, 2024

Final Version Submitted in January, 2025



# Declaration

This thesis is a presentation of my original research work. Wherever contributions of others are involved, every effort is made to indicate this clearly, with due reference to the literature, and acknowledgement of collaborative research and discussions.

The work was done under the guidance of Professor Manas Kulkarni at the International Centre for Theoretical Sciences, Tata Institute of Fundamental Research (ICTS-TIFR), Bangalore.



**Mahaveer Prasad**

In my capacity as the formal supervisor of record of the candidate's thesis, I certify that the above statements are true to the best of my knowledge.



**Professor Manas Kulkarni**

Date: January 28, 2025



*Dedicated to*

*My parents, my brother, and all Indian farmers.*



# Acknowledgements

First and foremost, I would like to express my deepest gratitude to my PhD advisor, Prof. Manas Kulkarni, for his invaluable guidance, and continuous support throughout my research journey. His enthusiasm consistently inspired me to put in continuous effort and explore a wide range of research problems.

I had the privilege of closely collaborating with Hari Kumar Yadalam, Abhishodh Prakash, and Justin Wilson. Through this experience, I gained valuable insights into various aspects of our research projects and acquired important numerical tools. I am also thankful to my other collaborators: Jedediah H. Pixley, Camile Aron, Sriram Ganeshan, Thomas Iadecola, and Ahana Chakraborty.

I would like to extend my gratitude to all the members of ICTS-TIFR, especially those in the statistical physics and condensed matter groups, for the insightful discussions and interactions that enriched my research.

I would like to acknowledge my Batchmates/friends: Ankush, Bhanu, Harshit, Anup, Souvik, Uddippata, Omkar, Tuneer, Mukesh, and Priyadarshi for their help during coursework, as well as their support with both academic and non-academic matters.

I am profoundly grateful to my brother Kamal, whose support has been unwavering and who played a key role in sparking my interest in physics and mathematics during my school years.

I deeply appreciate my dear friends: Mohit Mudgal, Divya Sahani, Aman Kaushik, Mintu, and many others, who have played a significant role in shaping who I am today. I would also like to thank my teachers, parents, and everyone who has inspired and guided me along the way.

Special thanks to my football and Kungfu martial arts buddies at ICTS: Basudeb, Ashik, Sarath, Sukan, Atharva, Nirnoy, Irshad, Saikat, Chandru, Sibaram, Ikbal, Subham, Jyotirmoy and others. Being around them has taught me invaluable lessons about teamwork and the spirit of the game (and life). I'm truly grateful to them for bringing extra energy and joy into my life.



# List of Figures

2.1	SFF for GOE ensemble shown in Eq. (2.18) with $N=1000$ . The separation between dip, ramp, and plateau regimes is schematically indicated using dotted lines. . . . .	15
2.2	Left: SFF for Poisson levels shown in Eq. (2.23). Right: The power-law scaling form for $\tau_T < \tau < \tau_H$ is exposed by subtracting the saturation value of $N$ (chosen to be 1000 for both plots). . . . .	16
2.3	(a) DOG [Eq. (2.25)] for the eigenvalues of GOE matrices compared with analytical expression in Eq. (2.31). (b) DOG [Eq. (2.25)] of Poisson levels compared with analytical expression in Eq. (2.34). The insets show the same figure restricted to positive values with the x-axis in log scale to clarify the behavior near the origin. The plot for each $N$ is generated using 5000 levels with mean level spacing $\mu = 1$ . . . . .	19
3.1	Scatter plot of the complex spectrum of the Liouvillian $\mathcal{L}$ of the dissipative Dicke model for $S = 10$ and $\omega_c = \omega_s = \kappa = 1$ for which $\lambda^* = 1/\sqrt{2}$ . (a) Normal phase, $\lambda = 0.2$ . (b) Superradiant phase, $\lambda = 1.0$ . A stark difference in the structure of the spectrum above and below the critical point can be observed. . . . .	26
3.2	Level-spacing distribution of the complex spectrum of the Liouvillian $\mathcal{L}$ in (a) normal phase with $\lambda = 0.2$ , and (b) superradiant phase with $\lambda = 1.0$ . We find remarkable agreement with the $2D$ Poisson distribution $p_{2D-P}(s)$ given in Eq. (2.6) and that of the GinUE RMT prediction $p_{\text{GinUE}}(s)$ given in Eq. (2.7) in the normal phase and in the superradiant phase, respectively. . . . .	28

- 3.3 The metric  $\eta$  defined in Eq. (3.10) as we increase the coupling  $\lambda$  from the normal phase to the superradiant phase. It shows the crossover of the complex-eigenvalue spacing distribution from integrable ( $\eta \sim 0$ ) to RMT ( $\eta \sim 1$ ) predictions. The crossover sharpens as we increase the system size. At  $\lambda = 0$  the dissipative cavity decouples from the spin. Hence, the spectrum is expected to display pathological statistics away from any universal behavior. This explains the observed discrepancies close to  $\lambda = 0$ . 29
- 3.4 Scatter plot of the complex level-spacing ratio  $z$  introduced in Eq. (3.11) for  $S = 10$  (a) in the normal phase,  $\lambda = 0.2$ , and (b) in the superradiant phase,  $\lambda = 1.0$ . The table gives  $\langle \cos \theta \rangle$  and  $\langle r \rangle$  for a range of  $\lambda$  values, along with their prediction from the  $2D$  Poisson distribution and GinUE RMT. . . . . 30
- 3.5 Scatter plot of the Liouvillian spectrum of the dissipative Dicke model for different  $n_{\text{cutoff}} = 20, 30, 40$  in (a) the normal phase,  $\lambda = 0.2$  and (b) the superradiant phase,  $\lambda = 1.0$  ( $S = 10$ ). . . . . 31
- 3.6  $\langle \cos \theta \rangle$  and  $\langle r \rangle$  versus  $n_{\text{cutoff}}$ , computed from the consecutive complex level-spacing ratio distribution of  $z$  introduced in Eq. (3.11) ( $S = 10$ ). . . 31
- 4.1 Tavis-Cummings lattice (TCL): Tavis-Cummings units hosted on a one-dimensional tight-binding lattice of size  $L$  with open boundary conditions. Each unit features a large spin  $S$  coupled to a bosonic mode via the interaction  $\lambda$ .  $J$  sets the hopping amplitude of the bosons between neighboring units. See the Hamiltonian in Eq. (4.1). . . . . 34
- 4.2 Distribution of level spacings  $p(s)$  in the crossover regime from integrability to chaos (left to right). The top panel is computed from the exact diagonalization of the Tavis-Cummings lattice ( $L = 3$  sites) with spin  $S = 8$ , for (a)  $J/\lambda = 0.02$ , (b)  $J/\lambda = 0.15$ , (c)  $J/\lambda = 0.22$  and (d)  $J/\lambda = 1.0$ . The bottom panel is computed from the corresponding impurity model with  $S = 64$  and  $\lambda = 1$ , for (e)  $\mu = 0.1$ , (f)  $\mu = 0.65$ , (g)  $\mu = 1.09$  and (h)  $\mu = 1.8$ . The red curves correspond to fits to the Brody distribution defined in Eq. (4.3), with the single fitting parameter  $b$  given in the legend. The values of the impurity  $\mu$  are chosen such that  $b$  is the same between the lattice and the impurity. . . . . 38

4.3 Adjacent gap ratio  $\langle r \rangle$  in the crossover regime from integrability to chaos. (a) Tavis-Cummings lattice ( $L = 3$  sites) as  $J/\lambda \times S^{1/4}$  is tuned from weak to strong hopping. (b) Corresponding impurity model as a function of the drive  $\mu \times S^{3/4}$  for fixed  $\lambda = 1$ . Other choices of  $\lambda$  yield similar results. The collapse of the different curves is used to identify the dynamic scaling with respect to local spin size  $S$ . . . . . 39

4.4 Map between the integrability-breaking parameters of the lattice and impurity models,  $J/\lambda$  and  $\mu$ , respectively. The scalings with  $S$  on both axis are deduced from the dynamic scalings identified in Fig. 4.3. The map is numerically extracted from the level-spacing Brody parameters  $b$  determined in Fig. 4.2 as well as from the data of the adjacent gap ratio  $\langle r \rangle$  of Fig. 4.3. The methodology is explained in Section [4.3.3].  $L = 3$  and  $S = 8$  on the lattice side and the different impurity spin sizes are given in the legend. . . . . 41

4.5 Spectral form factors of the lattice model with  $L = 3$  and  $S = 8$  and of the impurity model with  $S = 64$  for increasing values of the integrability-breaking parameters  $J/\lambda$  (lattice) and  $\mu$  (impurity) given in the legends and chosen as in Fig. 4.2. The plain and dashed black lines correspond to the Poisson and GOE distributions, respectively. . . . . 42

4.6 Poincaré sections of the classical driven impurity model defined in Eq. (4.9) in the limit  $S \rightarrow \infty$ ,  $\lambda = 1.0$ , and for various energies  $E$  and (top) weak drive  $\mu = 0.1$ , (middle) intermediate drive 1.8, (bottom) strong drive 10.0. Different colors represent trajectories with different initial conditions . . . 45

5.1 Top row: SFF [Eq. (2.16)] for  $N = 20$  levels across various disorder strengths. Bottom row: Reduced SFF deep in the MBL phase with power-law scaling. Plots in left, middle and right columns correspond to the disordered spin chain (D), Floquet spin chain (F) and quasi-periodic spin chain (Q) defined in Eqs. (5.1, 5.2, 5.6) respectively. System sizes used are (from left to right)  $L = 14, 10, 12$  for the top row and  $L = 18, 12, 16$  for the bottom row. The disorder strengths used for the bottom row is (from left to right)  $W = 25$ ,  $\Gamma = 0.01$  and  $W = 15$ . . . . . 49

5.2 DOG [Eq. (2.25)] plots deep in the ergodic phase (top row) and the MBL phase (bottom row) for (from left to right) the disordered spin chain (D), the Floquet spin chain (F) and the quasiperiodic spin chain (Q) defined in Eqs. (5.1, 5.2, 5.6) respectively, compared to the analytical expressions in Eqs. (2.31, 2.34) (dotted lines).  $N = 20$  levels drawn from the middle of the spectrum and rescaled to set mean level spacing at unity, and plotted the numerical data with positive values of gaps with the log scale on x-axis. The system sizes used are (from left to right)  $L = 12, 10, 12$ . . . . . 52

5.3 (Top row) Plots of the adjacent gap ratio  $\langle r \rangle$  and (Bottom row) rescaled density of zero gaps ( $N\chi(0, N)$ ) across various strengths and sizes of the system used to locate the approximate strength of the critical disorder (dashed line) where the curves for different sizes of the system cross for (from left to right) the disordered spin chain (D), Floquet spin chain (F) and quasi-periodic spin chain (Q) defined in Eqs. (5.1, 5.2, 5.6) respectively. The estimate of the critical disorder computed from  $\langle r \rangle$  and  $N\chi(0, N)$  agrees for all models. The full spectrum used for the plots in the top row and  $N = 20$  levels drawn from the middle of the spectrum used for plots in the bottom row. . . . . 53

5.4 Left: Persistent oscillations seen in the density of states of the full  $S_z = 0$  spectrum. Right: SFF [Eq. (2.16)] plotted for levels drawn from the middle of the  $S_z = 0$  sector of the spin chain with quasi-periodic local field [Eq. (5.6)] deep in the MBL phase ( $W = 15$ ). These oscillations remain unchanged with increased disorder averaging, but decrease in amplitude with increase in system size. . . . . 54

5.5 DOS (top row) and the reduced SFF (bottom row) for Poisson numbers generated as described in Eq. (2.20) (left column), Poisson numbers generated in Eq. (2.20) with random offset to soften the DOS edges, shown in Eq. (5.10) (middle column) and levels chosen from the disordered Hamiltonian Eq. (5.1) ( $L = 18$ ) deep in the MBL phase ( $W = 25$ ). . . . . 55

5.6 Left: The reduced filtered SFF Eq. (5.15) for  $N = 80,000$  Poisson numbers generated as shown in Eq. (2.20) averaged over 50,000 disorder samples. Right: Plot of modified coefficient of the power-law scaling  $\alpha$ , defined in Eq. (5.18) for various  $\eta$ . It is clear that  $\alpha(\eta)$  has no dependence on  $N$ . 58

5.7 Left: Reduced SFF for  $N = 1000$  fixed levels selected from unfolded  $N_R$  Poisson numbers generated as shown in Eq. (2.20) averaged over 400,000 disorder samples. Right: RMS deviation of the SFF  $\Sigma$  from the power law scaling form, defined in Eq. (5.19) calculated with the data points in the window  $\tau \in [\frac{3}{\sqrt{N}}, 0.2]$ . The power-law scaling form is absent when  $\frac{N}{N_R} \sim 1$  and is recovered at the limit  $\frac{N}{N_R} \sim 0$ . . . . . 60

5.8 Left: DOG [Eq. (2.25)] for the disordered spin chain model Eq. (5.1) in the MBL phase with disorder strength  $W = 15$  computed with  $N = 20$  energy levels drawn from the middle of the spectrum plotted on a log scale to capture the dip at the origin. The DOG approaches the form predicted by Poisson numbers Eq. (2.34) with an increase in system size. Right: Rescaled density of zero gaps ( $N\chi(0, N)$ ) versus binning size. This vanishes for small bin and system size and approaches the value of 1 predicted using Poisson numbers with an increase in bin and system size. 61

6.1 Density plots of trajectories of the Kicked Top model in the  $\theta - \phi$  phase plane with control map [Eq. (6.5)] with probability  $p = 0.0, 0.1, 0.2, 0.3, 0.5,$  and  $0.7$  (left to right). Parameters  $k = 6, a = 0.5$  are taken for the numerical computation, and data is generated over 1000 time steps. . . . . 66

6.2 (Left) The plot of  $O^2$  as defined in Eq. (6.6) is the measure of the steady-state value of square deviation from the fixed point  $t \rightarrow \infty$  and (Right) Lyapunov exponent  $\lambda$  as defined in Eq. (6.7) with respect to control probability  $p$  for various value of  $a$ . For numerical computation, kicking strength  $k = 6$  and control map parameter  $a = 0.5$ . . . . . 68

6.3 (Left) Uncontrolled-controlled phase diagram in the  $a - p$  plane with the distance measure  $O^2$  [Eq. (6.6)] (color bar) of the chaotic Kicked top model ( $k = 6$ ) with control map. (Right) Uncontrolled-controlled phase diagram in the  $k - p$  plane with the distance measure  $O^2$  of the Kicked top model with control map ( $a = 0.5$ ). Uncontrolled and controlled phases are separated by estimated critical points  $p_c(O^2 = 0)$  and  $p_c(\lambda = 0)$  that are computed from the  $O^2$  and  $\lambda$  data respectively. . . . . 69

A.1	Density of states (DOS) of the Tavis-Cummings Lattice [Eq. (4.1) in the main text]. (Left panel) Before unfolding. (Right panel) After unfolding. Spectra are computed in the reflection-symmetric sector with $L = 3$ , $S = 8$ , $N_{\text{ex}} = 36$ , and $\lambda = 1.0$ for (a, b) weak hopping $J/\lambda = 0.02$ , and (c, d) strong hopping $J/\lambda = 1.0$ . . . . .	74
D.1	Plots of $N\chi(0, N)$ for the disordered spin chain Eq. (5.1) versus disorder strength $W$ computed using different number of bins to construct histograms. Data averaged over 50000, 30000, 20000, 5000 disorder samples for system sizes $L = 10, 12, 14, 16$ respectively. The estimate for critical disorder strength $W^*$ (dashed line) corresponding to the location where curves of different system sizes cross is unchanged with binning sizes. $N = 20$ levels used from middle of spectrum of each disorder sample and scaled to set mean level spacing to unity. . . . .	85

# Contents

<b>Acknowledgements</b>	<b>v</b>
<b>Abstract</b>	<b>0</b>
<b>1 Introduction</b>	<b>1</b>
<b>2 Quantum chaos, random matrix theory, and spectral statistics tools</b>	<b>7</b>
2.1 RMT and quantum chaos/integrability conjectures . . . . .	8
2.1.1 BGS conjecture . . . . .	9
2.1.2 Berry-Tabor conjecture . . . . .	10
2.1.3 GHS conjecture . . . . .	10
2.2 Adjacent gap ratio . . . . .	11
2.3 Spectral form factor . . . . .	13
2.3.1 The spectral form factor for random matrices . . . . .	15
2.3.2 The spectral form factor for Poisson numbers . . . . .	16
2.4 Density of all gaps . . . . .	18
2.4.1 Density of all gaps for random matrices . . . . .	19
2.4.2 Density of all gaps for Poisson numbers . . . . .	20
2.5 Eigenstate Thermalization Hypothesis . . . . .	20
<b>3 Dissipative quantum dynamics, phase transitions, and non-Hermitian random matrices</b>	<b>23</b>
3.1 Dissipative Dicke model . . . . .	23
3.1.1 Computing the spectrum of the dissipative Dicke Liouvillian . . . . .	25
3.2 Spectral statistics of complex spectra of Liouvillian . . . . .	25
3.2.1 Spacing statistics of complex eigenvalues . . . . .	27

3.2.2	Complex-plane generalization of the consecutive level-spacing ratio	29
3.2.3	Convergence of the statistical properties of the spectrum with respect to the cavity cutoff . . . . .	31
3.3	Summary of results and conclusions . . . . .	32
<b>4</b>	<b>Transition to chaos in extended systems and their quantum impurity models</b>	<b>33</b>
4.1	Tavis-Cummings Lattice (TCL) . . . . .	34
4.2	Impurity model . . . . .	36
4.3	Spectral properties . . . . .	37
4.3.1	Level-spacing statistics . . . . .	37
4.3.2	Adjacent-gap ratio . . . . .	39
4.3.3	Map between lattice and impurity models . . . . .	40
4.3.4	Spectral form factor . . . . .	41
4.4	Chaos in the classical limit of Impurity model . . . . .	43
4.5	Summary of results and conclusions . . . . .	46
<b>5</b>	<b>Long-ranged spectral correlations in eigenstate phases</b>	<b>47</b>
5.1	Numerical study of physical models . . . . .	48
5.1.1	Physical models . . . . .	49
5.1.2	Summary of results . . . . .	52
5.2	On the universality and robustness of spectral signatures in the MBL phase	54
5.2.1	Deforming the global density of states . . . . .	56
5.2.2	Filtering the SFF formula . . . . .	57
5.2.3	Unfolding the spectrum . . . . .	59
5.3	Discussion . . . . .	60
5.3.1	The effect of many-body resonances in the MBL phase . . . . .	60
5.3.2	Symmetry breaking picture for delocalization . . . . .	62
<b>6</b>	<b>Stochastic control of chaos in Kicked Top model</b>	<b>63</b>
6.1	Classical Kicked Top model . . . . .	63
6.1.1	Chaos-Control Dynamics . . . . .	65
6.1.2	Observables . . . . .	67
6.2	Classical Control Transition . . . . .	68
6.2.1	Phase Diagram . . . . .	69

Conclusion	72
Appendix A Unfolding the spectrum	73
Appendix B Mean-field relation between lattice and impurity spectral form factors	75
Appendix C DOS effects on the connected SFF for Poisson numbers	81
Appendix D Sensitivity of $\chi(0, N)$ data on binning size	85
Appendix E Numerical parameters used to produce main text figures	87
Bibliography	89
List of publications	111

# Abstract

This thesis presents work on chaos and integrability in isolated and open quantum many-body systems and an attempt to control the classical chaotic dynamics stochastically. Quantum chaos is a rapidly growing field aimed at understanding the behavior of complex quantum systems, closely tied to both equilibrium and non-equilibrium phenomena like thermalization and non-thermal phases such as many-body localization (MBL). We mainly focus on investigating such properties with the spectral statistics diagnostics of the dynamics governing operators of such systems. We consider the dissipative Dicke model, an archetype of symmetry-breaking quantum phase transitions, and demonstrate that the Liouvillian, which describes the quantum dynamics, exhibits distinct spectral features indicative of integrable and chaotic behavior across the critical point of transition. We study its connections to non-Hermitian random matrices. We also discuss the integrability and chaotic features in the extended version of the Tavis–Cummings model on a finite chain. Furthermore, we identify a single-site impurity model that successfully captures the spectral properties of the lattice model. We also present some analytical and numerical results on long-range non-local spectral correlations: Spectral form factor (SFF), and density of all gaps (DOG). We discuss their utility in characterizing and distinguishing phases such as ergodic/chaotic and many-body localized systems. These quantities (SFF and DOG) furnish unique signatures that can identify two phases. We demonstrate this by numerically studying three one-dimensional quantum spin chain models with (i) quenched disorder, (ii) periodic drive (Floquet), and (iii) quasiperiodic detuning. Finally, we explore the stochastic control of chaos in the Kicked Top model. This leads to the emergence of controlled and uncontrolled phases, depending on the rate of control application on the chaotic dynamics. We present phase diagrams that illustrate the relationship between chaos and control parameters and estimate the critical transition point using observables such as square deviation and the Lyapunov exponent.

# Chapter 1

## Introduction

Integrability and chaos are distinct dynamical features of classical systems [1–10], characterized by phase space trajectories and typically diagnosed by the Lyapunov exponent [5, 9, 11–13]. Integrability in a system is reflected from an extensive number of conserved quantities and is associated with regular, closed-orbit trajectories in phase space. Chaos in classical dynamics arises due to non-linearity in the systems and strong sensitivity to initial conditions. It is natural to ask what happens when the system is quantum mechanical, where the dynamics is unitary and determined by linear operations on the quantum state. How these features of chaos in classical dynamics are mirrored when the system behaves as quantum mechanical? To address such questions, the field of quantum chaos [1, 14–19] emerged to explore the quantum manifestations of classical chaotic dynamics and has mainly focused on the time-independent one-body system case (few degrees of freedom). Understanding quantum chaos is not only fundamentally important but also provides insights into the classical limit of a quantum system. In recent years, quantum chaos has become an increasingly relevant topic, particularly concerning the important and challenging problems of thermalization [20–22] and the study of non-equilibrium phenomena such as localization-delocalization [23–25] in quantum systems.

Several attempts have been made to understand and characterize the integrability and chaos in quantum systems [19, 26]. Spectral statistics that capture spectral fluctuations or correlation of spectra of the dynamics-governing-operator such as Hamiltonian of the isolated system was first proposed as an effective probe for quantum systems that generically exhibit these two distinct behaviors in the classical limit. Berry and Tabor

conjectured [27] that spectra of Hamiltonian of generic integrable systems behave like uncorrelated random numbers and distribution of their nearest neighbor gaps follow one-dimensional Poisson distribution. Later Bohigas, Giannoni, and Schmit (BGS) [28] proposed a conjecture for chaotic systems that relates it to random matrix theory (RMT), according to which, the nearest neighbor level spacings of generic chaotic systems overlap with random matrix statistics depending on the symmetry class of the Hamiltonian of the system. Consequently, in the context of open quantum systems, Grobe, Haake, and Sommers extended this analysis and established the GHS conjecture [29], according to which signatures of integrability and chaos can be found in the spectral statistics of dynamics-governing-operator Liouvillians  $\mathcal{L}$  for Markovian dissipative systems. If the corresponding classical dynamics are integrable, the complex level spacings of the spectra of  $\mathcal{L}$  are distributed according to the two-dimensional ( $2D$ ) Poisson distribution. Conversely, if the systems have chaotic classical limits, they follow the predictions from non-Hermitian RMT corresponding to appropriate classes of the Ginibre ensembles. Later it was found that these conjectures also hold for quantum many-body systems [30–39] not having well defined classical limit and recently these approaches have been adopted to study non-hermitian systems [40–42]. Out-of-time-order correlator (OTOC) [43–46] is also proposed as a measure of quantum chaos to bridge the gap between classical and quantum systems. Generic many-body quantum systems are expected to be chaotic. Quantum chaos, both in isolated and open systems, is usually characterized by comparing the spectral properties of the time evolution generator ( $H$  for isolated and  $\mathcal{L}$  for open systems) to the universal predictions of RMT with systematic symmetry classification, within a framework known with these conjectures of quantum chaos and OTOC.

One of the fundamental questions in statistical mechanics focuses on how and when a system reaches thermal equilibrium (thermalization) from the dynamics of isolated many-body systems. In classical systems, where dynamics is described by the Hamiltonian, thermalization is well understood [47–49]. In quantum many-body systems, there are active attempts to understand how an isolated quantum many-body system under unitary dynamics reaches the thermal equilibrium state [20,50,51]. The Eigenstate Thermalization Hypothesis (ETH) [20] is formulated to find when and how isolated quantum many-body systems reach thermal equilibrium and such systems can be described with quantum statistical mechanics. ETH is a remarkable tool for making progress in the understanding of equilibrium and non-equilibrium phases of quantum many-body systems. Systems that satisfy ETH are said to be quantum chaotic or ergodic whose eigenstates

are highly (volume-law) [52] entangled and eigenvalues are correlated due to level repulsion and many important results can be derived with its correspondence with RMT. The memory of the initial state is washed out in the long-time evolution under the dynamics of such systems due to the underlying chaotic/ergodic nature of the system. Recently it has been found in numerical and experimental studies that there are specific kinds of settings of disordered interacting systems called many-body localized (MBL) systems [53–57], integrable [58–60], and quantum many-body scars [61, 62] violate ETH and these systems fail to reach thermal equilibrium. In the MBL phase, systems retain the memory of the initial state of the system in the long time dynamics. Probing and testing the validity of such non-equilibrium phases of quantum matter in the thermodynamic limit with currently available numerical tools is an active area of research and experiments on ultra-cold atomic gases [63–65], trapped ions [66], superconducting qubits [67, 68] and nuclear spins [69] have provided evidence for the existence of the MBL phase.

Several probes are introduced to find the signature of these phases (ergodic and MBL) in the numerical study of such systems. Spectral analysis [70] of such systems shows distinct features and estimates ergodic-MBL transition points. For ergodic (chaotic) systems, eigenvalue correlations are reproduced by an appropriate random matrix ensemble [17]. These are manifested in local probes such as the Wigner–Dyson distribution of spectral gaps as well as in nonlocal, long range probes such as the spectral form factor (SFF) which shows a robust, universal linear ‘ramp’ and has been the subject of many recent studies [71–77]. MBL systems, on the other hand, exhibit emergent integrability characterized by an extensive number of local integrals of motion and an energy spectrum that behaves like numbers drawn from a Poisson process [78–82]. While Poisson signatures in MBL systems have been studied in local probes such as the distribution of nearest-neighbor spectral gaps and adjacent gap ratios [79]. Recently, it was also shown that long-range spectral probes that measure correlations across the spectrum, such as the SFF, could also exhibit a unique scaling form in the MBL phase [83, 84]. Interestingly, this has also been shown to be present in integrable quantum-mechanical systems such as integrable billiards [85].

From a technological standpoint, chaos imposes fundamental limits on quantum information processing. Maintaining the coherence of the quantum state is highly desirable for loss-free information processing. In the modern era of quantum technology, effectively preparing systems to perform this task remains a challenge [86–91], as nearly all

quantum many-body systems are chaotic by nature. Recent interest in quantum information and computation has focused on exploring properties that preserve the quantum state from decoherence or information loss. Identifying integrable regimes in quantum many-body systems could be beneficial for achieving these goals. Significant progress has been made in incorporating increasingly controllable quantum degrees of freedom in quantum hybrid devices [92–103]. Additionally, studying extended quantum systems numerically using exact diagonalization is challenging because the Hilbert space dimension grows exponentially with the system size. This exponential growth makes it difficult to analyze larger systems with current state-of-the-art computational facilities. Developing effective methods and strategies to overcome these challenges is therefore crucial. To address this difficulty, we seek a minimal quantum impurity model that can reproduce the spectral features of the lattice problem at a lower computational cost.

Controlling chaotic dynamics in both classical and quantum regimes has been an active area of research. In classical dynamical systems, there exist both deterministic and stochastic protocols [104–106] to control chaotic dynamics and to steer the system to a desired final state thereby negating the effects of exponential sensitivity to the infinitesimal perturbations. With the advent of numerous noisy intermediate-scale quantum devices, this problem of controlling chaotic dynamics has found a new context where the goal is to find robust mechanisms for steering the dynamics to desired quantum states. An important step in this direction has manifested in the form of the out-of-equilibrium measurement-induced phase transition (MIPT), which is a transition from a volume law scaling entanglement to the areal law scaling as a function of the rate of measurements. In a recent work [107], it has been shown that a stochastic control protocol of a classically chaotic system, dubbed probabilistic control of chaos, possesses several features of the MIPT once feedback is included in the quantum dynamics. This approach allows us to view the classical and quantum control endeavors through a common lens thereby enabling us to import techniques developed in classical dynamical systems to the field of quantum control. These developments have resulted in a general framework of quantum adaptive dynamics where measurements and feedback can be employed to stabilize a desired quantum many-body phase. An interesting question in these studies is what are the fundamental similarities and differences between the control transition manifesting in the classical regime as compared to its quantum counterpart? To address these questions, we consider the stochastic control of Kicked Top model, which is a paradigmatic model for quantum chaos with a well-defined classical and semiclassical limit.

**This thesis contains four pieces of work and is organized as follows:**

Chapter [2] is focused on introducing and reviewing all the essential tools and diagnostics of spectral statistics such as nearest neighbor spacing, level spacing ratio, and SFF that are used for the study and characterization of chaos and integrability in isolated and open quantum systems and as well in the MBL physics. In this chapter we also review some RMT results that we will use later part of the thesis. We also present our original results on DOG in Section [2.4]. In Chapter [3], we discuss our work on the dissipative Dicke model to identify integrable to chaotic transition across dissipative quantum phase transition by analyzing the spectra of the Lindbladian of this model. In Chapter [4] we consider an extended version of the Tavis–Cummings model on a finite chain. We study a minimal single-site quantum impurity model that effectively captures the spectral properties of the lattice system, addressing the computational challenges posed by the large Hilbert space in such studies. By studying spectral statistics of the lattice model and the corresponding impurity model we observe the transition from integrability to chaos as the hopping between the Tavis–Cummings sites and drive term in the corresponding impurity model increases above a finite value. In Chapter [5] we study non-local measures of spectral correlations and their utility in characterizing and distinguishing between the distinct eigenstate phases of quantum chaotic and many-body localized systems. We focus on two related quantities, the spectral form factor and the density of all spectral gaps, and show that they furnish unique signatures that can be used to sharply identify the two phases. We investigated three one-dimensional quantum spin chain models: (i) with quenched disorder, (ii) under periodic driving (Floquet), and (iii) with quasiperiodic detuning, and demonstrated that the numerical results closely align with the analytical predictions. In Chapter [6], we discuss stochastic control of chaos in the Kicked Top model. In classical dynamical systems, a chaotic map can be stochastically controlled onto unstable periodic orbits leading to controlled and uncontrolled phases as a function of the rate at which the control is applied. In this work, we use Kicked Top a physical model of chaos, and implement a stochastic control map. The chaotic map (Kicked Top) acts with probability  $1 - p$  and the control map acts with probability  $p$ . We see that at some critical control rate  $p_c$ , the whole dynamics freezes onto the fixed point which becomes the global attractor of the combined dynamics.



# Chapter 2

## Quantum chaos, random matrix theory, and spectral statistics tools

In this chapter, we introduce and briefly discuss the subject of quantum chaos, along with the essential tools used to diagnose chaos in quantum systems. We also provide an overview of key conjectures in this field, highlighting the spectral statistics tools employed to capture the universal signatures of chaos and integrability. Additionally, we review important results from Random Matrix Theory (RMT), which are commonly used to study quantum chaos. Furthermore, we discuss the Eigenstate Thermalization Hypothesis, which explicitly connects RMT with quantum chaos, and sheds light on our current understanding of when and how isolated quantum systems thermalize, as well as when they fail to do so.

After the quantum revolution in physics, many phenomena observed and understood with the principles of classical mechanics were also explained at smaller scales, where the rules of quantum mechanics apply. Understanding the quantization of a classically chaotic system remained an exciting and challenging problem for a long time. The chaos that occurs in most systems due to non-linearity in classical dynamics remains less understood in the framework of quantum mechanics. It is due to the fact that quantum mechanics is governed by a set of linear operators and with the uncertainty principle, the phase-space picture is absent to characterize chaos in such a framework. Gutzwiller [108] initiated efforts to address this problem in the 1970s, with Wigner and Dyson's significant results [109–112] that helped establish the field of research known as quantum chaos. Wigner used RMT [14] in nuclear physics to understand the spectra

of complex nuclei and later RMT was used as a tool in modern physics in a variety of topics especially capturing the chaos signature in quantum systems and understanding the eigenstate thermalization. Below we provide an overview of RMT and its usefulness in analyzing the spectral properties of physical systems.

## 2.1 RMT and quantum chaos/integrability conjectures

Wigner's key idea was to focus on the small gaps in the spectrum where the eigenvalues exhibit a constant density of states, leading to the Hamiltonian resembling a random matrix theory. By studying the corresponding RMT within the same symmetry class, we can gain insights into the important spectral properties of the Hamiltonian. This concept has been instrumental in understanding the spectra of complex systems and the field of quantum chaos. Let's first define an ensemble of matrices drawn from a random Gaussian distribution [113],

$$P(\hat{H}) \propto \exp \left[ -\frac{\beta}{2a^2} \text{Tr}(\hat{H}^2) \right] = \exp \left[ -\frac{\beta}{2a^2} \sum_{i,j} H_{ij} H_{ji} \right]. \quad (2.1)$$

This is a general random matrix theory ensemble where  $a$  is some overall energy scale, and  $\beta$  is referred to as the Dyson index. The Dyson index  $\beta$  is used to classify ensembles of random matrices based on their symmetry and the nature of their entries. It plays a pivotal role in defining the statistical properties of the eigenvalues of random matrices and characterizes their universality classes, which are determined by the symmetries of the matrices. The value of  $\beta$  corresponds to the number of degrees of freedom associated with each independent matrix element. For  $\beta = 1$ , it is called Gaussian Orthogonal ensemble (GOE) corresponds to time-reversal symmetry where Hamiltonian is real and symmetric ( $H_{ij} = H_{ji}$ ). Without time reversal symmetry the Hamiltonian is complex hermitian ( $H_{ij} = H_{ji}^*$ ) corresponding to the Gaussian Unitary ensemble (GUE) with  $\beta = 2$ . There is also  $\beta = 4$  Wigner-Dyson class that belongs to the Gaussian Symplectic ensemble (GSE).

Level spacing distribution  $p(s)$  for  $\beta = 1, 2$  corresponds to Hamiltonian of random entries consecutively with and without time-reversal symmetry is precisely computed for

$2 \times 2$  with Gaussian distribution [14, 113, 114],

$$p_\beta(s) = A_\beta s^\beta \exp(-B_\beta s^2), \quad (2.2)$$

where  $s$  is the separation or spacing between consecutive eigenvalues.  $A_\beta$  and  $B_\beta$  can be obtained by imposing normalization conditions on distribution and fixing mean level spacing to be one. These distributions are given by,

$$p_1(s) = p_{GOE}(s) = \frac{\pi s}{2} e^{-\pi s^2/4}, \quad (2.3)$$

$$p_2(s) = p_{GUE}(s) = \frac{32s^2}{\pi^2} e^{-4s^2/\pi^2}. \quad (2.4)$$

These are called Wigner-Dyson distributions. These level spacing distributions are also derived for large dimensional RMT ensembles [defined in Eq. (2.1)] but these computations do not provide close forms but are asymptotically close to results in Eqs. (2.3, 2.4). As one can notice for  $s \rightarrow 0$ , level spacing approaches to zero with  $\sim s^\beta$  indicating the level repulsion. These are the key features of level spacing statistics that reflect the underlying symmetry of the chaotic Hamiltonian. These Hermitian random matrices from different symmetry classes exhibit distinct level statistics and define their own universality classes. In this section, we discussed the Hermitian RMT classes that are relevant for characterizing quantum chaos in Hamiltonian systems. These ideas are also applied to diagnose chaos in open quantum systems and non-Hermitian systems, where non-Hermitian RMT is utilized, which we will address in the Section [2.1.3].

### 2.1.1 BGS conjecture

In 1984, The Bohigas-Giannoni-Schmit (BGS) conjecture [115] aided in identifying chaos through the spectral statistics of Hamiltonian systems. They got the intuition from the ideas of Wigner and Dyson using RMT to study spectral statistics of complex nuclei. According to BGS conjecture, the level spacing distribution of the Hamiltonian of quantum system with chaotic classical limit follows the same statistics as the RMT ensemble corresponding to their symmetry class. A system with a Hamiltonian exhibiting time-reversal symmetry corresponds to Dyson symmetry class  $\beta = 1$  that is Gaussian orthogonal ensemble (GOE) RMT. Its spectral statistics (level spacing distribution) satisfy the Wigner-Dyson distribution that is  $p_{GOE}(s)$  defined in Eq. (2.3).

Later studies suggested that even systems with a lack of classical limit [30–39] also can be characterized as quantum chaotic systems with Wigner-Dyson level spacing statistics.

### 2.1.2 Berry-Tabor conjecture

A simple spectral measure/indicator of integrability and chaos can be found in the spectral statistics of eigenvalues of the Hamiltonian of quantum systems. Berry and Tabor studied a system of particles in one dimension whose classical dynamics is not chaotic. Based on their finding they conjectured [116] that the energy levels generic quantum integrable systems behave as uncorrelated random numbers (no level repulsion) and level spacing distribution should be described by Poisson statistics. Nearest neighbor level spacing distribution  $p(s)$  has to following 1D Poisson distribution,

$$p_{Poisson}(s) = e^{-s}, \quad (2.5)$$

where  $s$  is the spacing between consecutive energy levels.

### 2.1.3 GHS conjecture

GHS extended the BGS conjecture for the Markovian dissipative open quantum systems. They used spectra of the Liouvilian master equation and found distinct features of integrability and chaos. For this, they considered the Kicked Top model with damping (dissipation) and used a discrete quantum map [29]. In the integrable limit, they found agreement of level spacing  $p(s)$  with  $2D$  Poisson distribution that is,

$$p_{2D-P}(s) = \frac{\pi}{2} s \exp(-\pi s^2/4), \quad (2.6)$$

where  $s$  is the radial distance in the complex plane. This confirms that the spectrum is distributed as independent random numbers in the complex plane. In the chaotic limit, the level spacing distribution matches with the corresponding spacing distribution  $p_{GinUE}(s)$  of the Ginibre Unitary ensemble (GinUE) of non-Hermitian random matrices given below [29, 117],

$$p_{GinUE}(s) = \bar{s} \bar{p}_{GinUE}(\bar{s}s), \quad (2.7)$$

with

$$\bar{p}_{\text{GinUE}}(s) = \sum_{j=1}^{\infty} \frac{2s^{2j+1} \exp(-s^2)}{\Gamma(1+j, s^2)} \prod_{k=1}^{\infty} \frac{\Gamma(1+k, s^2)}{k!}, \quad (2.8)$$

and  $\bar{s} = \int_0^{\infty} ds s \bar{p}_{\text{GinUE}}(s)$ . Here,  $\Gamma(1+k, s^2) = \int_{s^2}^{\infty} t^k e^{-t} dt$  is the incomplete Gamma function.

The non-Hermitian random matrix ensembles introduced by Ginibre [118]—GinUE, GinOE, and GinSE are non-Hermitian extensions of the GUE, GOE, and GSE from the Hermitian case. Unlike the universality classes of Hermitian RMT, which exhibit distinct level spacing statistics, all three Ginibre matrices share the same level spacing statistics. Subsequently, this conjecture was extended to systems without a classical limit and to non-Hermitian systems, utilizing the spectral statistics of non-Hermitian RMT ensembles as an indicator of chaos [117, 119, 120].

## 2.2 Adjacent gap ratio

Adjacent gap ratio proposed by Oganessian and Huse  $\langle r \rangle$  [70], defined in terms of successive gaps  $\delta_i = E_{i+1} - E_i$  of the real spectra is given by

$$r_i = \frac{\min(\delta_i, \delta_{i+1})}{\max(\delta_i, \delta_{i+1})}. \quad (2.9)$$

First, it was introduced to characterize the change of statistics across a MBL transition. It has become one of the most extensively studied metrics in the field of disordered quantum systems for identifying signatures of integrability and chaos. This measure has a notable advantage over level spacing distribution because it suppresses local variations in the density of states, eliminating the need for the numerical unfolding of spacing to compute this quantity. It captures information about next-nearest neighbors which is missed in the conventional diagnostics of level-spacing statistics. The probability distribution  $P(r)$  of gap ratios is well-suited to characterize statistical properties of many-body spectra and analytical expressions are known for integrable case and RMT.

Analytical expressions for the adjacent gap ratio distribution [121–123] for integrable

(independent Poisson numbers) and chaotic (RMT) spectra are given by

$$P_{\text{Poisson/RMT}}(r) = 2 \tilde{P}_{\text{Poisson/RMT}}(r) \Theta(1-r), \quad (2.10)$$

with

$$\begin{aligned} \tilde{P}_{\text{Poisson}}(r) &= \frac{1}{(1+r)^2}, \\ \tilde{P}_{\text{RMT}}(r) &= \frac{1}{Z_\beta} \frac{(r+r^2)^\beta}{(1+r+r^2)^{1+\frac{3}{2}\beta}}, \end{aligned} \quad (2.11)$$

where  $Z_\beta$  is the normalization constant which depends on the Dyson index of the random matrix ensemble,  $\beta$ . For the Gaussian Orthogonal Ensemble (GOE),  $\beta = 1$  and  $Z_\beta = 8/27$ .

The average adjacent gap ratio, defined as  $\langle r \rangle = \int_0^1 dr r P(r)$ , is commonly used as a quantitative measure of quantum chaos and integrability. It is especially useful for tracking the transition from chaos to integrability as a function of a Hamiltonian parameter. The exact value of  $\langle r \rangle$  can be computed using Eq. (2.11) for independent Poisson levels and GOE RMT:

$$\begin{aligned} \langle r \rangle_{\text{Poisson}} &= 2 \ln 2 - 1 \approx 0.386, \\ \langle r \rangle_{\text{GOE}} &= 4 - 2\sqrt{3} \approx 0.536. \end{aligned} \quad (2.12)$$

The averages have been used to estimate a critical value of the transition parameter signifying the extent of symmetry crossover. This kind of statistics is particularly useful in real complex systems where one is unaware of the full analytical solution of crossover from one symmetry class to another. If the system is in the MBL phase, irrespective of symmetries present,  $\langle r \rangle \approx \langle r \rangle_{\text{Poisson}}$ . For ergodic systems, the value of  $\langle r \rangle$  depends on the global symmetries present in the system.

Generalization of this quantity for complex spectra was also introduced in Ref. [124] and is given by

$$z_i = r_i e^{i\theta_i} = \frac{E_i^{\text{NN}} - E_i}{E_i^{\text{NNN}} - E_i}, \quad (2.13)$$

where the superscripts NN (NNN) stand for nearest (next-nearest) neighbor. The distribution of  $z_i$  in the complex plane itself provides a qualitative distinction between the spectra of chaotic and integrable systems. For integrable systems, the distribution of  $z$

forms a uniform disk on the complex plane. In the case of chaos, however, the distribution becomes anisotropic in the angular direction and moves away from the origin, indicating level repulsion in the spectrum. Anisotropy and radial repulsion are measured by computing  $\langle \cos(\theta) \rangle$  and  $\langle r \rangle$  which are angular and radial parts of the complex quantity  $z$ . Using these measures we can make a distinction between integrable and chaotic systems.

## 2.3 Spectral form factor

The spectral form factor (SFF) is an important non-local spectral probe, which we denote as  $K(\tau, N)$ . SFF and its connected version (CSFF)  $K_c(\tau, N)$  captures 2-point spectral density density correlations. Lets first consider the density of state  $\rho(\lambda, N)$  of any spectra  $\{E_i\}$ ,

$$\rho(\lambda, N) = \sum_i^N \delta(E_i - \lambda). \quad (2.14)$$

We define  $Z(\tau, N)$  that is the Fourier transformation of the density of state and can be simplified using the above density of state expression,

$$Z(\tau, N) = \int_{-\infty}^{\infty} d\lambda \rho(\lambda, N) e^{-i\lambda\tau} = \sum_i e^{-iE_i\tau} = \text{tr} e^{-iH\tau}. \quad (2.15)$$

SFF and CSFF for of ensembles of  $N$  eigenvalues  $\{E_i\}$  can be defined in terms of  $Z(\tau, N)$  as following [71],

$$K(\tau, N) = \left\langle |Z(\tau, N)|^2 \right\rangle = \left\langle \sum_{m,n=1}^N e^{i\tau(E_m - E_n)} \right\rangle, \quad (2.16)$$

$$K_c(\tau, N) = K(\tau, N) - \left| \left\langle Z(\tau, N) \right\rangle \right|^2 = \left\langle \sum_{m,n=1}^N e^{i\tau(E_m - E_n)} \right\rangle - \left| \left\langle \sum_{m=1}^N e^{i\tau E_m} \right\rangle \right|^2, \quad (2.17)$$

where  $\langle \dots \rangle$  stands for average over ensembles.

The SFF for random matrix spectra, applicable to quantum chaotic systems, has been the subject of intense study and has recently attracted renewed interest [71–77, 83]. Systems with time-reversal symmetry, the appropriate RMT ensemble is the Gaussian Orthogonal Ensemble (GOE) for which the approximate expression of SFF is known [71–

74]. The early-time behavior of SFF, its dip, and subsequent oscillations, are dominated by non-universal features of the spectrum. In the intermediate to long-time regime, the linear ramp between Thouless and Heisenberg times and the subsequent plateau are well-known universal signatures of quantum chaos.

Thouless and Heisenberg times are important time scales related to the dynamics of the quantum system. These time scales are particularly relevant in understanding the dynamics of complex quantum systems, such as disordered systems, systems exhibiting quantum chaos, and quantum systems out of equilibrium. The Heisenberg time [19]  $\tau_H$  scale is associated with the uncertainty in the energy levels and it can be estimated as inverse of mean of spacing between energy levels. In disordered systems, such as those exhibiting quantum chaos, the Heisenberg time indicates how quickly the system evolves in terms of its energy eigenstates. The Thouless time [125–128]  $\tau_T$  is related to the diffusive behavior of a system, and it is crucial for understanding localization and the transition between localized and delocalized phases in disordered systems. For chaotic systems  $\tau_T \ll \tau_H$ , system explore all its eigenstates. During the time interval between  $\tau_T$  and  $\tau_H$ , system evolve and form universal ramp features in the spectral form factor.

To reduce clutter, we will focus on the SFF [Eq. (2.16)] but comment on the CSFF [Eq. (2.17)] when necessary. For a fixed number  $N$  (which we assume to be large throughout this thesis), as  $\tau$  is tuned, the SFF probes the correlations in the spectrum on scales inversely proportional to  $\tau$ . It is useful to separate the behavior of the SFF on various  $\tau$  scales. In general, there are three  $\tau$  regions separated by the so-called Thouless time  $\tau_T \sim \frac{1}{\mu N}$  and Heisenberg time  $\tau_H \sim \frac{1}{\mu}$  where  $\mu$  is the mean level spacing [71, 83]:

1. *Early*  $\tau$ : For small values of  $\tau \ll \tau_T$ , the SFF probes the spectrum on the bandwidth scale and is sensitive to the tails of the spectrum.
2. *Intermediate*  $\tau$ : For  $\tau_T < \tau < \tau_H$ , the behavior is expected to be dominated by universal correlations, if present. This is usually the regime of prime interest.
3. *Late*  $\tau$ : For large values of  $\tau \gg \tau_H$ , the SFF probes the spectrum on the scale of the mean level spacing where the levels are quantized. In the absence of accidental degeneracies, the expression of SFF Eq. (2.16) in this regime is thus dominated by terms where  $E_m = E_n$  and the SFF plateaus at  $K \approx N$ .

It is interesting to note that SFF also has a broader appeal. In addition to encoding

information about long-range correlations, SFF is also a highly valuable computational quantity. Some of the reasons are, (i) SFF is closely connected to a dynamical quantity called the survival probability [129, 130]. (ii) SFF is amenable to analytical calculations for certain systems where other quantities are far from being analytically tractable. For e.g. there has recently been work on hydrodynamic theory of the connected spectral form factor [131]. (iii) There are deep analytical insights for SFF results for eigenvalues of random matrix theories [71–77]. This makes it possible to explore deep connections between chaotic quantum Hamiltonians and random matrix theory through the lens of SFF.

### 2.3.1 The spectral form factor for random matrices

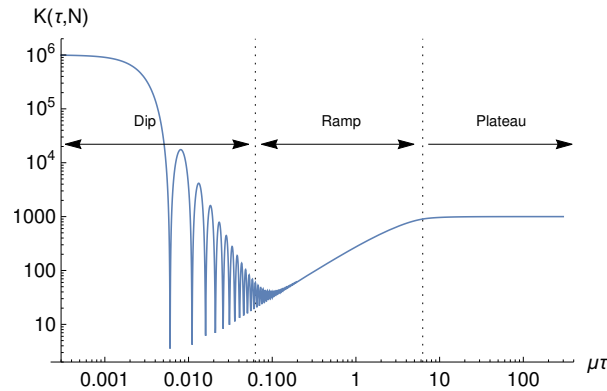


Figure 2.1: SFF for GOE ensemble shown in Eq. (2.18) with  $N=1000$ . The separation between dip, ramp, and plateau regimes is schematically indicated using dotted lines.

The SFF for random matrix spectra, applicable to quantum chaotic systems, has been the subject of intense study and has recently attracted renewed interest [71–77, 83]. We briefly review the results here. The precise nature of the random matrix SFF depends on the underlying symmetries [14, 71]. For systems with time-reversal symmetry, the appropriate RMT ensemble is the Gaussian Orthogonal Ensemble (GOE) for which the

approximate expression of SFF can be written as [71–74]

$$K^{GOE}(\tau, N) = K_c^{GOE}(\tau, N) + \left[ \frac{\pi}{\mu\tau} J_1 \left( \frac{2N\mu\tau}{\pi} \right) \right]^2, \quad (2.18)$$

$$K_c^{GOE}(\tau, N) = N \begin{cases} \frac{\mu\tau}{\pi} - \frac{\mu\tau}{2\pi} \log \left( 1 + \frac{\mu\tau}{\pi} \right) & 0 < \mu\tau < 2\pi \\ 2 - \frac{\mu\tau}{2\pi} \log \left( \frac{\mu\tau + \pi}{\mu\tau - \pi} \right) & 2\pi < \mu\tau < \infty \end{cases},$$

where  $J_1(x)$  is the Bessel function of the first kind. A plot of Eq. (2.18) is shown in Fig. 2.1 where we can see three qualitative regimes - an early dip ( $\tau < \tau_T$ ), intermediate ramp ( $\tau_T < \tau < \tau_H$ ) and a late saturation ( $\tau > \tau_H$ ). The SFF for other RMT ensembles also exhibits these three regimes, which are considered to be universal features of level repulsions and many-body quantum chaos.

### 2.3.2 The spectral form factor for Poisson numbers

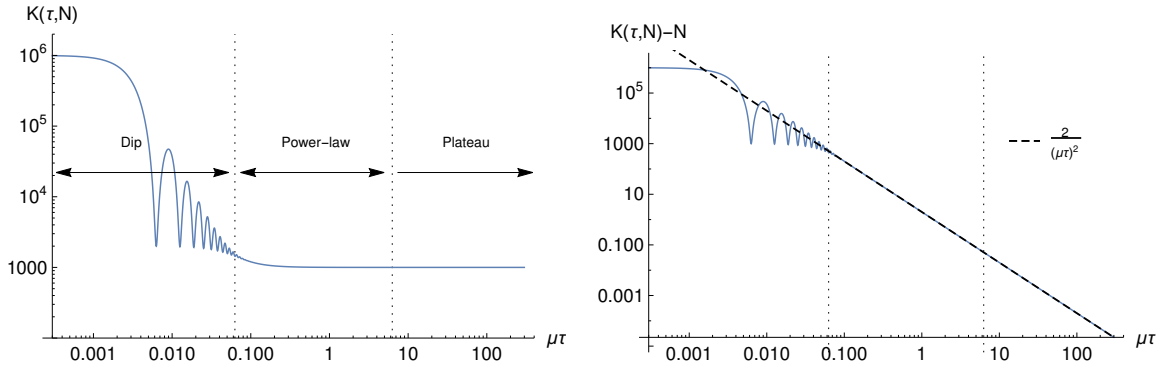


Figure 2.2: Left: SFF for Poisson levels shown in Eq. (2.23). Right: The power-law scaling form for  $\tau_T < \tau < \tau_H$  is exposed by subtracting the saturation value of  $N$  (chosen to be 1000 for both plots).

The SFF for Poisson numbers applicable to MBL and integrable systems was investigated in detail only recently [83–85]. An uncorrelated spectrum that resembles that of integrable and MBL systems can be generated [83] by starting with nearest-neighbour gaps  $\{\delta_n\}$  from an exponential distribution,

$$P(\delta_n) = \frac{1}{\mu} e^{-\delta_n/\mu}, \quad (2.19)$$

and summing them up

$$E_n = \sum_{r=1}^n \delta_r. \quad (2.20)$$

The joint 2-point probability distribution for this spectrum,  $P(E_n, n; E_m, m)$  i.e. the probability that the  $m^{\text{th}}$  eigenvalue is  $E_m$  and the  $n^{\text{th}}$  eigenvalue is  $E_n$  is

$$P(E_n, n; E_m, m) = p(E_n, n) p(E_m - E_n, m - n), \quad (2.21)$$

where  $p(E_k, k)$  ( $k = 1, 2, 3, \dots$ ) is the well-known Poisson distribution

$$p(E_k, k) = \begin{cases} \frac{e^{-\frac{E_k}{\mu}}}{\mu^{(k-1)!}} \left(\frac{E_k}{\mu}\right)^{k-1} & E_k \geq 0 \\ 0 & E_k < 0 \end{cases}. \quad (2.22)$$

Using this, the SFF can be calculated to obtain the following expression (see Ref. [84] and the supplementary materials of Ref. [83] for the derivation)

$$K^P(\tau, N) = N + \frac{2}{(\mu\tau)^2} - \frac{(1 + i\mu\tau)^{1-N} + (1 - i\mu\tau)^{1-N}}{(\mu\tau)^2}. \quad (2.23)$$

In Fig. 2.2, we see that the SFF for the spectrum in Eq. (2.20) can also be divided into three  $\tau$  regimes. Now we focus on the intermediate  $\tau$  regime  $\frac{1}{N} < \mu\tau < 1$  when the SFF form reduces to [83]

$$K^P(\tau, N) = N + \frac{2}{(\mu\tau)^2} + \dots \quad (2.24)$$

We can see that if we subtract the asymptotic value of  $N$ ,  $K(\tau, N) - N$  (which we will refer to as the reduced SFF) assumes a power law form independent of  $N$  with a fixed exponent and can be used to characterize systems with uncorrelated spectra as shown in Ref. [83]. Although the spectrum in Eq. (2.20) was built in a specific way, it captures many essential features of uncorrelated levels. For example, if  $N_R$  numbers were drawn from any distribution and  $N$  of those were selected from a fixed window after ordering, the distribution of  $k^{\text{th}}$  neighbor spectral gaps  $E_n - E_{n+k}$  of these  $N$  numbers approaches the Poisson distribution Eq. (2.22) (see the supplementary materials of Ref. [83]). Similarly, the same is expected to be true for  $N$  energy levels chosen from the middle of the spectrum of a system deep in the MBL phase. However, one feature

of the spectrum in Eq. (2.20) is the fact that all levels  $E_n$  are positive definite, which results in a sharp step-like feature in the density of states (DOS) which is absent if we choose  $N$  levels from the middle of a quantum many-body spectrum. As we will see in the coming sections, signatures such as the one shown in Eq. (2.24) are unaffected by this DOS feature and describe the spectra of MBL systems fairly accurately. Throughout the thesis (in Chapter [4] and Chapter [5]), we will focus only on the SFF as defined in Eq. (2.16). Some subtleties regarding connected SFF, especially regarding the effects of sharp DOS Eq. (2.17) will be discussed in Appendix [C].

## 2.4 Density of all gaps

We now discuss another useful quantity — the density of all gaps (DOG),  $\chi(x, N)$ , defined as

$$\chi(x, N) = \frac{1}{N(N-1)} \left\langle \sum_{m \neq n=1}^N \delta(x - (E_m - E_n)) \right\rangle, \quad (2.25)$$

and is related to the SFF in Eq. (2.16) as follows

$$K(\tau, N) = N + N(N-1) \int_{-\infty}^{\infty} dx e^{i\tau x} \chi(x, N). \quad (2.26)$$

In other words, the SFF is related to the Fourier transform of the DOG. We note that often the SFF is written in terms of the two-point density correlator [14]

$$K(\tau, N) = N + N(N-1) \quad (2.27)$$

$$\int_{-\infty}^{\infty} dx \int_{-\infty}^{\infty} dy e^{i\tau(x-y)} \rho^{(2)}(x, y, N). \quad (2.28)$$

$$\rho^{(2)}(x, y, N) = \frac{1}{N(N-1)} \left\langle \sum_{m \neq n=1}^N \delta(x - E_m) \delta(y - E_n) \right\rangle. \quad (2.29)$$

We can relate  $\chi(x, N)$  in Eq. (2.25) to  $\rho^{(2)}(x, y, N)$  as follows

$$\chi(x, N) = \int_{-\infty}^{\infty} du \rho^{(2)}(x+u, u, N). \quad (2.30)$$

We will see that studying the DOG exposes interesting details about spectral correlations.

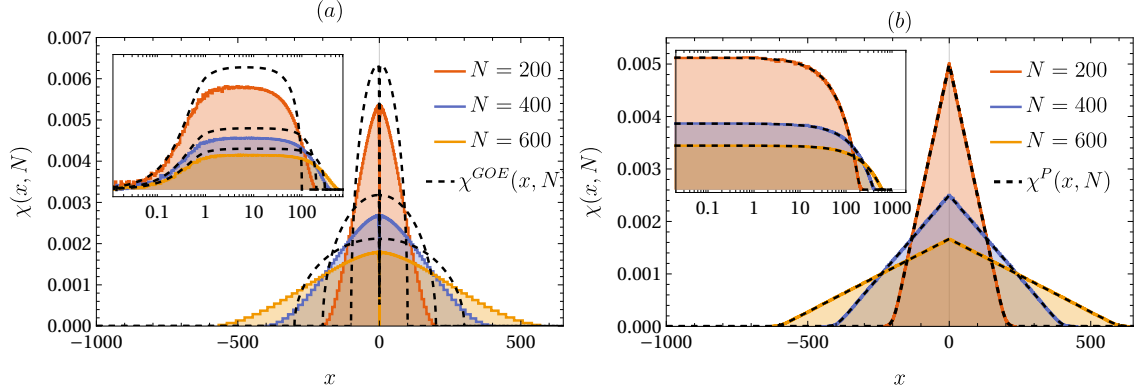


Figure 2.3: (a) DOG [Eq. (2.25)] for the eigenvalues of GOE matrices compared with analytical expression in Eq. (2.31). (b) DOG [Eq. (2.25)] of Poisson levels compared with analytical expression in Eq. (2.34). The insets show the same figure restricted to positive values with the x-axis in log scale to clarify the behavior near the origin. The plot for each  $N$  is generated using 5000 levels with mean level spacing  $\mu = 1$ .

### 2.4.1 Density of all gaps for random matrices

We can obtain approximate analytical forms for the DOG for both the RMT and Poisson cases. Let us start with the former. The expression for GOE matrices is [14, 72, 74, 75]

$$\chi^{GOE}(x, N) = \rho(x, N)(1 - Y_2(x)), \quad (2.31)$$

where  $\rho(\lambda, N)$  is the well-known semi-circle density of states

$$\rho(\lambda, N) = \begin{cases} \frac{4}{\pi N \mu} \sqrt{1 - \left(\frac{2\lambda}{\mu N}\right)^2} & |\lambda| < \frac{N\mu}{2} \\ 0 & |\lambda| > \frac{N\mu}{2} \end{cases}. \quad (2.32)$$

and  $Y_2(x)$  is the asymptotic connected two-point spectral correlator [14]

$$Y_2(\mu r) = \left(\frac{\sin(\pi r)}{\pi r}\right)^2 + \left[ \int_r^\infty ds \left(\frac{\sin(\pi s)}{\pi s}\right) \right] \left[ \frac{\partial}{\partial r} \left(\frac{\sin(\pi r)}{\pi r}\right) \right]. \quad (2.33)$$

Following [72, 74, 75], we improve  $Y_2(x)$  by introducing a density correction to the argument. Fig. 2.3 (a) shows a comparison between the numerically computed DOG and the expression in Eq. (2.31). The agreement is very good for small gaps  $x$  that correspond to  $\tau > \tau_T$  in the SFF but deviates for large gaps  $x$  that correspond to  $\tau < \tau_T$  in the

SFF.

## 2.4.2 Density of all gaps for Poisson numbers

For Poisson spectra generated as described in Eq. (2.23), we can compute  $\chi(x, N)$  exactly using the distribution in Eq. (2.22) in the formula Eq. (2.25) to get

$$\chi^P(x, N) = \frac{\left( e^{-\frac{|x|}{\mu}} \left( \frac{|x|}{\mu} \right)^N - \left( \frac{|x|}{\mu} - (N-1) \right) \Gamma \left( N, \frac{|x|}{\mu} \right) \right)}{\mu(N-1)N!}, \quad (2.34)$$

where  $\Gamma(x, N)$  is the incomplete Gamma function defined as follows (for integer  $N$ )

$$\Gamma(N, x) = \int_x^\infty dt t^{N-1} e^{-t} = e^{-x} (N-1)! \sum_{k=0}^N \frac{x^k}{k!}. \quad (2.35)$$

As seen in Fig. 2.3 (b), the exact expression perfectly matches the numerical data.

Much like the adjacent gap ratio, the DOG is a useful diagnostic not only for characterizing the MBL and ergodic phases but also for estimating the location of the transition between them. For example, from the expressions Eqs. (2.31, 2.34), we see that for RMT levels,  $\chi(0, N) \rightarrow 0$  while for Poisson numbers  $\chi(0, N) \rightarrow \frac{1}{N}$ . Thus, the quantity  $N\chi(0, N)$  takes values between 0 and 1 and tracking it on finite-size systems should give us an estimate of the transition between the MBL and ergodic phases where different system sizes cross. We will see in the next section that this is indeed true for various physical models hosting an MBL to ergodic transition.

## 2.5 Eigenstate Thermalization Hypothesis

Above we discussed quantum chaos and the relevance of RMT to characterize it in quantum systems using various spectral statistics tools. Here we will briefly review thermalization and the emergence of statistical mechanics behavior in isolated quantum systems whose governing dynamics is unitary. The study of thermalization is mainly focused on monitoring the behavior of observables for a long time. An observable is considered to be thermalized when it evolves under the unitary dynamics of the system and relaxes over a long time to a state where it can be replaced with the prediction of

the microcanonical ensemble. The time evolution of expectation value of observable  $\hat{O}$ ,

$$\begin{aligned}
O(t) &= \langle \psi(t) | \hat{O} | \psi(t) \rangle \\
&= \sum_{m,n} C_m^* C_n e^{i(E_m - E_n)t} O_{mn} \\
&= \sum_m |C_m|^2 O_{mm} + \sum_{m,n \neq m} C_m^* C_n e^{i(E_m - E_n)t} O_{mn}.
\end{aligned} \tag{2.36}$$

Here  $O_{mn} = \langle m | \hat{O} | n \rangle$  where,  $|m\rangle$  is the eigenstate of Hamiltonian. If the expectation value of the observable approaches the average value calculated using the microcanonical ensemble, it suggests that the primary contribution comes from the diagonal matrix elements. In this case, the observable undergoes thermalization. When the Hamiltonian matrix is a random matrix structure then using RMT prediction it can be concluded that diagonal elements of observable  $O_{mm}$  are independent of eigenstates labels  $m$  and off-diagonal elements are exponentially small in systems size that satisfies the thermalization condition. The statistical mechanics of isolated quantum systems using RMT was first explored by Deutsch [132]. Our current understanding of thermalization in isolated quantum systems is based on the Eigenstate Thermalization Hypothesis (ETH) [22] that was proposed by Srednicki. According to ETH an ansatz for matrix element of the few body observable on the energy eigenbasis of Hamiltonian is,

$$O_{mn} = O(\bar{E})\delta_{mn} + e^{-S(\bar{E})/2} f_O(\bar{E}, \omega) R_{mn}, \tag{2.37}$$

where  $\bar{E} = (E_m + E_n)/2$  is the average energy of considered pair of eigenstates,  $\omega = E_m - E_n$  is the corresponding energy difference, and  $S(\bar{E})$  is the thermodynamic entropy at energy  $\bar{E}$ .  $O(\bar{E})$  and  $f_O(\bar{E}, \omega)$  are smooth functions of their arguments. And,  $R_{mn}$  are random numbers with zero mean and unit variance. Our current understanding is that systems whose observables satisfy the ETH are generally quantum chaotic/ergodic, and they thermalize over a timescale. Systems that do not satisfy the ETH are integrable [58–60], exhibit many-body localization (MBL) [53–57], and quantum many-body scars [61, 62], and as a result they fail to thermalize.



# Chapter 3

## Dissipative quantum dynamics, phase transitions, and non-Hermitian random matrices

In this work, we study the spectral properties of the Liouvillian of a dissipative version of the paradigmatic Dicke model [133, 134]. In the thermodynamic limit, the isolated Dicke model displays a  $\mathbb{Z}_2$  symmetry-breaking quantum phase transition between a normal and a superradiant phase [135–137]. Studies of the spectral statistics of the Dicke Hamiltonian [138, 139] revealed that the level spacings are Poisson distributed in the normal phase, reflective of integrable dynamics, whereas they are distributed according to the Gaussian Orthogonal Ensemble in the superradiant phase, indicating chaotic dynamics. Here, via exact diagonalization of the Liouvillian, we discuss whether and how these connections with RMT can be generalized to the context of phase transitions in open quantum systems. More precisely, we address the robustness of the signatures of integrability as the system is driven through a phase transition by turning on an integrability-breaking perturbation.

### 3.1 Dissipative Dicke model

The dissipative Dicke model describes the coupling of an ensemble of closely packed quantum emitters to a single leaky cavity mode [133, 134]. In the Markovian approximation, the evolution of the density matrix  $\rho$  is governed by a Lindblad Master equation

where the Liouvillian superoperator reads

$$\mathcal{L} \star = -i [H, \star] + \kappa [2a \star a^\dagger - \{a^\dagger a, \star\}], \quad (3.1)$$

with  $\kappa > 0$  being the cavity decay rate and  $\star$  stands for operators on the Hilbert space. The Dicke Hamiltonian is given by

$$H = \omega_c a^\dagger a + \omega_s S^z + \frac{2\lambda}{\sqrt{S}} (a^\dagger + a) S^x. \quad (3.2)$$

$a$  ( $a^\dagger$ ) is the bosonic annihilation (creation) operator of a cavity mode with energy  $\omega_c$ .  $S^\alpha$ ,  $\alpha = x, y, z$ , are the spin angular momentum operators built from the totally symmetric representation of  $S$  identical two-level systems with energy splitting  $\omega_s$ .  $\lambda$  is the cavity-spin coupling which is rescaled by  $1/\sqrt{S}$  to ensure a non-trivial thermodynamic limit ( $S \rightarrow \infty$ ). The Dicke Hamiltonian is  $\mathbb{Z}_2$ -symmetric:  $[H, \Pi] = 0$  where the operator

$$\Pi = \exp [i\pi(a^\dagger a + S^z + S/2)] \quad (3.3)$$

gives the parity of the total number of excitations. As a consequence of the specific structure of the dissipator in Eq. (3.1), the Liouvillian inherits a so-called weak  $\mathbb{Z}_2$  symmetry:

$$[\mathcal{L}, \Pi] = 0, \quad \Pi \star = \Pi \star \Pi^\dagger \quad (3.4)$$

gives the parity of the difference of the number of excitations between the left and right sides of the states in Liouville space [140–143] defined in Eq. (3.5). In the thermodynamic limit, this weak  $\mathbb{Z}_2$  symmetry is spontaneously broken in the steady state at  $\lambda = \lambda^* = \frac{1}{2}\sqrt{\omega_c \omega_s} \sqrt{1 + \kappa^2/\omega_c^2}$ , corresponding to a second-order dissipative phase transition [137, 144, 145]. In the normal phase, *i.e.*  $\lambda < \lambda^*$ , the boson expectation value vanishes:  $\langle a \rangle = 0$ . In the superradiant phase, *i.e.*  $\lambda > \lambda^*$ , it acquires a finite expectation value:  $\langle a \rangle \neq 0$ . At  $\lambda = 0$ , the model is trivially integrable. The counter-rotating terms,  $a^\dagger S^+$  and  $a S^-$ , break the quantum integrability of the model.

### 3.1.1 Computing the spectrum of the dissipative Dicke Liouvillian

We use a convenient basis of the Liouville space spanned by the states

$$|\alpha\rangle\rangle \equiv |n_l, m_l\rangle\langle n_r, m_r|, \quad (3.5)$$

where  $|n, m\rangle$  are the Fock states of the Dicke Hamiltonian with  $n$  cavity excitations and  $m = -S/2, -S/2+1, \dots, S/2$  is the quantum number associated with the  $z$ -component of the spin.  $\alpha$  collects all the quantum numbers  $n_l, m_l, n_r, m_r$ . The notation  $|\alpha\rangle\rangle$  underlines that operators on the Hilbert space are states in the Liouville space. In practice, we truncate the Hilbert and Liouville spaces by introducing a cavity cutoff:  $n = 0, 1, \dots, n_{\text{cutoff}}$ . In the above basis, the Liouvillian can be represented by a matrix  $L$  with the elements  $L_{\alpha\alpha'} = \langle\langle\alpha|\mathcal{L}|\alpha'\rangle\rangle$ , where the Hilbert-Schmidt inner product [17, 146] is given by

$$\langle\langle\alpha|\alpha'\rangle\rangle \equiv \text{Tr}\left[ (|n_l, m_l\rangle\langle n_r, m_r|)^\dagger |n'_l, m'_l\rangle\langle n'_r, m'_r| \right] \quad (3.6)$$

and the trace is performed over the Hilbert space. Let us recall that  $\mathcal{L}$  has a parity symmetry [140–142],  $[\mathcal{L}, \Pi] = 0$ , where the superoperator  $\Pi$  acts on the basis states as

$$\Pi|\alpha\rangle\rangle = \Pi|n_l, m_l\rangle\langle n_r, m_r| = \zeta|\alpha\rangle\rangle, \quad (3.7)$$

with  $\zeta = +1$  if  $(n_l + m_l) - (n_r + m_r)$  is even and  $\zeta = -1$  if it is odd. This weak  $\mathbb{Z}_2$  symmetry of  $\mathcal{L}$  guarantees that it does not couple states of the Liouville space with different parities. Hence,  $L$  can be organized as a two-by-two block-diagonal matrix. To avoid spurious overlaps of eigenvalues, we discard the odd-parity block. Finally, the even-parity block matrix is fed to a diagonalization algorithm of the LAPACK library suited to complex non-Hermitian matrices.

## 3.2 Spectral statistics of complex spectra of Liouvillian

We analyze the statistical properties of the complex eigenvalues  $\{E_i\}$  of the Liouvillian operator  $\mathcal{L}$  by means of extensive numerical computations. We work in the even parity

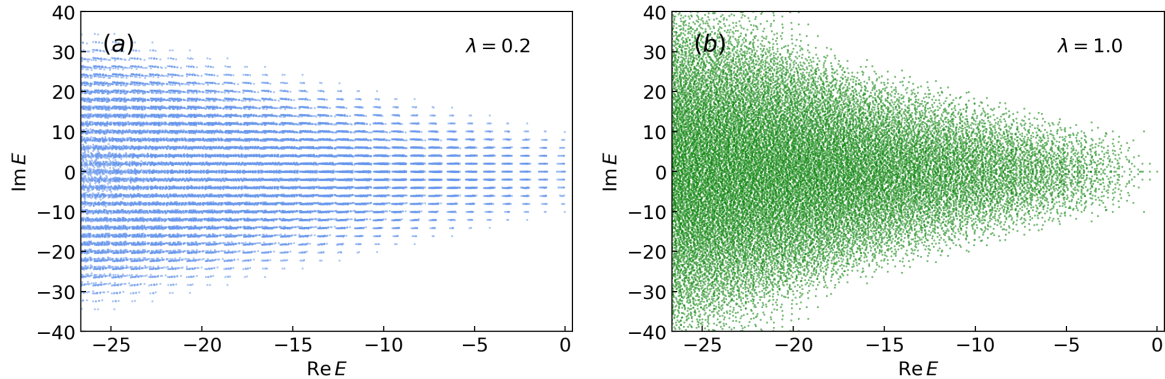


Figure 3.1: Scatter plot of the complex spectrum of the Liouvillian  $\mathcal{L}$  of the dissipative Dicke model for  $S = 10$  and  $\omega_c = \omega_s = \kappa = 1$  for which  $\lambda^* = 1/\sqrt{2}$ . (a) Normal phase,  $\lambda = 0.2$ . (b) Superradiant phase,  $\lambda = 1.0$ . A stark difference in the structure of the spectrum above and below the critical point can be observed.

sector of the Liouville space to avoid possible spurious overlaps of eigenvalues from the different symmetry sectors [147]. Throughout the chapter, we consider the strongly dissipative regime,  $\omega_c = \omega_s = \kappa = 1$ , for which the critical point is located at  $\lambda^* = 1/\sqrt{2} \approx 0.71$ .

In practice, the numerical approach comes with two inherent limitations: (i) The infinitely large bosonic Hilbert space of the cavity has to be truncated to a finite number of excitations,  $n_{\text{cutoff}} = 40$ . (ii) Numerical errors during the diagonalization process can propagate dangerously, yielding an accuracy of the results far worse than machine precision. Consequently, we truncate our spectra to an energy window  $\text{Re } E_i \in [-\alpha\kappa n_{\text{cutoff}}, 0]$  where we make sure that statistics are converged with respect to  $n_{\text{cutoff}}$ . Although its precise value is of little consequence to our findings, we choose  $\alpha = 2/3$ . This amounts to analyzing the statistical properties of those eigenvalues which correspond to intermediate to long-lived dynamics. We work with 128 bits complex double float precision.

The overall aspect of the spectrum is illustrated in Fig. 3.1 for different values of the cavity-spin coupling  $\lambda$  and for fixed spin size  $S = 10$ . The symmetry about the real axis is a generic feature of Liouvillians of Lindblad Master equations [17]. The unique steady-state of the dynamics corresponds to the single eigenvalue located at  $E = 0$ . The spectra in the two phases display clear differences. In the non-interacting limit,  $\lambda = 0$ , the spectrum displays ladder structures across both the imaginary and the real axis. The former are a direct consequence of our choice of resonant parameters,

$\omega_c = \omega_s$ , whereas the latter stem from the fragmentation of the Liouville space due to the presence of continuous symmetries at  $\lambda = 0$ : The weak  $U(1)$  symmetry corresponding to the conservation of superoperators  $[a^\dagger a, \star]$  and the strong  $U(1)$  symmetry corresponding to the conservation of  $S^z$ . In the normal phase,  $0 < \lambda < \lambda^*$ , the spectrum in Fig. 3.1 still displays structured patterns that are inherited from the non-interacting limit. The effect of a small but finite interaction can be seen as a renormalization of  $\omega_c$ ,  $\omega_s$  and  $\kappa$  leading to smearing of the patterned spectrum. There, the existence of patterns across the real axis is robust and we suspect them to be rooted in the fragmentation of Liouville space due to the emergence of approximately conserved quantities. This fragmentation disappears as  $\lambda$  approaches  $\lambda^*$  and the spectrum does not display such signature of emergent conservation laws in the superradiant phase,  $\lambda > \lambda^*$ .

### 3.2.1 Spacing statistics of complex eigenvalues

In order to unveil the universal features of these complex spectra, we turn to the study of level-spacing statistics. We first perform an unfolding of the spectrum using standard procedures which is discussed in detail below. The unfolded spectrum is then used to generate the histogram of the Euclidean distance  $s$  between nearest-neighbor eigenvalues in the complex plane, yielding the complex-level spacing distribution  $p(s)$ .

To eliminate the system-specific features of the level-spacing statistics, we first perform an unfolding procedure of the spectrum. Several methods have been proposed for the case of a complex spectrum [148, 149]. We use the method of Ref. [117]. First, we compute the Euclidean distance of each of the  $N$  complex eigenvalues to its nearest neighbor (NN)  $s_i \equiv |E_i - E_i^{\text{NN}}|$ . Next, we rescale these distances as

$$s_i \rightarrow s'_i = s_i \frac{\sqrt{\rho_{\text{av}}(E_i)}}{\bar{s}}, \quad (3.8)$$

where  $\rho_{\text{av}}(E_i)$  is the local average density approximated by

$$\rho_{\text{av}}(E) = \frac{1}{2\pi\sigma^2 N} \sum_{i=1}^N \exp\left(-\frac{|E - E_i|^2}{2\sigma^2}\right) \quad (3.9)$$

and  $\sigma$  is chosen greater than the global mean level spacing given by  $\tilde{s} = (1/N) \sum_{i=1}^N s_i$ . This guarantees a smooth distribution function on the scale of  $\tilde{s}$ . In practice, we work with  $\sigma = 4.5 \times \tilde{s}$ .  $\bar{s}$  in Eq. (3.8) is set to ensure that the global mean level spacing of

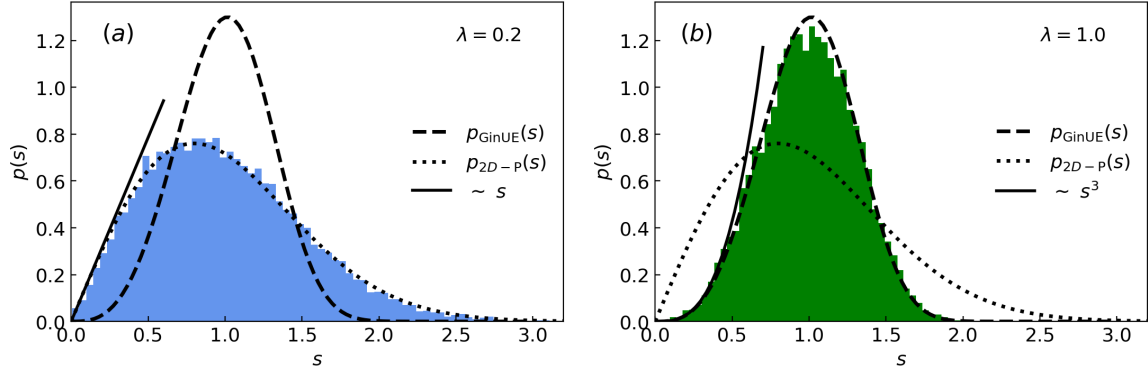


Figure 3.2: Level-spacing distribution of the complex spectrum of the Liouvillian  $\mathcal{L}$  in (a) normal phase with  $\lambda = 0.2$ , and (b) superradiant phase with  $\lambda = 1.0$ . We find remarkable agreement with the  $2D$  Poisson distribution  $p_{2D-P}(s)$  given in Eq. (2.6) and that of the GinUE RMT prediction  $p_{\text{GinUE}}(s)$  given in Eq. (2.7) in the normal phase and in the superradiant phase, respectively.

the  $s'_i$  is unity:  $(1/N) \sum_{i=1}^N s'_i = 1$ . Finally, the statistics of nearest-level spacings are computed from the  $s'_i$ . In the main text, we drop the prime notation in  $s'_i$  for the sake of simplicity.

Using the GHS conjecture, which is introduced in Section [2.1.3], we analyze integrability and chaos in the dissipative Dicke model. The results are summarized in Fig. 3.2 for values of  $\lambda$  corresponding to the normal and superradiant phases. For comparison, we also plot the corresponding spacing distribution for independent complex random numbers, namely the  $2D$  Poisson distribution defined in Eq. (2.6) as well as the distribution for the eigenvalues of the corresponding non-Hermitian random matrix ensemble [29,117]. Given the absence of symmetry of our Liouvillian (the so-called  $A$  class), it corresponds to the Ginibre Unitary Ensemble (GinUE) [149–152]<sup>1</sup> is defined in Eq. (2.7).

Fig. 3.2 demonstrates that the distributions computed from the spectrum of  $\mathcal{L}$  in Eq. (3.1) are in remarkable agreement with  $2D$  Poisson in the normal phase, and with the GinUE prediction in the superradiant phase. In the superradiant phase, this reflects the presence of complex-eigenvalue repulsion characterized by a  $p(s) \sim s^3$  suppression at small energy spacings, which is consistent with Eq. (2.7). On the other hand, in the normal phase, we find  $p(s) \sim s$ , consistent with Eq. (2.6). This corresponds to the absence of level repulsion in the  $2D$  complex plane [17].

<sup>1</sup>We are assuming that the positivity-conservation property of Liouvillians is irrelevant to the spacing distribution of the Ginibre Unitary Ensemble [17].

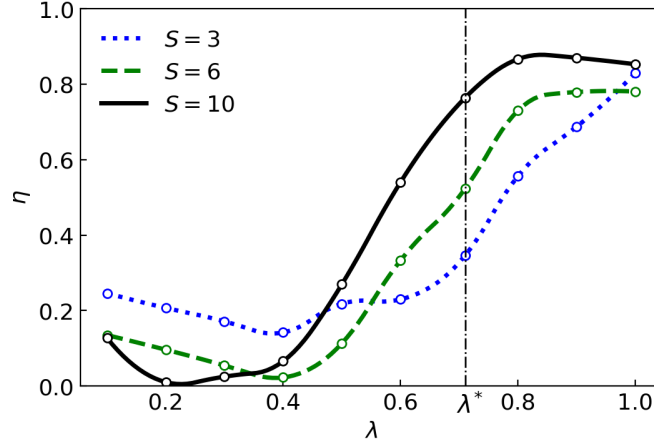


Figure 3.3: The metric  $\eta$  defined in Eq. (3.10) as we increase the coupling  $\lambda$  from the normal phase to the superradiant phase. It shows the crossover of the complex-eigenvalue spacing distribution from integrable ( $\eta \sim 0$ ) to RMT ( $\eta \sim 1$ ) predictions. The crossover sharpens as we increase the system size. At  $\lambda = 0$  the dissipative cavity decouples from the spin. Hence, the spectrum is expected to display pathological statistics away from any universal behavior. This explains the observed discrepancies close to  $\lambda = 0$ .

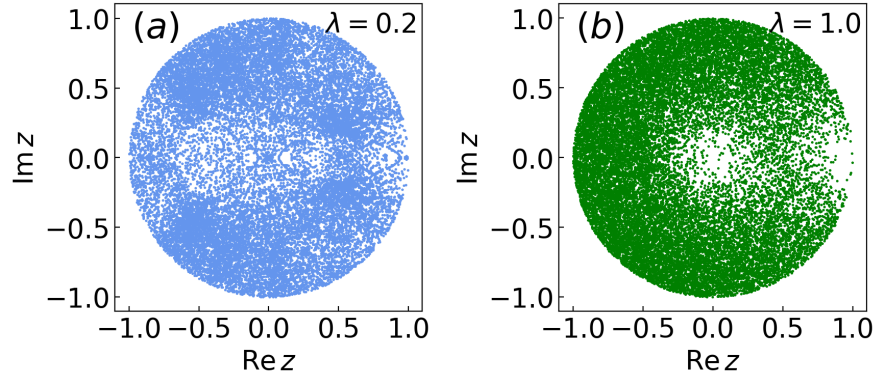
In order to better quantify the nature of the statistics as one crosses from one phase to another, we introduce the metric motivated by Refs. [139, 153, 154]

$$\eta \equiv \frac{\int_0^\infty ds [p(s) - p_{2D-P}(s)]^2}{\int_0^\infty ds [p_{\text{GinUE}}(s) - p_{2D-P}(s)]^2}. \quad (3.10)$$

By construction,  $\eta$  vanishes when the numerically obtained distribution  $p(s)$  approaches the  $2D$  Poisson distribution, whereas  $\eta$  goes to 1 when  $p(s)$  approaches the GinUE prediction. Fig. 3.3, showing  $\eta$  versus  $\lambda$ , exhibits the crossover from a  $2D$  Poisson distribution to that of GinUE prediction as one crosses the critical point. This crossover sharpens with increasing the system size.

### 3.2.2 Complex-plane generalization of the consecutive level-spacing ratio

Until now, we only probed spectral statistics using the Euclidean distance  $s$  between complex levels. To extract the angular information we resort to a recently introduced



$\lambda$	2D Poisson	0.2	0.4	0.6	0.8	1.0	GinUE
$-\langle \cos \theta \rangle$	0	0.00	0.09	0.19	0.23	0.24	0.24
$\langle r \rangle$	0.67	0.69	0.71	0.72	0.74	0.74	0.74

Figure 3.4: Scatter plot of the complex level-spacing ratio  $z$  introduced in Eq. (3.11) for  $S = 10$  (a) in the normal phase,  $\lambda = 0.2$ , and (b) in the superradiant phase,  $\lambda = 1.0$ . The table gives  $\langle \cos \theta \rangle$  and  $\langle r \rangle$  for a range of  $\lambda$  values, along with their prediction from the 2D Poisson distribution and GinUE RMT.

diagnostic [124] involving the level-spacing ratio

$$z_i = r_i e^{i\theta_i} = \frac{E_i^{\text{NN}} - E_i}{E_i^{\text{NNN}} - E_i}, \quad (3.11)$$

where superscripts NN (NNN) stand for nearest (next-nearest) neighbor. Eq. (3.11) is the generalization of the well-known adjacent gap ratio [70, 121] defined for isolated quantum systems. It captures information about next-nearest neighbors which is missed in the conventional diagnostics of level-spacing statistics. An additional advantage of this quantity is that it does not rely on the unfolding procedure which may sometimes be ambiguous and unreliable. In Fig. 3.4, we show the scatter plots of  $z_i$  below and above the critical point. The anisotropy in the superradiant phase is another signature of connection to RMT [124]. To quantitatively compare with the predictions of 2D Poisson and GinUE RMT, we report  $\langle r \rangle$  and  $\langle \cos \theta \rangle$  for a range of  $\lambda$  values in the table below Fig. 3.4 and in the convergence test of data in Fig. 3.6.

### 3.2.3 Convergence of the statistical properties of the spectrum with respect to the cavity cutoff

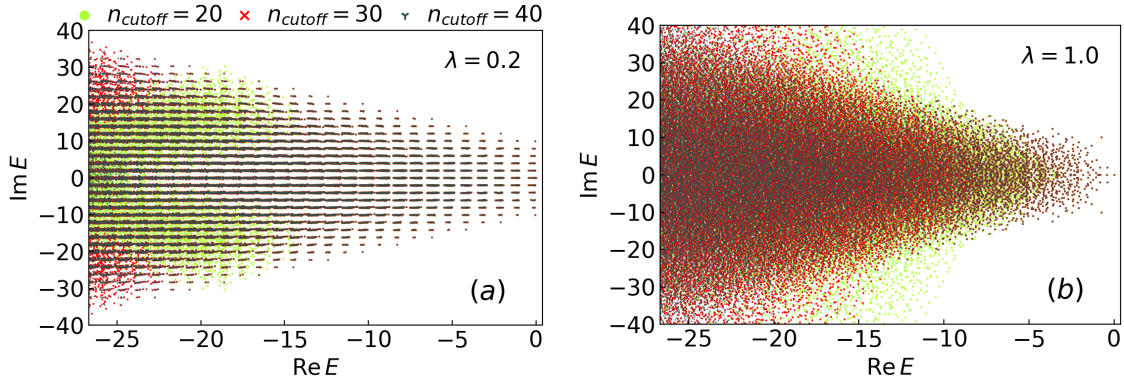


Figure 3.5: Scatter plot of the Liouvillian spectrum of the dissipative Dicke model for different  $n_{\text{cutoff}} = 20, 30, 40$  in (a) the normal phase,  $\lambda = 0.2$  and (b) the superradiant phase,  $\lambda = 1.0$  ( $S = 10$ ).

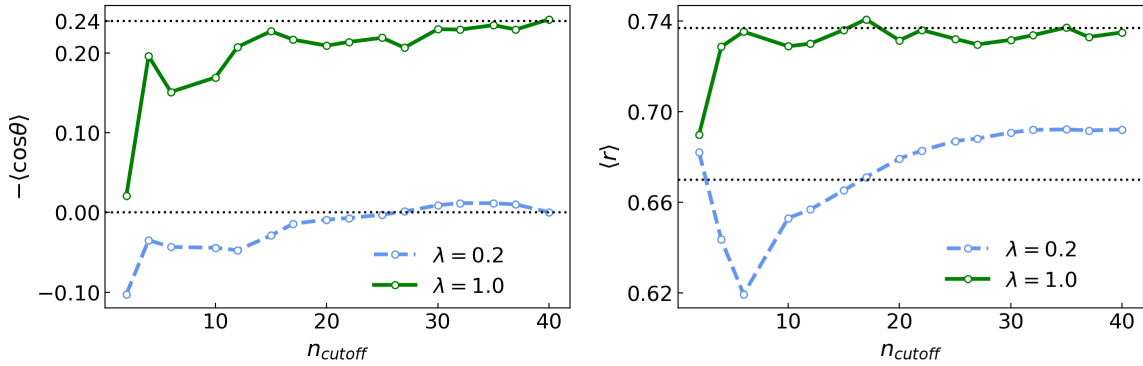


Figure 3.6:  $\langle \cos \theta \rangle$  and  $\langle r \rangle$  versus  $n_{\text{cutoff}}$ , computed from the consecutive complex level-spacing ratio distribution of  $z$  introduced in Eq. (3.11) ( $S = 10$ ).

While the introduction of a finite  $n_{\text{cutoff}}$  is essential to the numerical diagonalization of the Liouvillian, the repercussions on the resulting spectrum must be dealt with care. In Fig. 3.5, we plot the spectrum of  $\mathcal{L}$  both in the normal and in the superradiant phase for different values of  $n_{\text{cutoff}} = 20, 30, 40$  and focusing on the window  $\text{Re } E \in [-\frac{2}{3} \times 40 \kappa, 0]$ . In the normal phase, the three cutoffs yield the same highly patterned spectrum in the window  $\text{Re } E \in [-10 \kappa, 0]$ . The patterned region of the spectrum grows as  $n_{\text{cutoff}}$  is increased. For  $n_{\text{cutoff}} = 40$ , the whole window  $\text{Re } E \in [-\frac{2}{3} \times 40 \kappa, 0]$  is patterned. In

the superradiant phase, convergence is obtained in the window  $\text{Re } E \in [-5\kappa, 0]$ . Rather than the convergence of the eigenvalues, it is more important to ensure the convergence of their spectral statistics. In Fig. 3.6, we follow the convergence of properties extracted from the consecutive level-spacing ratio distribution [124] introduced in Eq. (3.11). Both  $\langle r \rangle$  and  $\langle \cos \theta \rangle$  remarkably converge when  $n_{\text{cutoff}} \approx 30$ . All results presented in the main text are produced with  $n_{\text{cutoff}} = 40$ .

### 3.3 Summary of results and conclusions

We investigated how the presence of a dissipative quantum phase transition driven by an integrability-breaking term affects the spectral statistics of the complex Liouvillian spectrum of open quantum systems. Working in the framework of the dissipative Dicke model, we found the spectral features of integrability to be robust against the integrability-breaking perturbation until the onset of the dissipative quantum phase transition. In the symmetry-broken phase, they are eventually replaced by RMT features indicative of chaotic dynamics.

# Chapter 4

## Transition to chaos in extended systems and their quantum impurity models

The Tavis-Cummings (TC) model [155, 156], a close variant of the Dicke model Hamiltonian, is widely studied in quantum optics as a model for light-matter interaction. It describes a single-quanta light field interacting with an ensemble of  $N$  two-level atoms. The Hamiltonian  $H_i$  defined in Eq. (4.1) undergoes a zero-temperature quantum phase transition (normal and superradiant phases) in  $N \rightarrow \infty$  limit like Dicke model. Dicke model also shows spectral transition (integrable-chaos) across the critical point of the quantum phase transition but TC model is Bethe ansatz integrable [157] for any value of spin-cavity coupling. In this work, we consider a collection of TC model units loaded on a tight-binding lattice. For a finite hopping amplitude, the integrability of the Tavis-Cummings lattice (TCL) model is expected to break, resulting in chaos.

The TC model has a large local Hilbert space and is known to be integrable. When loaded on a finite lattice, the integrability is expected to be broken and the chaos to set in at finite values of the hopping amplitude. As an associated impurity model, we shall consider the single-site TC model driven by a coherent source mimicking the coupling to neighbors and breaking the integrability of the undriven impurity.

After we introduce the TCL and its associated impurity model, we characterize their respective transition from integrability to chaos by means of extensive exact-diagonalization computations. We extract the statistical properties of their spectra and

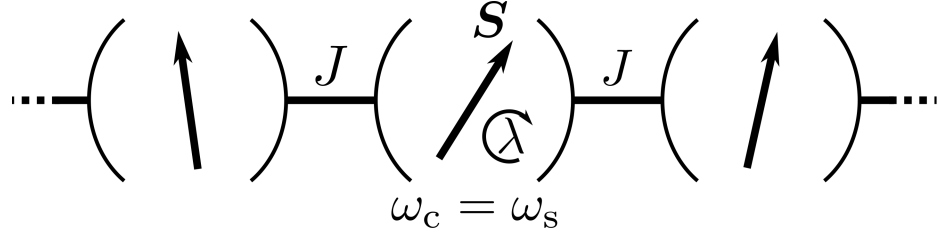


Figure 4.1: Tavis-Cummings lattice (TCL): Tavis-Cummings units hosted on a one-dimensional tight-binding lattice of size  $L$  with open boundary conditions. Each unit features a large spin  $S$  coupled to a bosonic mode via the interaction  $\lambda$ .  $J$  sets the hopping amplitude of the bosons between neighboring units. See the Hamiltonian in Eq. (4.1).

compute their level-spacing distributions, adjacent gap ratios, and spectral form factors. We find the spectral properties of the TCL to transition from Poisson statistics to those of random matrix theory (RMT) as one increases the hopping amplitude. Remarkably, the spectral form factors are computed from disorder-free models and without averaging over any model parameter. We show that the associated impurity model can successfully reproduce the spectral features of the lattice model and we compute the map between the integrability-breaking parameters of both models.

## 4.1 Tavis-Cummings Lattice (TCL)

We consider the following Hamiltonian for the TCL to describe an extended array of TC model units,

$$\begin{aligned}
 H &= \sum_{i=1}^L h_i + \sum_{\langle ij \rangle} h_{ij}, \tag{4.1} \\
 h_i &= \omega_c a_i^\dagger a_i + \omega_s S_i^z + \frac{\lambda}{\sqrt{S}} \left( a_i^\dagger S_i^- + a_i S_i^+ \right), \\
 h_{ij} &= -\frac{J}{2} \left( a_i^\dagger a_j + a_j^\dagger a_i \right),
 \end{aligned}$$

where individual Tavis-Cummings (TC) models, with Hamiltonians  $h_i$ , are loaded on a one-dimensional tight-binding lattice with  $L$  sites and open boundary conditions.  $a_i$  ( $a_i^\dagger$ ) is the bosonic annihilation (creation) operator of the cavity mode at site  $i$  with energy  $\omega_c$ .  $S_i^\alpha$ ,  $\alpha = x, y, z$ , are the spin angular momentum operators built from the totally symmetric representation of  $S$  identical two-level systems with energy splitting

$\omega_s$ . Throughout the chapter, we consider the resonant regime  $\omega_c = \omega_s = \omega_0$  and set the unit of energy  $\omega_0 = 1$ .  $\lambda$  sets the interaction strength between spins and cavity modes.  $h_{ij}$  introduces coherent hopping amplitude  $J > 0$  between the nearest-neighbor cavity modes. In the atomic limit,  $J = 0$ , one recovers the physics of the single-site TC model: in the  $S \rightarrow \infty$  limit,  $\lambda > 1$  drives a spontaneous  $U(1)$  symmetry-breaking quantum phase transition between a normal and a superradiant phase [145, 158–161]. Notably, the TC model is integrable on both sides of the phase transition [138, 157, 162, 163]. The hopping  $J > 0$  demotes the local  $U(1)$  symmetry of the TC model to a global  $U(1)$  symmetry in the TCL model corresponding to the conservation of the total number of excitations. The normal phase of the TC model extends in the  $J$ - $\lambda$  plane of the phase diagram of the TCL model. Importantly,  $J$  acts as an integrability-breaking parameter. More precisely, for finite size lattices, the integrable character of the TC model is expected to be robust until a finite value of  $J$  which rapidly vanishes as the size of the lattice and of the local Hilbert space, respectively  $L$  and  $S$ , are increased. In practice, we explore the onset of chaos by working at  $L = 3$  cavities, which is experimentally feasible and relevant.

Furthermore, while that the spin-boson scaling factor  $1/\sqrt{S}$  in Eq. (4.1) is conventionally introduced to ensure non-trivial thermodynamics in the  $S \rightarrow \infty$  limit, we will show below that a proper dynamic scaling can be introduced for the cavity-cavity nearest-neighbor hopping parameter  $J$ . This is due to the fact that it breaks the system's integrability, and as the system size increases, the integrability regime becomes suppressed. Based on the available finite system size data, it remains challenging to conclusively determine whether integrability persists in the thermodynamic limit. Motivated by the work of Bulchandani, Huse, and Gopalakrishnan work in ref. [164], finite-size scaling—where plots for various system sizes collapse onto one another—provides supporting evidence that the integrability regime remains robust up to a certain parameter value. However, in the thermodynamic limit, this requires additional rescaling, with  $J \rightarrow J/S^{1/4}$ . In this work, we present adjacent gap ratio  $\langle r \rangle$  data with  $J$  scaled by the spin size  $S$ . These results demonstrate that the integrability-to-chaos crossover becomes independent of the spin size  $S$  for a fixed lattice size  $L$ .

## 4.2 Impurity model

Let us now introduce the impurity model associated to the above lattice model. It is given by the Hamiltonian

$$H_{\text{imp}} = \omega_c a^\dagger a + \omega_s S^z + \frac{\lambda}{\sqrt{S}} (a^\dagger S^- + a S^+) - \mu \sqrt{S} (a + a^\dagger). \quad (4.2)$$

It corresponds to a single-site TC model with an additional drive term controlled by the parameter  $\mu$ . Similarly to the lattice model, we set  $\omega_c = \omega_s = \omega_0$ . Note that the parameter  $\omega_0$  of the impurity can in principle be different from the one of the lattice model but, for simplicity, we also set it as the unit of energy. Similarly to the integrability-breaking parameter  $J/\lambda$  that lifts the local  $U(1)$  symmetry of the lattice model to a global  $U(1)$  symmetry, the impurity drive  $\mu \neq 0$  explicitly breaks the  $U(1)$  symmetry as well as the integrability of the TC model. Note that the scaling factors of the spin-boson interaction and the drive in  $H_{\text{imp}}$ , respectively  $1/\sqrt{S}$  and  $\sqrt{S}$ , ensure non-trivial thermodynamics in the  $S \rightarrow \infty$  limit. While we follow that convention, we shall see later that a proper dynamic scaling, in the sense of Bulchandani, Huse, and Gopalakrishnan in Ref. [164] (discussed in the above section), requires rescaling the drive  $\mu$  with a factor  $1/S^{1/4}$  rather than  $\sqrt{S}$ . Similar single-site models have been used in the literature to study the stability of the superradiant phase-transition and the onset of quantum chaos [165, 166]. Intuitively, the drive term in  $H_{\text{imp}}$  can be seen as mimicking the hopping from the rest of the lattice on the impurity site. In that view,  $\mu$  is expected to depend on the size and the precise geometry of the lattice, and it vanishes in the atomic limit  $J \rightarrow 0$ . We motivate our choice of impurity model in Eq. (4.2) from the fact that in the dynamic scaling regime, where the integrability-breaking parameter  $J/\lambda$  is small, it can be derived from a lattice model with a large coordination number using a standard mean-field approach. In other words, such term can be thought of as effectively a mean field decoupling from the rest of the lattice sites. We refer the reader to the Appendix [B] for a detailed presentation of this construction. Notably, we found the classical version of the driven impurity model to unambiguously exhibit chaotic dynamics for intermediate values of  $\mu$ . We refer the reader to the Section [4.4] for a detailed analysis. The conjecture by Bohigas, Giannoni and Schmit (BHS) [28] states that those Hamiltonians with a chaotic classical limit have spectra whose statistical features are governed by RMT. As a consequence, we expect the quantum impurity

model in Eq. (4.2) to exhibit RMT features.

### 4.3 Spectral properties

We analyze the statistical properties of the eigenvalues  $\{E_n\}$  of both the lattice Hamiltonian  $H$  in Eq. (4.1) and the impurity Hamiltonian  $H_{\text{imp}}$  in Eq. (4.2) by means of exact diagonalization. Given the spatial reflection symmetry and the  $U(1)$  symmetry of the finite lattice model, we choose to compute the spectral statistics from the reflection-symmetric sector with a fixed number of excitations, labeled by the quantum number  $N_{\text{ex}} = 36$ . Therefore, the spectral statistics that we extract are independent of  $\omega_0$ . However, given the lack of such symmetry in the impurity model, in principle, one has to consider its whole spectrum. In practice, given the infinitely large bosonic Hilbert space of the cavity, we truncate it to a finite number of excitations  $n_{\text{cutoff}} = 2^{10}$ . We use standard algorithms with double precision. To provide statistics that are converged with respect to  $n_{\text{cutoff}}$ , we discard the upper 50% of the impurity eigenvalues. Additionally, contrary to the lattice model whose spectrum was found to be statistically uniform throughout, the spectrum of the impurity model can be mixed: a low-energy portion with integrable statistics, and an intermediate to high-energy portion with chaotic statistics. Such features were already reported for similar models [139, 167–169] and are consistent with the classical analysis presented in Section [4.4]. Hence, we focus on an intermediate energy range, discarding about the first 10% of the spectrum.

#### 4.3.1 Level-spacing statistics

In order to unveil the universal footprints of these spectra as well as the crossover regime between integrability and chaos, we study the level-spacing statistics of the TCL and its associated impurity model as their respective integrability-breaking parameters are turned on. First, we perform an unfolding of the spectra using standard procedures, see the details in Appendix [A]. The unfolded spectra are then used to generate the histograms of the gaps  $s$  between nearest-neighbor eigenvalues, yielding the spacing distributions  $p(s)$ . The results obtained for the lattice model are summarized in the top panel of Fig. 4.2 for weak, intermediate, and strong values of the integrability-breaking parameter  $J/\lambda$ . For comparison, we also plot the corresponding spacing distributions for independent random numbers, namely the Poisson distribution  $p_{\text{Poisson}}(s)$

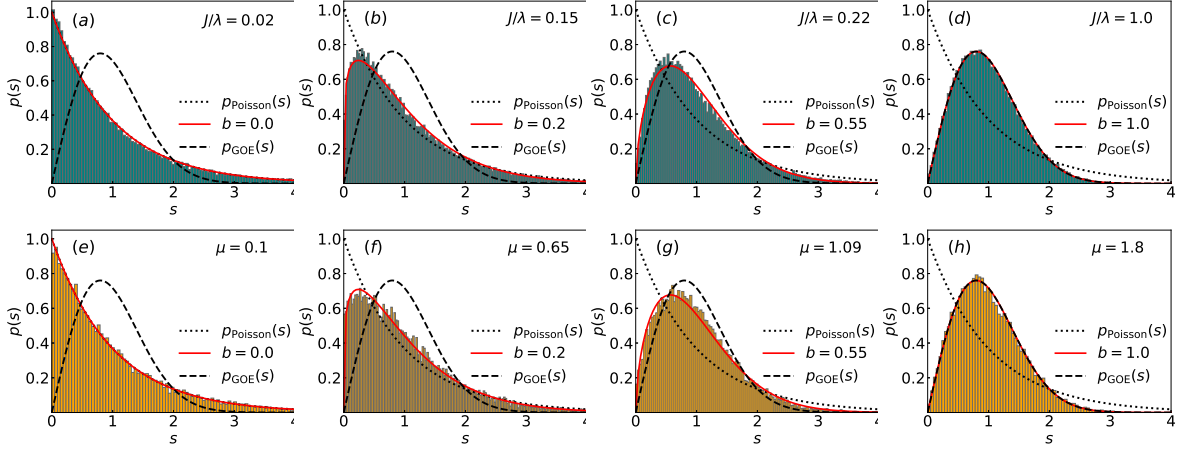


Figure 4.2: Distribution of level spacings  $p(s)$  in the crossover regime from integrability to chaos (left to right). The top panel is computed from the exact diagonalization of the Tavis-Cummings lattice ( $L = 3$  sites) with spin  $S = 8$ , for (a)  $J/\lambda = 0.02$ , (b)  $J/\lambda = 0.15$ , (c)  $J/\lambda = 0.22$  and (d)  $J/\lambda = 1.0$ . The bottom panel is computed from the corresponding impurity model with  $S = 64$  and  $\lambda = 1$ , for (e)  $\mu = 0.1$ , (f)  $\mu = 0.65$ , (g)  $\mu = 1.09$  and (h)  $\mu = 1.8$ . The red curves correspond to fits to the Brody distribution defined in Eq. (4.3), with the single fitting parameter  $b$  given in the legend. The values of the impurity  $\mu$  are chosen such that  $b$  is the same between the lattice and the impurity.

defined in Eq. (2.5) as well as the corresponding distribution for the eigenvalues of GOE-Hermitian random matrix ensemble,  $p_{GOE}(s)$  defined in Eq. (2.3) for Hamiltonian with time-reversal symmetry.

The distributions computed from the spectrum of  $H$  are in remarkable agreement with Poisson in the weak hopping regime, and with the GOE RMT prediction in the strong hopping regime. The case of the Jaynes-Cummings lattice ( $S = 1$ ) has been studied at small filling fraction in Ref. [170].

We also compute the level-spacing statistics of the impurity model in both the integrable and RMT regime, as well as in the intermediate crossover regime. See the bottom panel of Fig. 4.2. The impurity statistics successfully reproduce the ones found on the lattice side in all these regimes. Let us better quantify the agreement between the TCL and its associated impurity model by performing a single-parameter numerical fit of all the computed spacing distributions to the following Brody distribution

$$P_B(b, s) = (b + 1)\eta s^b e^{-\eta s^{b+1}}, \quad \eta = \Gamma\left(\frac{b+2}{b+1}\right)^{b+1}, \quad (4.3)$$

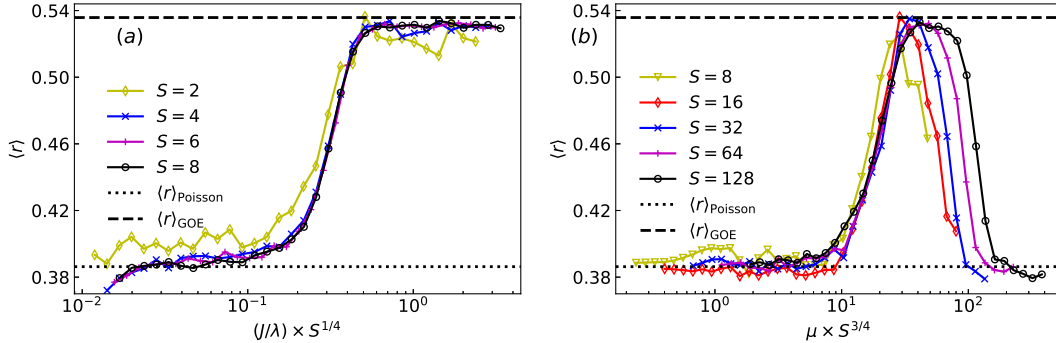


Figure 4.3: Adjacent gap ratio  $\langle r \rangle$  in the crossover regime from integrability to chaos. (a) Tavis-Cummings lattice ( $L = 3$  sites) as  $J/\lambda \times S^{1/4}$  is tuned from weak to strong hopping. (b) Corresponding impurity model as a function of the drive  $\mu \times S^{3/4}$  for fixed  $\lambda = 1$ . Other choices of  $\lambda$  yield similar results. The collapse of the different curves is used to identify the dynamic scaling with respect to local spin size  $S$ .

where  $\Gamma(x)$  is the gamma function. The transition from RMT to Poisson statistics has already been extensively studied in a variety of models [33, 171–175] and the Brody distribution was heuristically proposed to interpolate between the Poisson and the GOE regimes [171, 176]. We found it to be better suited than other interpolating distributions such as the one corresponding to the Rosenzweig-Porter for  $2 \times 2$  matrices. The results of the fitting procedure are given by the red curves in Fig. 4.2 and the corresponding values of  $b$  are given in the legends. The values of  $\mu$  were chosen so as to reproduce the same values of  $b$  as that of the lattice.

### 4.3.2 Adjacent-gap ratio

As a complementary diagnostic to the spectral statistics, we compute the adjacent-gap ratio [70] that defined in Eq. (2.9), does not rely on the unfolding procedure.

For chaotic systems in the GOE class, the tabulated average adjacent gap ratio is  $\langle r \rangle_{\text{GOE}} \approx 0.53$ . For integrable cases,  $\langle r \rangle_{\text{Poisson}} \approx 0.39$ . In Fig. 4.3 (a), we report how  $\langle r \rangle$  evolves as a function of the integrability-breaking parameter  $J/\lambda$  and we identify its scaling with  $S$ . The figure displays a well-delineated ramp where  $\langle r \rangle$  crosses over from Poisson value to GOE value. We find a good collapse of that crossover ramp for different values of  $S$  when  $\langle r \rangle$  is plotted as a function of  $J/\lambda \times S^{1/4}$ . Interestingly, this implies that different sets of model parameters will produce the same adjacent gap ratio as long as  $J/\lambda \times S^{1/4}$  is kept constant. More generally, this scaling has to be interpreted in the

sense of the dynamic scaling introduced in Ref. [164]: it is the scaling that allows to control the onset of chaos when the size of the local Hilbert space is increased. Before the crossover ramp, the integrable phase is found to be robust until a finite value of  $J/\lambda \times S^{1/4} \approx 0.1$ . After the crossover ramp, we observe a large chaotic plateau where the value of  $\langle r \rangle$  is the one of the GOE ensemble. For values of  $J/\lambda \times S^{1/4}$  that are much larger than the ones shown in Fig. 4.3 (a), we found a departure from the RMT statistics. This is expected when the kinetic energy dominates over the Tavis-Cummings light-matter coupling and the model perturbatively reduces to a free bosonic tight-binding model which is integrable.

In Fig. 4.3 (b), we display the same quantity on the impurity side as a function of the integrability-breaking parameter  $\mu$  and we identify its scaling with  $S$ . The impurity model successfully reproduces the qualitative features found in the lattice model: a robust integrable regime, a crossover ramp, and a subsequent chaotic plateau. We find a good scaling collapse of that ramp when  $\langle r \rangle$  is plotted as a function of  $\mu \times S^{3/4}$ . As it will become clear later when relating both models, such a dynamics scaling of the impurity model is consistent with the one found in the lattice model. At large values of  $\mu \times S^{3/4}$ , the re-entrance of the integrable phase can be attributed to the effective screening of the interaction in the Hamiltonian [Eq. (4.2)] by a very strong drive term and is consistent with what we observed on the lattice side at very large  $J/\lambda \times S^{1/4}$ . For both lattice and impurity models, we also checked that the entire adjacent-gap ratio distribution  $P(r)$  [121–123] converges to those universal distributions expected in the integrable and the chaotic regimes.

### 4.3.3 Map between lattice and impurity models

Above, we have characterized the integrable-to-chaotic crossover of the level-spacing distribution via its Brody parameter  $b$ , as well as the one of the adjacent gap ratio  $\langle r \rangle$  when increasing the integrability-breaking parameters, namely  $J/\lambda$  in the lattice and  $\mu$  in the impurity. We use this to retrieve the relationship between the integrability-breaking parameters of both models by eliminating the fitting parameter  $b$  from the data of Fig. 4.2 and, similarly, by eliminating  $\langle r \rangle$  from the data of Fig. 4.3. In practice, we identify the functions  $\alpha = f_1(J/\lambda)$  and  $\alpha = f_2(\mu)$  where  $\alpha = b, \langle r \rangle$  and find  $\mu = f_2^{-1}(f_1(J/\lambda))$ . Note that these functions are only invertible in the crossover region. The resulting maps  $\mu(J/\lambda)$  for different impurity sizes  $S$  are displayed in Fig. 4.4 for a fixed lattice size

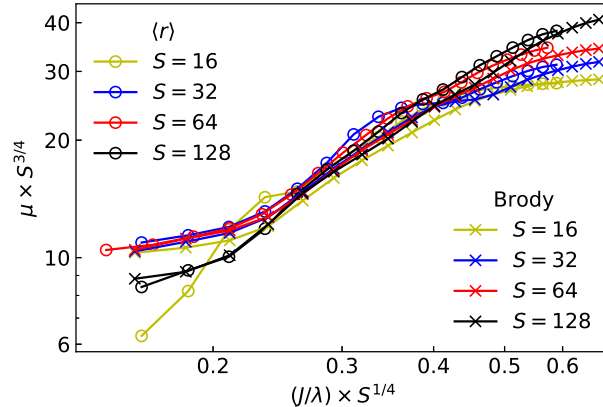


Figure 4.4: Map between the integrability-breaking parameters of the lattice and impurity models,  $J/\lambda$  and  $\mu$ , respectively. The scalings with  $S$  on both axis are deduced from the dynamic scalings identified in Fig. 4.3. The map is numerically extracted from the level-spacing Brody parameters  $b$  determined in Fig. 4.2 as well as from the data of the adjacent gap ratio  $\langle r \rangle$  of Fig. 4.3. The methodology is explained in Section [4.3.3].  $L = 3$  and  $S = 8$  on the lattice side and the different impurity spin sizes are given in the legend.

$L = 3$  and  $S = 8$ . We use the dynamic scaling identified in Fig. 4.3. The resulting maps obtained from the level-spacing distributions are similar to those obtained from the adjacent gap ratio, and the agreement seems to improve as  $S$  is increased. Notably, this reveals that the impurity  $\mu$  is a non-linear function of the lattice  $J/\lambda$ . From a mean-field point of view, this map has to be understood as the self-consistent relation tying together the TCL model with its impurity counterpart.

#### 4.3.4 Spectral form factor

We now turn to another diagnostic that probes the long-range correlations in the spectrum, namely the spectral form factor (SFF) [26] that we introduced in Section [2.3] and discussed in detail.

SFF is typically not a self averaged quantity and  $\langle \dots \rangle$  in Eq. (2.16) denotes averaging with respect to disorder sampling. For our clean system, we replace this disorder average by dividing the unfolded spectrum into samples of  $N = 100$  consecutive eigenvalues and by averaging over those samples. In this chapter, SFF notation is presented as  $K(t)$ , where  $K(t) = K(\tau, N = 100)$ . We use shorthand notation for SFF expressions for

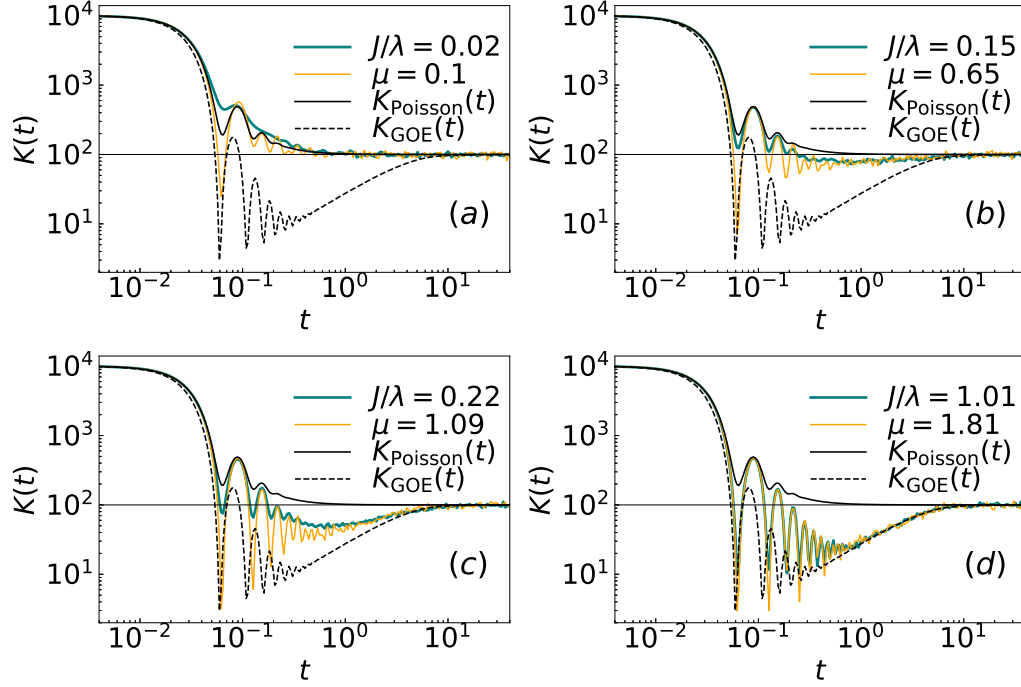


Figure 4.5: Spectral form factors of the lattice model with  $L = 3$  and  $S = 8$  and of the impurity model with  $S = 64$  for increasing values of the integrability-breaking parameters  $J/\lambda$  (lattice) and  $\mu$  (impurity) given in the legends and chosen as in Fig. 4.2. The plain and dashed black lines correspond to the Poisson and GOE distributions, respectively.

GOE-RMT and Poisson numbers defined in Eqs. (2.18, 2.23), for fixed  $N$  as follows,

$$K_{GOE}(t) = K^{GOE}(\tau, N), \quad (4.4)$$

$$K_{Poisson}(t) = K^P(\tau, N). \quad (4.5)$$

This is justified by the expectation that the statistics are similar throughout the spectrum. The resulting SFF for the lattice and the impurity model are presented in Fig. 4.5 for the same parameters as in Fig. 4.2. We compare these findings to the predictions of the relevant random matrix ensembles [26, 177–182]. The SFF of the GOE-RMT is defined in Eq. (4.4) for asymptotically at large  $N$ .

As shown in Fig. 4.5, the early-time behavior of SFF, its dip, and subsequent oscillations, are dominated by non-universal features of the spectrum. In the intermediate to

long-time regime, the linear ramp between Thouless and Heisenberg times and the subsequent plateau are well-known universal signatures of quantum chaos. On the integrable side, the SFF for Poissonian levels with unit mean level spacing is defined in Eq. (4.5) is the lack of such features and has power-law decay in the intermediate time regime. In stark contrast to the chaotic case, the SFF of integrable dynamics does not show the linear ramp. In the fully developed integrable and chaotic regimes, our results in Fig. 4.5 are in excellent agreement with those universal predictions given in Eqs. (4.4, 4.5). More importantly, this also clearly demonstrates that the SFF of the lattice and the impurity models are in quantitative agreement with each other throughout the crossover region between the integrable and chaotic regimes.

## 4.4 Chaos in the classical limit of Impurity model

In this section, we discuss the integrability to the chaotic crossover of the classical limit of the dynamics of the impurity model [139, 166]. We recall that the quantum Hamiltonian of the impurity model reads

$$H_{\text{imp}} = \omega_c a^\dagger a + \omega_s \left( S^z + \frac{S}{2} \right) - \sqrt{S} \mu (a^\dagger + a) + \frac{\lambda}{\sqrt{S}} (a^\dagger S^- + S^+ a) . \quad (4.6)$$

Note that we do not consider the dynamic scaling regime here. The corresponding classical Hamiltonian is obtained in three steps:

(i) Express the spin operators in terms of bosonic operators using the Holstein-Primakoff transformation, yielding,

$$H_{\text{imp}} = \omega_c a^\dagger a + \omega_s b^\dagger b - \sqrt{S} \mu (a^\dagger + a) + \frac{\lambda}{\sqrt{S}} \left( a^\dagger \sqrt{S - b^\dagger b} b + b^\dagger \sqrt{S - b^\dagger b} a \right) . \quad (4.7)$$

(ii) Writing the resulting Hamiltonian in terms of position and momentum operators defined as,

$$\begin{aligned} \hat{x}_c &:= \frac{1}{\sqrt{2\omega_c}} (a^\dagger + a) , \quad \hat{p}_c := i\sqrt{\frac{\omega_c}{2}} (a^\dagger - a) , \\ \hat{x}_s &:= \frac{1}{\sqrt{2\omega_s}} (b^\dagger + b) , \quad \hat{p}_s := i\sqrt{\frac{\omega_s}{2}} (b^\dagger - b) . \end{aligned} \quad (4.8)$$

(iii) Taking the classical limit, by replacing position and momentum operators by real numbers. This yields the classical Hamiltonian

$$H_{\text{imp}}^{\text{cl}} = \frac{1}{2} (p_c^2 + \omega_c^2 x_c^2 - \omega_c) + \frac{1}{2} (p_s^2 + \omega_s^2 x_s^2 - \omega_s) + \lambda \left( \sqrt{\omega_c \omega_s} x_c x_s + \frac{p_c p_s}{\sqrt{\omega_c \omega_s}} \right) \eta(p_s, x_s) - \sqrt{S} \mu \sqrt{2\omega_c} x_c, \quad (4.9)$$

where  $\eta(p_s, x_s) := \sqrt{1 - (p_s^2 + \omega_s^2 x_s^2 - \omega_s) / 2\omega_s S}$ .

We consider the  $S \rightarrow \infty$  limit by first rescaling the position and momentum coordinates as  $(x_c, p_c, x_s, p_s) \mapsto \sqrt{S} \times (x_c, p_c, x_s, p_s)$ , and the energies as  $E \mapsto S \times E$ . We obtain the following classical Hamilton's equations of motion [3]

$$\begin{aligned} \frac{d}{dt} x_c &= p_c + \frac{\lambda}{\sqrt{\omega_c \omega_s}} \tilde{\eta}(x_s, p_s) p_s, \\ \frac{d}{dt} p_c &= -\omega_c^2 x_c - \lambda \sqrt{\omega_c \omega_s} \tilde{\eta}(x_s, p_s) x_s + \sqrt{2\omega_c} \mu, \\ \frac{d}{dt} x_s &= p_s + \frac{\lambda}{\sqrt{\omega_c \omega_s}} \left[ \tilde{\eta}(x_s, p_s) p_c - \frac{1}{2\omega_s \tilde{\eta}(x_s, p_s)} \left( \omega_c \omega_s x_c x_s + p_c p_s \right) p_s \right], \\ \frac{d}{dt} p_s &= -\omega_s^2 x_s - \lambda \sqrt{\omega_c \omega_s} \left[ \tilde{\eta}(x_s, p_s) x_c - \frac{1}{2\omega_c \tilde{\eta}(x_s, p_s)} \left( \omega_c \omega_s x_c x_s + p_c p_s \right) x_s \right], \end{aligned} \quad (4.10)$$

where  $\tilde{\eta}(x_s, p_s) = \sqrt{1 - (p_s^2 + \omega_s^2 x_s^2) / 2\omega_s}$ . Note that the phase space is constrained by  $0 \leq \tilde{\eta}(x_s, p_s) \leq 1$ . One simple and qualitative way to study the chaos in classical dynamics is to study Poincaré sections [3, 5]. These are obtained by numerically integrating the above equations of motion, with the initial conditions set by  $x_c(0), p_c(0), x_s(0), p_s(0)$  and the energy  $E$ . The trajectories are projected on a chosen two-dimensional section. We choose it to be the intersection between the hypersurface of constant energy  $E$ , the hypersurface of equation  $p_s(t) = 0$ , and the  $(x_c, p_c)$  plane. Regular and structured Poincaré sections indicate integrable dynamics, whereas erratic and random structures indicate chaotic dynamics.

The Poincaré sections generated for various initial conditions with different energies and for various values of the drive  $\mu$  are displayed in Fig. 4.6. At small values of  $\mu$

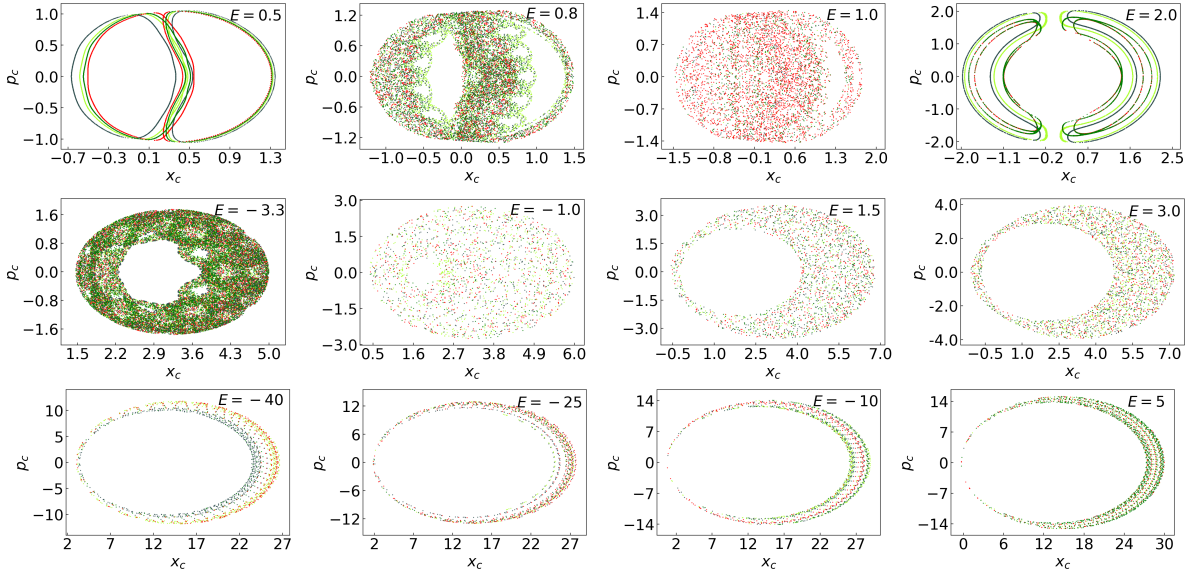


Figure 4.6: Poincaré sections of the classical driven impurity model defined in Eq. (4.9) in the limit  $S \rightarrow \infty$ ,  $\lambda = 1.0$ , and for various energies  $E$  and (top) weak drive  $\mu = 0.1$ , (middle) intermediate drive 1.8, (bottom) strong drive 10.0. Different colors represent trajectories with different initial conditions

( $\mu = 0.1$ ), Poincaré sections are regular except for a small intermediate energy window where the dynamics are chaotic. This indicates a relative robustness of the  $\mu = 0$  integrable phase. If one views this phenomena through the lens of an energy-resolved version of Bohigas, Giannoni, and Schmit (BGS) conjecture, it hints at the presence of extensive (in  $S$ ) low-energy and high-energy portions of the spectrum of the *quantum* impurity model whose universal features are dictated by Poisson statistics.

At intermediate values of the drive  $\mu$  ( $\mu = 1.8$ ), we observed chaotic dynamics at all the energies we numerically investigated. This hints at a quantum spectrum with statistical features dictated by random matrix theory. Interestingly, at very large values of  $\mu$  ( $\mu = 10$ ), we observed close-to-integrable features at all energies. We attribute this to a drive term which is so strong that it effectively screens the effect of the non-linearity  $\lambda$  that is responsible for chaos. The same reasoning can be applied to the quantum version of the model.

## 4.5 Summary of results and conclusions

In this work, we argued that the universal spectral features of a spatially extended system can be captured by a minimal impurity model with a much smaller Hilbert space. This impurity modeling is inspired from what is routinely done to capture local physics in the *thermodynamic* scaling regime. Here, we proposed to extend this approach to the *dynamic* scaling regime to capture spectral features at the onset of chaos. The validity of this approach was tested by comparing spectral statistics computed on both the lattice and the impurity side. A complementary test would be to compare the chaotic features of out-of-time-order correlators. Note that we have treated the integrability-breaking parameter  $\mu$  as freely adjustable. This is similar to proving that a single spin coupled to a carefully chosen Weiss field is a faithful impurity representation of an extended magnet in that it can *exactly* reproduce its magnetization. However, an exciting challenge remains: *analytically* identifying the relationship between the lattice problem and its impurity that self-consistently determines the amplitude of the integrability-breaking drive term. This means analytically deriving the map between  $J/\lambda$  and  $\mu$  that has been numerically computed in Fig. 4.4. Although our elementary implementation relied on a single-site impurity driven by a static source, its generalization to larger impurities (*e.g.* to accommodate larger LIOMs, increase the local Hilbert space) or more complex environments is not expected to bring extra conceptual difficulty. Adapting this approach to other lattice models relies on: (i) the impurity model featuring a tunable integrability-breaking term analogous to our  $\mu$ , (ii) a local (impurity) Hilbert space which is large enough to ensure sufficient spectrum data for universal statistics to develop.

As a side note, we found that both the quantum and the classical versions of our impurity model exhibit a rich phenomenology, with regimes of chaos and integrability simultaneously present at different energies, see the Section [4.4]. Similar observations were made in various other models [166, 167, 183–185]. The classical-to-quantum correspondence of such models with mixed phase space is still an open question that could be investigated through the lens of an energy-resolved extension of BGS conjecture.

# Chapter 5

## Long-ranged spectral correlations in eigenstate phases

In this chapter, we investigate the utility of long-range spectral probes: Spectral form factor (SFF) and density of all gaps (DOG) that are introduced and discussed to great detail in Chapter [2]. We use these probes in characterizing and distinguishing between the MBL and ergodic phases further. First, we extend the results of previous work in Ref. [83] where an analytical form for SFF was obtained and verified for energy conserving systems with quenched disorder. Here, we show that the SFF form is also applicable to quasiperiodic systems (deterministic potentials) and Floquet systems (which do not conserve energy). Second, we study a quantity related to the Fourier transform of the SFF, the distribution of all spectral gaps that we refer to as the density of gaps (DOG), for which we obtain an analytical form for Poisson numbers Eq. (2.34) and random matrices Eq. (2.31) (both of which have not been presented in the literature previously to the best of our knowledge). Using this, we show that the DOG also exhibits distinct signatures in the MBL and ergodic phases and also furnishes a means of tracking the transition between the two phases. Finally, we also clarify the robustness and universality of these spectral signatures in the MBL phase. We show that unlike the ‘ramp’ which is seen in the SFF of ergodic systems, the scaling form of the SFF in MBL systems depends on global aspects of the spectrum as a consequence of the lack of intrinsic correlations in MBL spectra. Altogether, our results show that the universal signatures present in long-range spectral probes that arise from both intrinsic correlations and global features of the spectrum can comprehensively characterize eigenstate phases

more efficiently on finite-size simulations than either intrinsic or global only.

In this work we consider three one-dimensional quantum spin chain models incorporating quenched disorder in Eq. (5.1), periodic driving (Floquet) in Eq. (5.2), and quasiperiodic detuning in Eq. (5.6), as a setup for numerical analysis. These models belong to different classes to study MBL physics and more details of these models are discussed in Section [5.1.1]. Below are the important properties of these probes (SFF and DOG) we will be focusing on in this work in the numerical study of various quantum-many body systems:

SFF: We extract the spectral form factor  $K(\tau, N)$  defined in Eq. (2.16) and compare it with the analytical form obtained from RMT shown in Eq. (2.18) in the ergodic phase and to the form obtained from Poisson numbers shown in Eq. (2.23) in the MBL phase. In particular, we verify that deep in the MBL phase we observe the power law scaling shown in Eq. (2.24). The SFF plots are shown in Fig. 5.1 for above mentioned models and defined in Eqs. (5.1, 5.2, 5.6).

DOG: We compute the density of all gaps defined in Eq. (2.25) and compare it with the analytical expression obtained from RMT shown in Eq. (2.31) in the ergodic phase and to the form obtained from the Poisson spectra shown in Eq. (2.34) in the MBL phase. The DOG plots are shown in Fig. 5.2 for the above mentioned models. As discussed in Section [2.4.2], we also use the appropriately normalized density of zero gaps  $[N\chi(0, N)] \in [0, 1]$  as an order parameter to track the transition between the MBL and the ergodic phases. This is shown in Fig. 5.3 where we compare the location of the transition determined by  $[N\chi(0, N)]$  with the same determined by the more conventional adjacent gap ratio ( $r$ ) defined in Eq. (2.9). Discussions on the sensitivity of numerical computations of  $\chi(x, N)$  to binning are discussed in Appendix [D].

## 5.1 Numerical study of physical models

In order to perform our numerical analysis, we employ the following prescription: From each disorder realization of the model, we extract  $N$  consecutive levels from the middle of the spectrum where  $N$  is smaller than the total number of levels  $N_R$  and then proceed to compute the SFF and DOG. This does not produce any sharp DOS features of the kind present in Eq. (2.20). We also rescaled the data to set the mean level spacing  $\mu$ , averaged across disorder samples, to 1 for convenience. Whenever we have a global  $U(1)$

symmetry, we extract the levels from the zero total magnetization sector,  $\sum_j S_j^z = 0$ . Additional details of numerical analysis, such as the number of disorder samples the data is averaged over to produce all the figures, are tabulated in Appendix [E] to reduce clutter. In general, all our numerical results are in excellent agreement with analytical predictions. We provide details of each model and comment on various features below.

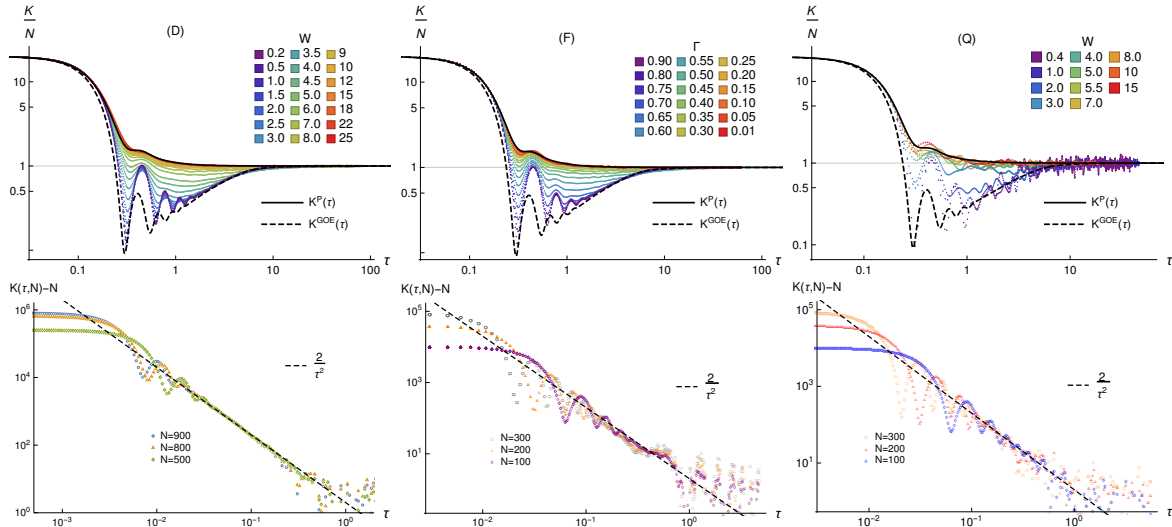


Figure 5.1: Top row: SFF [Eq. (2.16)] for  $N = 20$  levels across various disorder strengths. Bottom row: Reduced SFF deep in the MBL phase with power-law scaling. Plots in left, middle and right columns correspond to the disordered spin chain (D), Floquet spin chain (F) and quasi-periodic spin chain (Q) defined in Eqs. (5.1, 5.2, 5.6) respectively. System sizes used are (from left to right)  $L = 14, 10, 12$  for the top row and  $L = 18, 12, 16$  for the bottom row. The disorder strengths used for the bottom row is (from left to right)  $W = 25$ ,  $\Gamma = 0.01$  and  $W = 15$ .

### 5.1.1 Physical models

#### Spin chain Hamiltonian with quenched disorder

We begin with the quantum spin chain Hamiltonian with quenched disorder considered in Refs. [83, 186].

$$H = \sum_i J_1(S_i^x S_{i+1}^x + S_i^y S_{i+1}^y + \Delta S_i^z S_{i+1}^z) + w_i S_i^z + \sum_i J_2(S_i^x S_{i+2}^x + S_i^y S_{i+2}^y + \Delta S_i^z S_{i+2}^z). \quad (5.1)$$

Here and henceforth,  $S^\alpha$  are spin-half operators that can be written in terms of Pauli matrices as  $S^\alpha = \frac{1}{2}\sigma^\alpha$  and  $w_i$  are random numbers drawn from a uniform distribution  $w_i \in [-W, W]$ . Following Refs. [83, 186], we set  $J_1 = J_2 = 1.0$  and  $\Delta = 0.55$ . This Hamiltonian has  $U(1)$  spin-rotation symmetry which allows us to work with the spectrum of the zero magnetization sector (half-filling) for numerical analysis. Variants of this model have been previously studied [187, 188] and are known to have a thermal phase at weak disorder and an MBL phase in strong disorder, as can be seen by tracking the adjacent gap ratio ( $r$ ) defined in Eq. (2.9). As shown in Fig. 5.3 (top row, left column), tracking the adjacent gap ratio indicates that the strength of the critical disorder is somewhere near  $W_c \approx 7.3$  where the curves cross for different sizes of the system.

### Floquet spin chain with quenched disorder

Local conservation laws produce diffusive hydrodynamic modes that can slow down dynamics and obscure the thermalization properties of the system [52]. Periodically driven Floquet systems with quenched disorder and no global symmetries serve as a useful testing ground for studying eigenstate phases because they contain no conservation laws, including energy. As a result, the system is allowed to thermalize rapidly in the ergodic phase, leading to a sharper MBL-ergodic transition. Now we consider the Floquet model defined in Ref. [189]. This is described by the following Floquet unitary operator that generates the time evolution for one time period,  $2T$

$$U(T) = \exp\left(-i\frac{T}{2}H_x\right) \exp(-iTH_z) \exp\left(-i\frac{T}{2}H_x\right), \quad (5.2)$$

where, the Hamiltonians  $H_x$  and  $H_z$  are defined as follows:

$$\begin{aligned} H_x &= g\Gamma \sum_{j=1}^L \sigma_j^x, \\ H_z &= \sum_{j=1}^{L-1} \sigma_j^z \sigma_{j+1}^z + \sum_{j=1}^L (h + g\sqrt{1 - \Gamma^2}G_j) \sigma_j^z. \end{aligned} \quad (5.3)$$

Our choice of parameters  $(g, h) = (0.9045, 0.8090)$  and the time period  $2T = 1.6$  are the same as studied in Ref. [189].  $\{G_j\}$  are independent Gaussian random numbers with zero mean and unit standard deviation where it was argued that the critical point  $\Gamma_c$  was near 0.3. For  $\Gamma < \Gamma_c$  this system is in MBL phase and for  $\Gamma > \Gamma_c$  it is ergodic.

Eigenvalues of unitary operator Eq. (5.2) are pure complex phases  $\{e^{i\theta_j}\}$  where  $\{\theta_j\}$  define the Floquet spectrum and take values on the unit circle. We will use  $\{\theta_j\}$  to study the SFF and DOG.

$$K(\tau, N) = \left\langle \sum_{m,n=1}^N e^{i\tau(\theta_m - \theta_n)} \right\rangle, \quad (5.4)$$

$$\chi(x, N) = \frac{1}{N(N-1)} \left\langle \sum_{m \neq n=1}^N \delta(x - (\theta_m - \theta_n)) \right\rangle. \quad (5.5)$$

Since  $\{\theta_j\}$  are only well defined on a unit circle, for the SFF expression in Eq. (5.4) to be well defined,  $\tau$  are restricted to take on discrete values [190]  $\tau \in \mathbb{Z}$ . When we rescale the values of  $\{\theta_m\}$  to set the mean level spacing  $\mu$  to unity, this condition reads  $\tau \in \mu$ . On the other hand, for the DOG expression in Eq. (5.5) to be well defined,  $x$  can only take values on a circle and thus  $\chi(x, N)$  has to be a periodic function of  $x$  with period  $2\pi$  ( $2\pi/\mu$  when levels are rescaled to set mean level spacing to 1). Since we performed our analysis by selecting a relatively small subset of levels from the full spectrum, large values of  $\theta_m - \theta_n$  are suppressed. Therefore, the SFF and DOG for circle-valued levels  $\{\theta_m\}$  can be described by the expressions obtained for real-valued levels  $\{E_m\}$  shown in Eqs. (2.18, 2.23, 2.34, 2.31).

### Spin chain with a quasi-periodic local field

Models of quasi-periodic MBL have now been studied in a variety of contexts through the properties of their eigenstates, transport, and operator dynamics [188, 191–200]. We consider the interacting spin chain system with a quasiperiodic magnetic field (QP) [188], defined as:

$$H = J \sum_{i=1}^{L-1} (S_i^x S_{i+1}^x + S_i^y S_{i+1}^y) + J_z \sum_{i=1}^{L-1} S_i^z S_{i+1}^z + W \sum_{i=1}^L \cos(2\pi k i + \phi) S_i^z + J' \sum_{i=1}^{L-2} (S_i^x S_{i+2}^x + S_i^y S_{i+2}^y) \quad (5.6)$$

Here,  $\phi \in [-\pi, \pi)$  is a site-independent phase offset used to generate an ensemble,

$k = (\sqrt{5} - 1)/2$  is an irrational number, and we set  $J = J' = J_z = 1$  for numerical computation. With  $\langle r \rangle$ , the critical disorder is estimated to be around  $W_c \approx 4.3$  [188]. When  $W > W_c$ , the system is in the MBL phase and when  $W < W_c$  it is in the ergodic phase. This model also has spin-rotation  $U(1)$  symmetry, and we consider the spectrum of the zero magnetization sector for numerical computations.

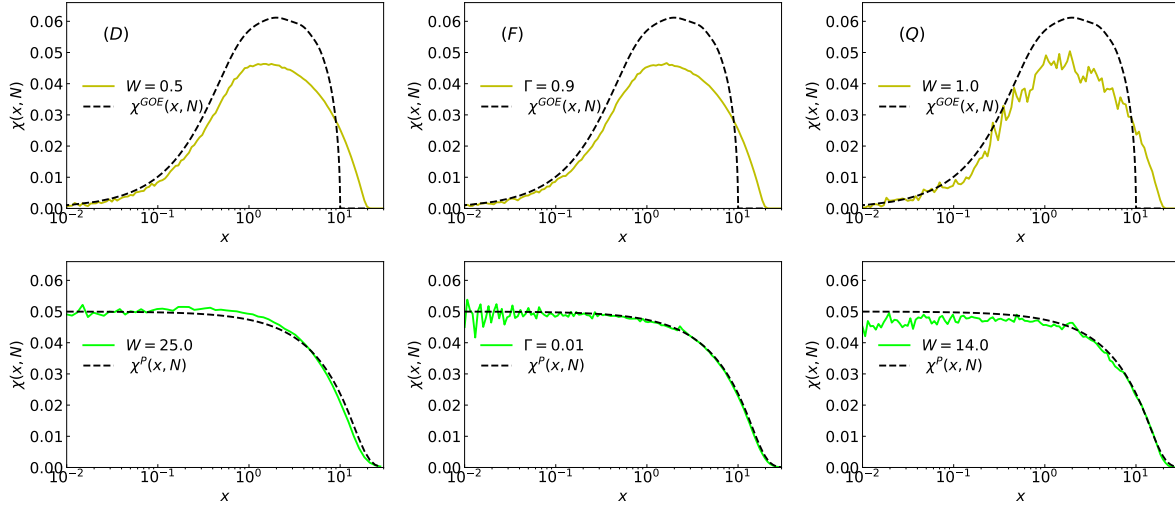


Figure 5.2: DOG [Eq. (2.25)] plots deep in the ergodic phase (top row) and the MBL phase (bottom row) for (from left to right) the disordered spin chain (D), the Floquet spin chain (F) and the quasiperiodic spin chain (Q) defined in Eqs. (5.1, 5.2, 5.6) respectively, compared to the analytical expressions in Eqs. (2.31, 2.34) (dotted lines).  $N = 20$  levels drawn from the middle of the spectrum and rescaled to set mean level spacing at unity, and plotted the numerical data with positive values of gaps with the log scale on x-axis. The system sizes used are (from left to right)  $L = 12, 10, 12$ .

### 5.1.2 Summary of results

The SFF for all three models [Eqs. (5.1, 5.2, 5.6)] is shown in the three columns of Fig. 5.1 from left to right, labeled (D), (F) and (Q) respectively. The SFF for disordered spin chain model [Eq. (5.1)] was studied in [83] where it was verified that the numerical results match the analytical expressions very well. We reproduce the plots in Fig. 5.1 (left column) for completeness. For small values of  $N$ , we see in Fig. 5.1 that the SFF expressions Eqs. (2.23, 2.18) match the data well deep in the MBL and ergodic phases, respectively. The power-law scaling form deep in the MBL phase is also verified in Fig. 5.1. The DOGs for all three models are shown in Fig. 5.2. We see that deep in

the MBL and ergodic phases, the analytical expressions Eqs. (2.34, 2.31) describe the DOG well. Finally, in Fig. 5.3 (bottom row), we show the utility of the density of zero gaps  $N\chi(0, N)$  to estimate the critical disorder strength corresponding to the MBL to ergodic transition using the location where the curves for various sizes of the system cross. Moreover, we see that it agrees well with the same result obtained from the adjacent gap ratio in Fig. 5.3 (top row).

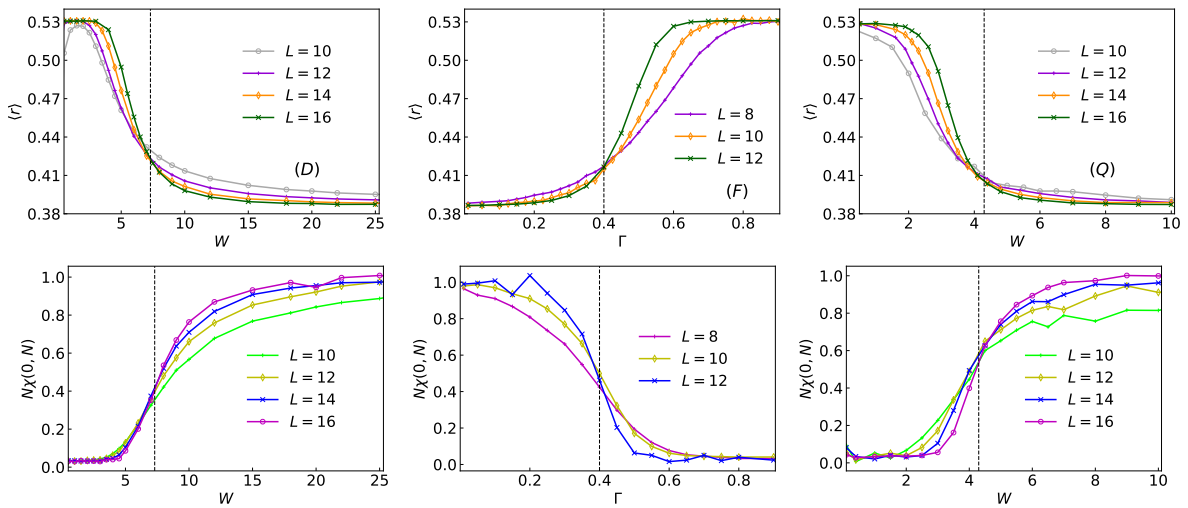


Figure 5.3: (Top row) Plots of the adjacent gap ratio  $\langle r \rangle$  and (Bottom row) rescaled density of zero gaps ( $N\chi(0, N)$ ) across various strengths and sizes of the system used to locate the approximate strength of the critical disorder (dashed line) where the curves for different sizes of the system cross for (from left to right) the disordered spin chain (D), Floquet spin chain (F) and quasi-periodic spin chain (Q) defined in Eqs. (5.1, 5.2, 5.6) respectively. The estimate of the critical disorder computed from  $\langle r \rangle$  and  $N\chi(0, N)$  agrees for all models. The full spectrum used for the plots in the top row and  $N = 20$  levels drawn from the middle of the spectrum used for plots in the bottom row.

For the spin chain with a quasiperiodic local field [Eq. (5.6)], we observe certain finite-size oscillatory features in the SFF, DOG and also in the density of states (DOS) as shown in Fig. 5.4 which are not removed by increasing the number of samples the data are averaged over. However, the amplitude of oscillations reduces with increasing system size as seen in Fig. 5.4. We postulate that these finite-size oscillations have an origin in the quasiperiodic nature of on-site detuning.

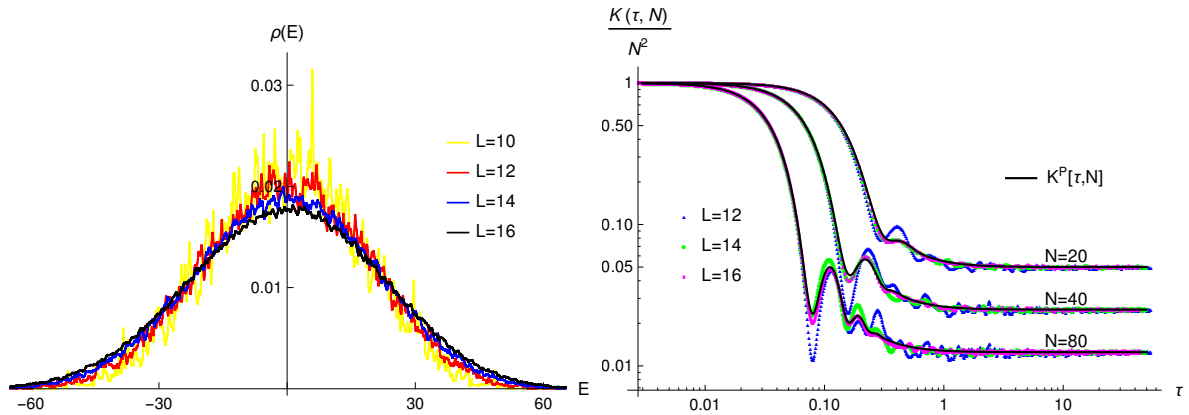


Figure 5.4: Left: Persistent oscillations seen in the density of states of the full  $S_z = 0$  spectrum. Right: SFF [Eq. (2.16)] plotted for levels drawn from the middle of the  $S_z = 0$  sector of the spin chain with quasi-periodic local field [Eq. (5.6)] deep in the MBL phase ( $W = 15$ ). These oscillations remain unchanged with increased disorder averaging, but decrease in amplitude with increase in system size.

## 5.2 On the universality and robustness of spectral signatures in the MBL phase

Spectral signatures in the ergodic phase, for example, the linear ramp in the SFF, are considered to be universal features arising from the underlying level correlations in the system. This means that the ramp survives global deformations of the spectrum, such as unfolding. MBL, on the other hand, is often characterized by the absence of RMT features and level repulsions [201]. It is desirable to identify spectral signatures unique to the MBL phase beyond the absence of ergodic signatures. The results in the preceding sections are an attempt to isolate such signatures. The analytical expressions for the SFF and DOG, especially the power-law scaling form with a fixed exponent shown in Eq. (2.24) was studied in Ref. [83]. This was shown to be a robust feature of the MBL spectra and can be thought of as a universal signature that can help to identify the MBL phase and distinguish it from the ergodic phase. However, a natural question is what the origin of these signatures in the MBL phase is and how robust they are. Since it is known, by the very definition, that uncorrelated Poisson numbers cannot have intrinsic correlations, their spectral signatures must have their origin in global effects.

In this section, we clarify robustness of universal MBL signatures to smooth changes in global density of states using deformations of various kinds to the spectrum and its

probes. First, we study the effects of sharp features in the DOS of Poisson numbers generated as shown in Eq. (2.23) and we study the robustness of the SFF as they are smoothed. We find that key features of the SFF, such as power-law scaling Eq. (2.24) survive such changes. Next, we modify the expression for the SFF formula following the prescription in Ref. [201] and find that while the power-law scaling form survives, the coefficient is renormalized and eventually disappears. Finally, we compute the SFF after unfolding the spectrum, where we find that the power-law scaling form is eliminated. However, we find that it is again recovered if the SFF is computed from a subset of the levels in the unfolded spectrum. We conclude that the power-law scaling form has its origin in the global features of Poisson numbers but not directly from the density of states. They are nevertheless useful to distinguish MBL from ergodic systems in finite system size simulations, especially when probed at energy scales where the latter is dominated by intrinsic level repulsions.

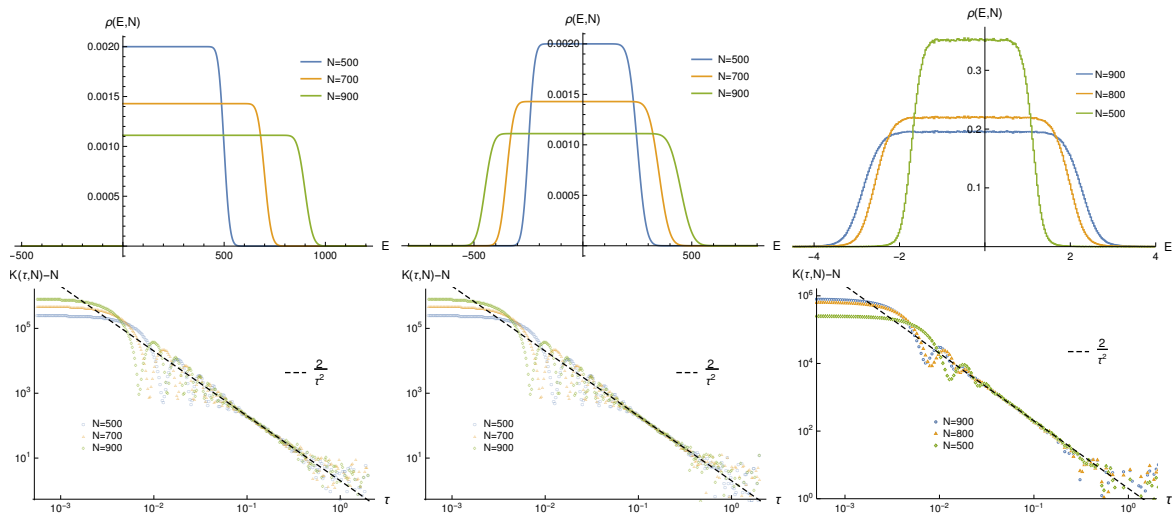


Figure 5.5: DOS (top row) and the reduced SFF (bottom row) for Poisson numbers generated as described in Eq. (2.20) (left column), Poisson numbers generated in Eq. (2.20) with random offset to soften the DOS edges, shown in Eq. (5.10) (middle column) and levels chosen from the disordered Hamiltonian Eq. (5.1) ( $L = 18$ ) deep in the MBL phase ( $W = 25$ ).

### 5.2.1 Deforming the global density of states

Using the probability density in Eq. (2.21), we can easily compute the density of states for Poisson numbers generated explicitly as [83]

$$\rho(E, N) = \frac{1}{N} \sum_{k=1}^N \langle \delta(E - E_k) \rangle = \frac{\Gamma(N, E/\mu)}{\mu N!}, \quad (5.7)$$

where,  $\Gamma(N, x)$  is the incomplete Gamma function defined (for integer  $N$ ) as

$$\Gamma(N, x) = \int_x^\infty dt t^{N-1} e^{-t} = e^{-x} (N-1)! \sum_{k=0}^N \frac{x^k}{k!}. \quad (5.8)$$

Since the energies are chosen to be positive definite, the ensemble-averaged DOS has a sharp edge at  $E = 0$  as shown in the top left column of Fig. 5.5. One might postulate that the power-law scaling form is an artifact of Fourier transforming this sharp edge. However, this is not the case, as easily seen from the formula for the SFF in Eq. (2.16) which only takes into account the differences in levels and would not change if the spectrum were modified to smooth out the sharp edge. For instance, let us shift all Poisson numbers by the same random offset parameter  $E_0$ , drawn from a Gaussian distribution  $p_0(x)$  with mean  $N/2$  and variance  $N$ ,

$$p_0(x) = \frac{1}{\sqrt{2\pi N}} \exp\left(-\frac{(x - N/2)^2}{2N}\right). \quad (5.9)$$

Assuming  $m > n$ , the new joint two-point distribution  $\tilde{P}(E_n, n; E_m, m)$  is

$$\tilde{P}(E_n, n; E_m, m) = \tilde{p}(E_n, n) p(E_m - E_n, m - n), \quad (5.10)$$

where,

$$p(E, k) = \frac{e^{-\frac{E}{\mu}}}{\mu(k-1)!} \left(\frac{E}{\mu}\right)^{k-1}, \quad (5.11)$$

$$\tilde{p}(E, k) = \int_0^\infty dx p(x, k) p_0(E - x). \quad (5.12)$$

The form of the new density of states,  $\tilde{\rho}(E, N)$  can be determined as

$$\tilde{\rho}(E, N) = \int_0^\infty dx \rho(x, N) p_0(E - x) \quad (5.13)$$

where,  $\rho(x, N)$  is the original DOS given in Eq. (5.7). By numerical integration Eq. (5.13), we can see in Fig. 5.5 (top row, middle column) that the DOS is smoothed out. However, as mentioned before, the calculation of the SFF Eq. (2.16) only involves the distribution of energy differences  $E_m - E_n$  and therefore is completely independent of the change in DOS introduced in Eq. (5.10) and leaves both analytical expressions of Eqs. (2.23, 2.24) unchanged (see the bottom row, middle column of Fig. 5.5).

In fact, this was already verified directly in Fig. 5.1, where the plots were generated by selecting levels from the middle of the spectrum. As seen in Fig. 5.5 (top right), the density of states for these levels has no sharp edges, and we clearly see that the power-law scaling is robust. To end this section, we remark that the formula for the connected SFF shown in Eq. (2.17) does have a dependence on DOS. However, the effect of smoothing the DOS as Eq. (5.10) is to enhance (double) the coefficient of the power-law scaling form as

$$K_c(\tau, N) - N = \frac{1}{(\mu\tau)^2} \mapsto \frac{2}{(\mu\tau)^2}. \quad (5.14)$$

See Appendix [C] for more details on this.

### 5.2.2 Filtering the SFF formula

We now modify the expression for SFF Eq. (2.16) using the prescription of Ref. [186] by introducing weights  $\zeta(E)$  associated with the eigenvalue  $E$  to define the filtered SFF expression

$$K_\eta(\tau) = \left\langle \sum_{m,n=1}^{Nr} \zeta(E_m)\zeta(E_n)e^{i\tau(E_m-E_n)} \right\rangle. \quad (5.15)$$

Above,  $\zeta(E)$  is a Gaussian filter function defined as

$$\zeta(E) = \exp\left[\frac{-(E - \bar{E})^2}{2(\Gamma\eta)^2}\right], \quad (5.16)$$

where  $\bar{E}$  and  $\Gamma$  are set to the mean and variance of levels from each disorder realization. In the limit  $\tau \rightarrow \infty$ ,  $K_\eta(\tau)$  saturates to  $Z_\eta$ , given by the expression

$$Z_\eta = \left\langle \sum_{m=1}^{Nr} |\zeta(E_m)|^2 \right\rangle. \quad (5.17)$$

The parameter  $\eta$  controls the width of the filter. As seen in Fig. 5.6, as  $\eta$  is reduced, the filtered SFF preserves the power-law scaling form but renormalizes the coefficient as

$$K_\eta(\tau) - Z_\eta = \frac{2}{(\mu\tau)^2} \mapsto \alpha(\eta) \frac{2}{(\mu\tau)^2}, \quad (5.18)$$

where,  $\alpha(\eta)$  is a function that depends on the filter parameter  $\eta$  but not on the number of levels  $N$  as shown in Fig. 5.6. A spectral signature that does not have its origin in

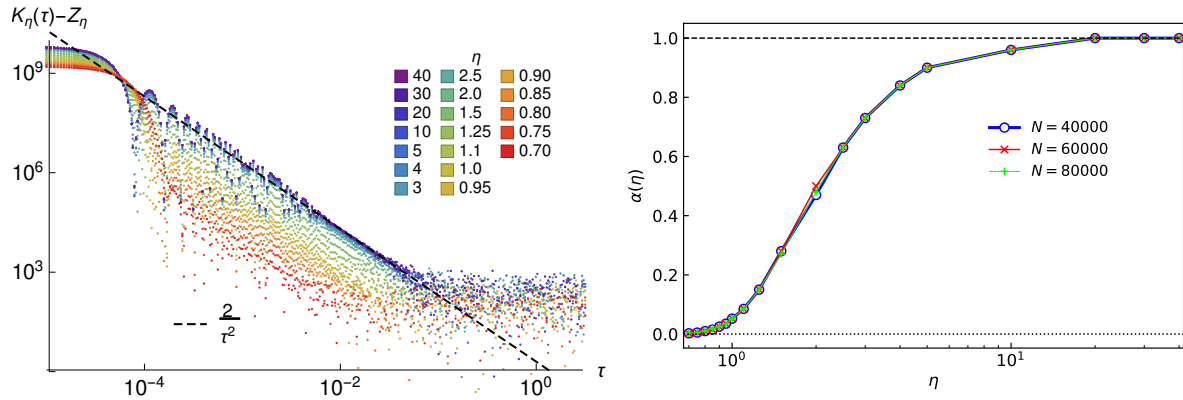


Figure 5.6: Left: The reduced filtered SFF Eq. (5.15) for  $N = 80,000$  Poisson numbers generated as shown in Eq. (2.20) averaged over 50,000 disorder samples. Right: Plot of modified coefficient of the power-law scaling  $\alpha$ , defined in Eq. (5.18) for various  $\eta$ . It is clear that  $\alpha(\eta)$  has no dependence on  $N$ .

global features would be expected to survive in the limit when we take  $N$  to be large and  $\eta$  to be small. This is true for the linear ramp in the ergodic phase [186]. However, since  $\alpha$  has no dependence on the number of levels, in the limit of large  $N$  and small  $\eta$ , it is expected that the power law scaling will vanish. This is consistent with the assertion that the power-law scaling has its origin in global features.

### 5.2.3 Unfolding the spectrum

In this section, we discuss the effect of unfolding the spectrum on the SFF. We begin with Poisson numbers generated as mentioned in Section [2.3.2] whose SFF matches the analytical expression in Eq. (2.23) and exhibits power law scaling Eq. (2.24) at intermediate  $\tau$  values. We now unfold [202–205] the same levels using the usual polynomial method, described in Appendix [A]. Although the density of states was uniform before and after unfolding [84], we see in Fig. 5.7 that the SFF is no longer described by Eq. (2.23) and does not exhibit power law scaling Eq. (2.24). Now, if we compute the SFF with decreasingly smaller fractions of the unfolded spectrum, the analytical form as well as the power law scaling is recovered as shown in Fig. 5.7 (left). To quantify this, we compute the root-mean-square (RMS) deviation of the SFF from the power law scaling form,  $\Sigma$ , defined as

$$\Sigma^2 = \left\langle \left( K(\tau, N) - N - \frac{2}{\tau^2} \right)^2 \right\rangle - \left( \left\langle K(\tau, N) - N - \frac{2}{\tau^2} \right\rangle \right)^2, \quad (5.19)$$

where  $\langle \dots \rangle$  represents the average taken over data points falling in the domain  $\tau \in [\frac{3}{\sqrt{N}}, 0.2]$  where the power law scaling form is expected to be clearest when present. As seen in Fig. 5.7 (right), for  $N/N_R \rightarrow 1$ ,  $\Sigma$  is large, indicating that the SFF deviates significantly from the power-law scaling form. As  $N/N_R \rightarrow 0$ , we find that  $\Sigma$  vanishes, indicating that the power-law scaling form is recovered.

We conclude this section with a few comments. Unlike the linear ramp of the ergodic SFF which is unaffected by unfolding, the power-law scaling form of the SFF in the MBL phase is a global feature. The long-ranged spectral signatures for the MBL phase, such as power-law scaling, arise from the global features of ordered, uncorrelated levels. This is related to the emergence of the Poisson distribution in the distribution of spectral gaps starting with an ensemble of random numbers drawn from any independent identical distribution after ordering (see the supplementary material of Ref. [83] for a discussion on this). In conclusion, we believe that our results suggest that using spectral signatures that have their origin in both intrinsic and global details is more useful in characterizing eigenstate phases as well as integrability (and its breaking) on a finite number of levels as compared to those that are retained by unfolding and similar procedures and depend on intrinsic correlations only. For example, the analysis presented here is quite useful for characterizing the spectral correlations in the middle part of the many-body spectrum

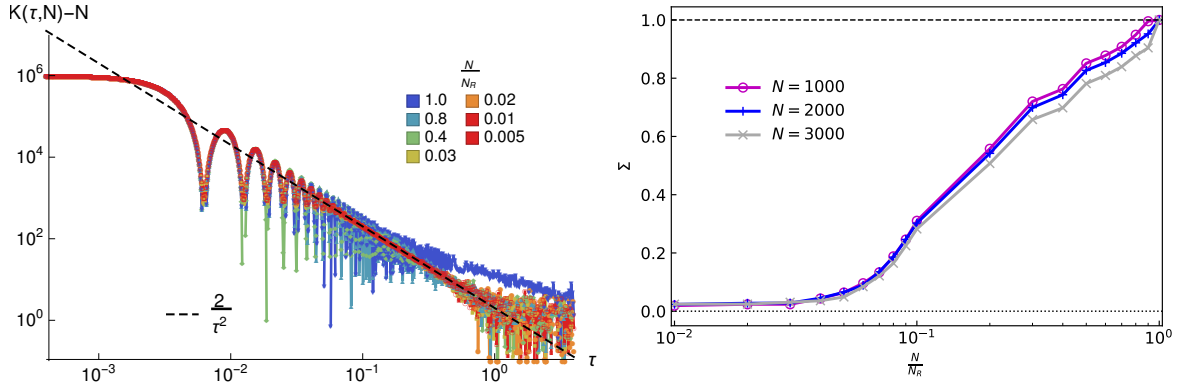


Figure 5.7: Left: Reduced SFF for  $N = 1000$  fixed levels selected from unfolded  $N_R$  Poisson numbers generated as shown in Eq. (2.20) averaged over 400,000 disorder samples. Right: RMS deviation of the SFF  $\Sigma$  from the power law scaling form, defined in Eq. (5.19) calculated with the data points in the window  $\tau \in [\frac{3}{\sqrt{N}}, 0.2]$ . The power-law scaling form is absent when  $\frac{N}{N_R} \sim 1$  and is recovered at the limit  $\frac{N}{N_R} \sim 0$ .

at finite sizes, as conventionally considered in numerical studies of MBL.

## 5.3 Discussion

In this section, we discuss our findings relative to other related works of long-ranged spectral correlations in the MBL phase.

### 5.3.1 The effect of many-body resonances in the MBL phase

In this work, we have used Poisson numbers to derive analytical expressions for the SFF and DOG in the MBL phase, which assumes that the levels have zero intrinsic correlations. While this should be a good description deep in the MBL phase, as we approach the transition, however, many-body resonances will begin to proliferate [206, 207], an effect that we have neglected in our treatment of the SFF. These resonances can lead to weak but nonzero level repulsions in finite-size systems that have been shown to have a nonvanishing value of  $\chi(0, N)$  [208] if the energy resolution is chosen appropriately (and we note that this effect vanishes in the thermodynamic limit). Indeed, these effects are also observable in our finite-size simulations and in the appropriate regimes connects to our results from the previous sections as we now demonstrate.

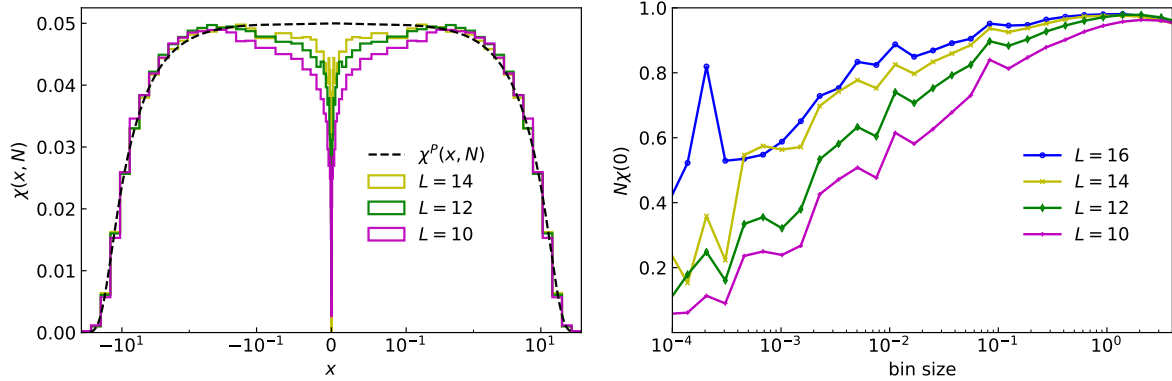


Figure 5.8: Left: DOG [Eq. (2.25)] for the disordered spin chain model Eq. (5.1) in the MBL phase with disorder strength  $W = 15$  computed with  $N = 20$  energy levels drawn from the middle of the spectrum plotted on a log scale to capture the dip at the origin. The DOG approaches the form predicted by Poisson numbers Eq. (2.34) with an increase in system size. Right: Rescaled density of zero gaps ( $N\chi(0, N)$ ) versus binning size. This vanishes for small bin and system size and approaches the value of 1 predicted using Poisson numbers with an increase in bin and system size.

The expression of DOG for Poisson numbers,  $\chi^P(x, N)$  shown in Eq. (2.34) shows a peak for zero-gaps,  $\chi(0, N)$  as shown in Fig. 2.3 which is confirmed in numerical studies of  $\chi(x, N)$  in Section [5.1]. To see the vanishing of  $\chi(0, N)$  predicted in [208], we consider the disordered spin chain model shown in Eq. (5.1). Fig. 5.8 shows that with careful binning on a log-scale,  $\chi(x, N)$  deviates from  $\chi^P(x, N)$  in a range  $\delta_L$  and vanishes in the limit  $x \rightarrow 0$ . With increasing system size, we also see that  $\delta_L$  reduces and the DOG increasingly agrees with Eq. (2.34). If we increase the size of the histogram bins to be larger than  $\delta_L$ , as it was done in Section [5.1], the finite-size vanishing of  $\chi(0, N)$  in the MBL is not observed, as seen in Fig. 5.2 and we find  $N\chi(0, N) \rightarrow 1$  as expected from Eq. (2.34). More details on the robustness of  $\chi(x, N)$  for binning sizes larger than  $\delta_L$  are shown in Appendix [D].

In summary, if we choose a bin size larger than  $\delta_L$ , Eq. (2.34) reproduces the form of  $\chi(x, N)$  accurately. As we increase system size  $L$  and disorder strength, we expect  $\delta_L$  to reduce, and the expression of Eq. (2.34) is increasingly accurate for various binning sizes.

### 5.3.2 Symmetry breaking picture for delocalization

Fig. 2.3 shows the DOG for Poisson numbers and random matrices. It is clear that the DOG distinguishes the two cases very well. While the DOG for random matrices is characterized by a deficit in zero gaps, the Poisson DOG is characterized by a clustering at zero gaps. From its definition in Eq. (2.25),  $\chi(x, N)$  has a reflection symmetry

$$\chi(-x, N) = \chi(x, N). \quad (5.20)$$

The value of spectral gaps  $x^*$  that maximizes  $\chi$  serves as a proxy for level repulsions. From Fig. 2.3 it is clear that for RMT,  $x^* \neq 0$  and for Poisson numbers,  $x^* \rightarrow 0$ . Thus, the  $x \mapsto -x$  symmetry of  $\chi(x, N)$  leaves the value of  $x^*$  invariant in the MBL phase but not in the ergodic phase. This is reminiscent of the symmetry-breaking transition in the Ising model if we make an analogy between  $-\chi(x, N)$  with the Landau free-energy potential of the Ising model and  $x^*$  the location of the potential minima with the magnetic order parameter. This motivates the possibility of tracking the MBL-to-ergodic transition via a symmetry-breaking framework. We remark that a symmetry-breaking framework to describe the ergodic-MBL transition was recently discussed in Ref. [209] where the ergodic phase also corresponded to the symmetry-breaking phase. However, the symmetry they consider is more complex, and it is unclear if and how it is connected to the  $\mathbb{Z}_2$  symmetry of the DOG described above.

# Chapter 6

## Stochastic control of chaos in Kicked Top model

Methods have been developed to control the chaotic dynamics of classical systems using both deterministic [210] and probabilistic [104–106] control protocols. In this chapter, we will focus on the probabilistic control of chaos. The main idea behind these control protocols is to stochastically apply a control map (with probability  $p$ ) to the chaotic map. The chaotic map may possess unstable periodic orbits. The control map is constructed to share the same periodic orbits as the chaotic map but must be stable fixed points. Through the stochastic process of control and chaos, the dynamics get stabilized on the periodic orbit, which serves as a global attractor for a rate  $p_c$  at which control is applied and we have control transition.

### 6.1 Classical Kicked Top model

In this work, we study the Kicked Top model in the chaotic regime under the probabilistic control map and show that the dynamics can be frozen around the unstable fixed point of the chaotic map. To construct models with a competition of chaotic dynamics and control we first choose a generator of the chaotic dynamics, and then identify its unstable fixed points to form a control map that “pushes” the state of the system onto them. As we show below, the the Kicked-Top model introduced by Haake and Kus [211], is a suitable setting to explore this phenomenon. In this model, a spin (or “top”) is periodically driven representing a dynamical system that can manifest classi-

cal, and quantum chaotic motion. It has a single spin degree of freedom and a compact two-dimensional sphere as its classical phase space. An interesting aspect of the dynamics of the Kicked top is that the strength of classical chaos is tunable allowing for an interesting platform to introduce competing perturbations. Importantly, the classical unstable orbits can be identified through an analytic equation that can be straightforwardly solved numerically. This allows for control maps to be accurately constructed, an essential piece to this dynamical model construction.

The classical Kicked Top model is described by the following Hamiltonian,

$$H_{\text{KT}} = \left(\frac{\hbar\alpha}{T}\right)J_y + \left(\frac{\hbar k}{2S}\right)J_z^2 \sum_{n=-\infty}^{\infty} \delta(t - nT). \quad (6.1)$$

In this model,  $\mathbf{J} = (J_x, J_y, J_z)$  represents the components of the angular momentum operator, where  $|\mathbf{J}| = S$  denotes the total spin magnitude. The spin  $\mathbf{J}$  is subjected to periodic external impulses, referred to as "kicks." The parameters  $\alpha$  and  $k$  characterize the strength of the kinetic and kicked terms in the Hamiltonian, respectively. This Hamiltonian can be interpreted as describing the dynamics of a large spin  $\mathbf{J}$  that precesses around the y-axis with an angular frequency  $\alpha/T$ . One of the example of finding such kind of spin precession occurs when it is in the presence of a uniform magnetic field (represented in kinetic term). At regular intervals of time  $T$ , the system experiences a kicks that induce an impulsive rotation around the z-axis with the angle proportional to  $J_z$ , affect the spin's evolution.

For small kicking strength  $k$ , trajectories of motion of kicked top in the phase space  $(\theta, \phi)$  appear regular and with increasing  $k$ , trajectories become random and filled the phase-space. Within random trajectory points, there are some specific points that are the fixed points (stable and unstable) of this map. The stability of the orbit points of the map can be tested by linearizing the map in their vicinity. This model has stable fixed points (Ex. period-1 solutions given in Eq. 5.3) for kicking strength  $k < \sqrt{2}\pi$  and become unstable for  $k > \sqrt{2}\pi$ . For strong enough kicking strengths  $k > \sqrt{2}\pi$  [211], the Kicked Top Hamiltonian defined in Eq. (6.1) exhibits fully chaotic dynamics (for  $\alpha = \pi/2$ ). This model can be made quantum mechanical by promoting the classical spin variables to quantum spin operators  $(\hat{J}_x, \hat{J}_y, \hat{J}_z)$  of size  $S$  that satisfy the SU(2) algebra  $[\hat{J}_i, \hat{J}_j] = i\epsilon_{ijk}\hat{J}_k$ .

### 6.1.1 Chaos-Control Dynamics

We now construct the chaotic part of the dynamics, which is a review of the classical equations of motion of the Kicked top. In the following, we apply Newtonian dynamics (i.e. the chaotic map) with probability  $1 - p$  and the control map with probability  $p$ , which introduces a model that allows for the competition between chaos and control in the dynamics of the rotor.

#### Newtonian dynamics

In the classical limit of the model  $S \rightarrow \infty$ , the chaotic evolution is driven by the classical discrete-time evolution on the vector  $\mathbf{r} \equiv \mathbf{J}/S = (x, y, z)$ , which yields [211],

$$\begin{aligned} x_{n+1} &= z_n \cos(kx_n) + y_n \sin(kx_n), \\ y_{n+1} &= -z_n \sin(kx_n) + y_n \cos(kx_n), \\ z_{n+1} &= -x_n. \end{aligned} \tag{6.2}$$

The equation above represents an iterative map that takes the position coordinates  $\mathbf{r}_n = (x_n, y_n, z_n)$  at time step  $n$  and provides the updated position coordinates  $\mathbf{r}_{n+1} = (x_{n+1}, y_{n+1}, z_{n+1})$  after a discrete time interval  $T$ . For this parameterization, we have chaotic dynamics only in the range  $k > \sqrt{2}\pi$ . For  $k < \sqrt{2}\pi$  the phase space of the model is mixed but fixed points are the stable fixed points. We note that this tunability with  $k$  allows an interesting control over the strength of chaos that allows the control dynamics (described below) to become more dominant.

#### Classical Control Map

In order to construct the control map, we have to first identify unstable fixed points of the dynamics in Eq. (6.2). For simplicity of the construction, in this work, we focus on unstable orbits with period-1. From the condition for a fixed point  $\mathbf{r}' = \mathbf{r}$ , it is known that the period-1 unstable orbits are given by [211]

$$x_0^2 = \frac{\sin^2(kx_0/2)}{1 + \sin^2(kx_0/2)} \tag{6.3}$$

together with  $z_0 = -x_0$  and the normalization  $x_0^2 + y_0^2 + z_0^2 = 1$  implies that  $y_0 = \sqrt{1 - 2x_0^2}$ , allowing the vector at the fixed point  $\mathbf{r}_0 \equiv (x_0, y_0, z_0)$  to be determined solely

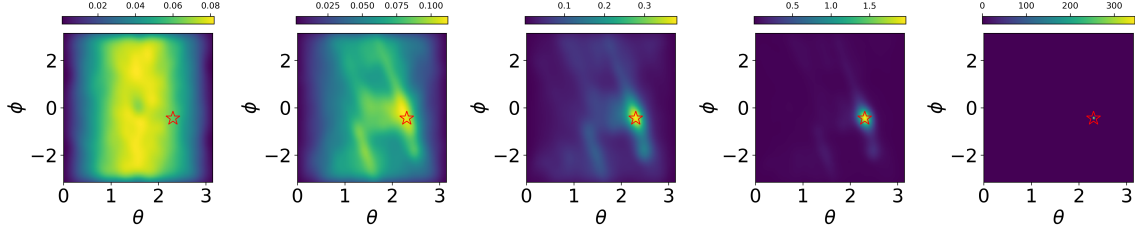


Figure 6.1: Density plots of trajectories of the Kicked Top model in the  $\theta - \phi$  phase plane with control map [Eq. (6.5)] with probability  $p = 0.0, 0.1, 0.2, 0.3, 0.5,$  and  $0.7$  (left to right). Parameters  $k = 6, a = 0.5$  are taken for the numerical computation, and data is generated over 1000 time steps.

through the solution of Eq. (6.3).

By numerically solving Eq. (6.3) we obtain the fixed point value  $\mathbf{r}_0$  as a function of  $k$ . We then apply the control map with probability  $p$  by rotating the vector  $\mathbf{r} = (x, y, z)$  on the sphere towards the unstable fixed point  $\mathbf{r}_0$ . We do this rotation on the sphere through spherical coordinates  $\mathbf{r} = (\cos \phi \sin \theta, \sin \phi \sin \theta, \cos \theta)$  allowing us to parameterize the state of the Kicked top through  $(\theta, \phi)$  where  $\theta \in (0, \pi)$  and  $\phi \in (0, 2\pi)$  through

$$\begin{aligned}\theta &= \cos^{-1}(z/\sqrt{x^2 + y^2 + z^2}) \\ \phi &= \tan^{-1}(y/x).\end{aligned}\tag{6.4}$$

This control map tries to bring the dynamics at the unstable fixed point  $\mathbf{r}_0$  that is now labeled by  $(\theta_0, \phi_0)$ . The unstable fixed point  $\mathbf{r}_0$  corresponding to solutions to Eq. (6.3) is numerically determined by solving a transcendental equation. The control map is then defined as follows: if the vector points within the half of the unit sphere with  $X > 0$  (where the unstable fixed point resides) we then “push” the vector towards the fixed point with strength  $a$ , through the mapping  $\mathbf{r} \rightarrow \mathbf{r}'$  defined by

$$\begin{aligned}\theta' &= (1 - a)\theta_0 + a\theta, \\ \phi' &= (1 - a)\phi_0 + a\phi.\end{aligned}\tag{6.5}$$

We note that we have chosen for each angle to be pushed the same, namely  $a_\theta = a_\phi = a$  for further computation.

### 6.1.2 Observables

In the controlled phase, the dynamics of the system are regularized onto the desired unstable periodic orbits, and in the uncontrolled phase, the control map fails to stabilize the chaotic motion onto the unstable periodic orbits and it remains chaotic.

Classically, we consider two key physical quantities that can capture the nature of the control phase transition. The first is the distance of the spin from its fixed point value, namely, we define the square deviation as

$$\begin{aligned}\delta r^2(t) &\equiv |\mathbf{r}(t) - \mathbf{r}_0|^2, \\ O^2 &= \delta r^2(t \rightarrow \infty).\end{aligned}\tag{6.6}$$

If  $\delta r^2(t)$  remains finite in the long-time limit, we will never reach the fixed point, whereas if  $\delta r^2(t)$  goes to zero then we know the dynamics is exponentially close to the unstable fixed point  $\mathbf{r}_0$ . Therefore,  $O^2$  is a measure of the ‘‘activation’’ away from the fixed point value and acts as an order parameter for the transition.

To probe the nature and strength of chaos we compute the Lyapunov exponent of the dynamics. If the dynamics is chaotic then two initial trajectories, denoted  $\mathbf{r}_A$  and  $\mathbf{r}_B$ , that is started from an infinitesimally small separation  $|\mathbf{r}_A(0) - \mathbf{r}_B(0)| = d_0 \ll 1$  grows exponentially with time with a positive (leading) Lyapunov exponent. In contrast, in the control phase, we expect these two initial states to both get pushed to the same fixed point value  $\mathbf{r}_0$ , thus the Lyapunov exponent should be negative. In either phase of the model, we expect that  $|\mathbf{r}_A(t) - \mathbf{r}_B(t)| \sim e^{\lambda t}$  and  $\lambda$  is the Lyapunov exponent of the combined Newtonian dynamics and control map. To compute the Lyapunov exponent, we start from two random trajectories that are initially separated by an amount  $d_0 = 10^{-7}$  and the Lyapunov exponent [212]  $\lambda$  is determined from

$$\lambda = \frac{1}{n\tau} \left\langle \sum_{i=1}^n \log \frac{d_i}{d_0} \right\rangle.\tag{6.7}$$

$\langle \dots \rangle$  represent the averaging over the different initial conditions.  $d_i = |\mathbf{r}_A(t) - \mathbf{r}_B(t)|$  is the separation between trajectories A and B at time  $\tau$  that are evolved from the initial separation  $d_0$ . In each step, we reset one trajectory towards another after the time  $\tau$  to keep the separation equal to the initial separation. For computation, we fixed  $\tau = 10$  and  $n$  is taken to be sufficiently large that the  $\lambda$  converge to a value.

## 6.2 Classical Control Transition

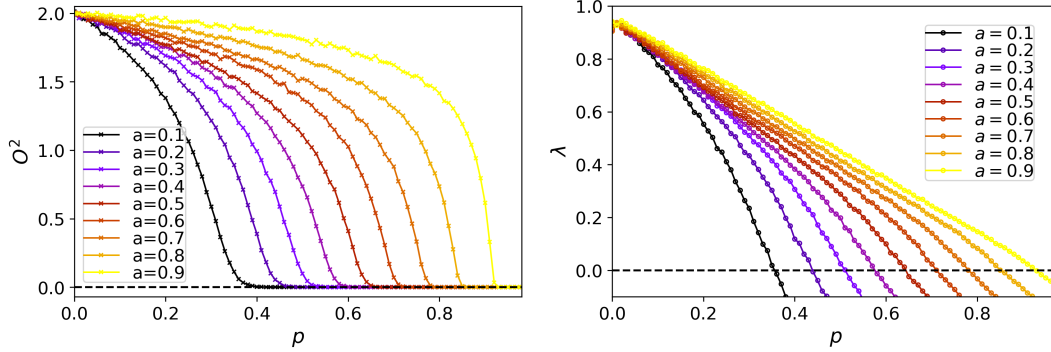


Figure 6.2: (Left) The plot of  $O^2$  as defined in Eq. (6.6) is the measure of the steady-state value of square deviation from the fixed point  $t \rightarrow \infty$  and (Right) Lyapunov exponent  $\lambda$  as defined in Eq. (6.7) with respect to control probability  $p$  for various value of  $a$ . For numerical computation, kicking strength  $k = 6$  and control map parameter  $a = 0.5$ .

As shown in Fig. 6.1, random trajectories of chaotic Kicked top motion filled the whole  $\theta - \phi$  plane and with increasing control map probability  $p$ , dynamics tend to regularize around the unstable fixed point. For sufficient enough  $p$ , the motion gets frozen to that point. In this section, we discuss the classical control transition using square deviation  $O^2$  [Eq. (6.6)] and Lyapunov exponent  $\lambda$  [Eq. (6.7)] observable. These quantities are sampled over many realizations of initial conditions. Using these measures we estimate the critical control probability  $p_c$  at which controlled-uncontrolled transition takes place. For that, we consider the chaotic Kicked top model with kicking strength  $k = 6$ , and apply the stochastic control map with probability  $p$ .  $O^2$  is the steady state value of the square deviation from the fixed point. In Fig. 6.2 (left),  $O^2$  is finite for a small  $p$  and at around a critical  $p$  value,  $O^2$  approaches to zero (with 0.01 tolerance). We identify a critical point  $p_c$  of the controlled-uncontrolled phase transition corresponding to a control map parameter  $a$ . Dynamics undergoes the controlled-uncontrolled phase transition with finite  $p_c \in (0, 1)$  when  $\vec{r}_0$  in the control map [Eq. (6.5)] is the fixed point of the chaotic map. Otherwise, it fails to regularize the dynamics around this point for any control probability  $p < 1$  and the system will remain chaotic. This shows that we need to have knowledge of the unstable fixed points of the chaotic model to control the dynamics. The estimated  $p_c$  data is plotted in Fig. 6.3 with respect to various values of control map parameter  $a$ .

Lyapunov exponent  $\lambda$  data in Fig. 6.2 (right) of this stroboscopic chaos-control map also shows that  $\lambda$  is positive for small control probability and it decreases with increasing  $p$  and changes sign at a control probability  $p$  that is approximately same as estimated controlled-uncontrolled critical point  $p_c$  computed from the  $O^2$  data.

### 6.2.1 Phase Diagram

In the above section, we have described how we estimate the critical point  $p_c$  of the controlled-uncontrolled transition using the quantity  $O^2$ . In Fig. 6.2 (left), it is shown how  $O^2$  changes with control probability  $p$  for a fixed value of control parameter  $a$  that is applied on chaotic Kicked top model ( $k = 6$ ). For a complete picture, we generate the full phase diagram in the  $a - p$  plane and plot  $O^2$  in a color bar for  $k = 6$  in Fig. 6.3 (Left). In this phase diagram, controlled and uncontrolled phases are in two distinguished regions and separated with the lines of critical points  $p_c$  ( $O^2 = 0$ ) and  $p_c$  ( $\lambda = 0$ ). In Fig. 6.3 (Right) we present the phase diagram of  $O^2$  in the  $k - p$  plane for

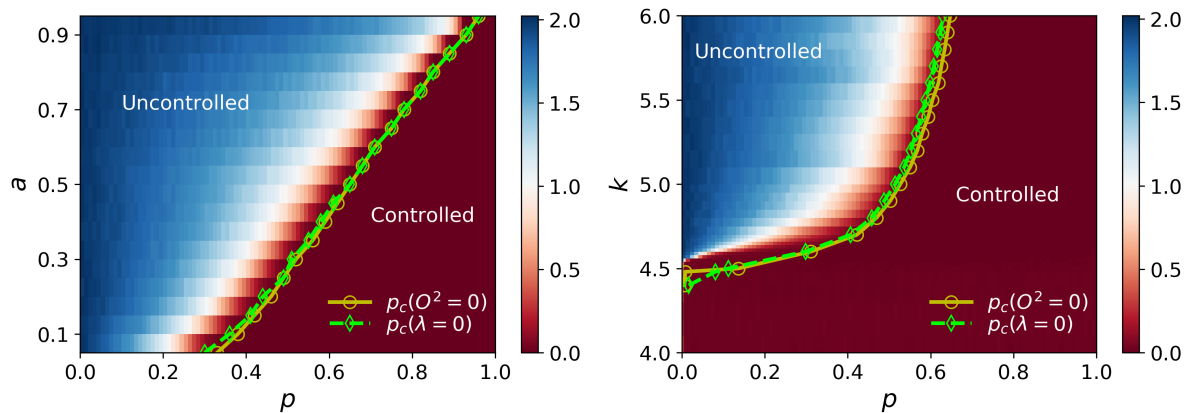


Figure 6.3: (Left) Uncontrolled-controlled phase diagram in the  $a - p$  plane with the distance measure  $O^2$  [Eq. (6.6)] (color bar) of the chaotic Kicked top model ( $k = 6$ ) with control map. (Right) Uncontrolled-controlled phase diagram in the  $k - p$  plane with the distance measure  $O^2$  of the Kicked top model with control map ( $a = 0.5$ ). Uncontrolled and controlled phases are separated by estimated critical points  $p_c(O^2 = 0)$  and  $p_c(\lambda = 0)$  that are computed from the  $O^2$  and  $\lambda$  data respectively.

fixed control parameter  $a = 0.5$ . In this case, also, we get two regions, controlled and uncontrolled. For  $k < 4.5$ , the dynamics is always controlled with infinitesimally small control probability  $p$  as the nature of the fixed point is stable. For  $k > 4.5$ , as the nature

of fixed point changes one requires finite  $p$  to regularize the dynamics. Hence we have finite  $p_c (O^2 = 0)$  and  $p_c (\lambda = 0)$ .

# Conclusion and outlook

This thesis broadly covers the work on the study of spectral signatures of chaos, integrability and MBL in many body closed and open quantum systems in first four chapters. In Chapter [2] we introduced all the spectral statistics diagnostic that is used to characterize chaos and integrability in quantum systems. We discussed in great detail long-range spectral correlations: Spectral form factor and density of all gaps for GOE random matrix theory and independent random numbers related to chaos and integrability/MBL phase consecutively. We obtained analytical expressions of these quantities verified with its numerical study.

In Chapter [3] we present the results of spectral phase transition in dissipative Dicke model: Integrability to chaos cross over around critical point of symmetry breaking dissipative phase transition that is reported in Ref. [213]. We used the tools of spectral statistics of non-hermitian random matrix theory to diagnose chaos. While our results unambiguously reveal a tight connection between dissipative quantum phase transition driven by integrability-breaking term and spectral phase transition of the Liouvillian, whether they happen simultaneously at  $\lambda = \lambda^*$  has yet to be scrutinized. The approach we developed here can be straightforwardly adapted to other dissipative quantum dynamics.

Universal spectral features of a spatially extended system (Tavis-Cummings lattice model) are discussed in Chapter [4] and a corresponding minimal impurity model is introduced that can capture these features of the corresponding model with a much smaller Hilbert space. With exact diagonalization, we study the spectral statistics of these models. We provide an estimated relation between the integrability breaking parameter of lattice and impurity models. We also discuss the semiclassical limit of the impurity model and show the Poincare sections that show very rich properties at different energy scales.

In Chapter [5], we have studied long-range spectral probes and their use in characterizing many-body localization and ergodic phases and the transition between them. We obtain analytical forms for these probes and numerically verify their validity and utility using a variety of spin chain models to find excellent agreement. We also discussed the nature of the universality and robustness of these spectral signatures and briefly commented on related work. Recent demonstration of large-scale Hamiltonians involving a large number of qubits (or spin sites) in quantum devices is indeed a promising avenue to potentially explore these quantities. The robust nature of these quantities that we demonstrated in this work indicates that such quantities can potentially be observed despite experimental imperfections that are often inevitable in large-scale systems. In future work, it would be interesting to further explore the utility of long-range spectral probes to shed light on the nature of the transition between many-body localization and ergodic phases, as well as investigate whether the symmetry-breaking picture of Section [5.3.2] can help produce an effective theory for the transition.

Chapter [6] is based on the study of stochastic control in chaotic classical systems, where we used the Kicked Top as a model for chaos and applied a control map. Through numerical analysis, we computed the square deviation from the fixed point and the Lyapunov exponent, identifying a critical point  $p_c$ , at which the dynamics become fully controlled. We present a phase diagram within the chaos-control parameter space, illustrating the distinct regimes of controlled and uncontrolled phases. Recent work [107,214] showed that on stochastic control protocol of a classical chaotic system, dubbed probabilistic control of chaos possesses several features of the MITP once feedback is included in the quantum dynamics. This approach allowed us to view the classical and quantum control endeavors within a common lens thereby enabling us to import techniques developed in classical dynamical systems to the quantum control field. With the extension of our work to construct quantum control protocols, the Quantum Kicked Top model may shed light on similarities and differences in quantum entanglement and classical control transition. The Quantum Kicked Top model has a well-defined semi-classical limit, which enables to combined quantum chaotic and control dynamics to tend to the classical control dynamics in the  $J \rightarrow \infty$  limit. It would be interesting to examine how the results obtained in the semi-classical limits of the quantum model make sense with the classical results that we presented in the Chapter [6]. This work may further help to develop a general framework of quantum adaptive dynamics where measurements and feedback can be employed to stabilize a desired quantum many-body phase.

# Appendix A

## Unfolding the spectrum

To eliminate the system-specific features of the spectrum, to extract its universal features, and to compare them with random matrix theory predictions, it is customary to perform a so-called unfolding procedure of the spectrum [16, 202, 215–220]. It proceeds by transforming the original spectrum such as to ensure a uniform local density of states in the resulting spectrum. In practice, we use the following procedure:

1. First, we compute the cumulative density of the ordered spectrum,  $I(E) = \sum_n \Theta(E - E_n)$  where  $\Theta(x)$  is the Heaviside step function.
2.  $I(E)$  is then fitted to a smooth polynomial function  $\tilde{I}(E)$ .
3. Finally, the unfolded spectrum is obtained as,  $\tilde{E}_n \equiv \tilde{I}(E_n)$ .

We display in Fig. (A.1) the density of states of the original spectrum of Tavis-Cummings Lattice model [Eq. (4.1)] and its corresponding unfolded spectrum for two different values of  $J/\lambda$ . We have used a 12<sup>th</sup>-order polynomial in the unfolding procedure. Clearly, the resulting density of states is almost constant. The level-spacing distribution is computed from the unfolded spectrum as  $p(s) = \sum_n \delta(s - (\tilde{E}_{n+1} - \tilde{E}_n))$ . After unfolding, the mean level spacing is unity by construction,  $\langle s \rangle = \int_0^\infty ds s p(s) = 1$ , and the higher moments are expected to display universal features depending on the integrable or chaotic nature of the dynamics.

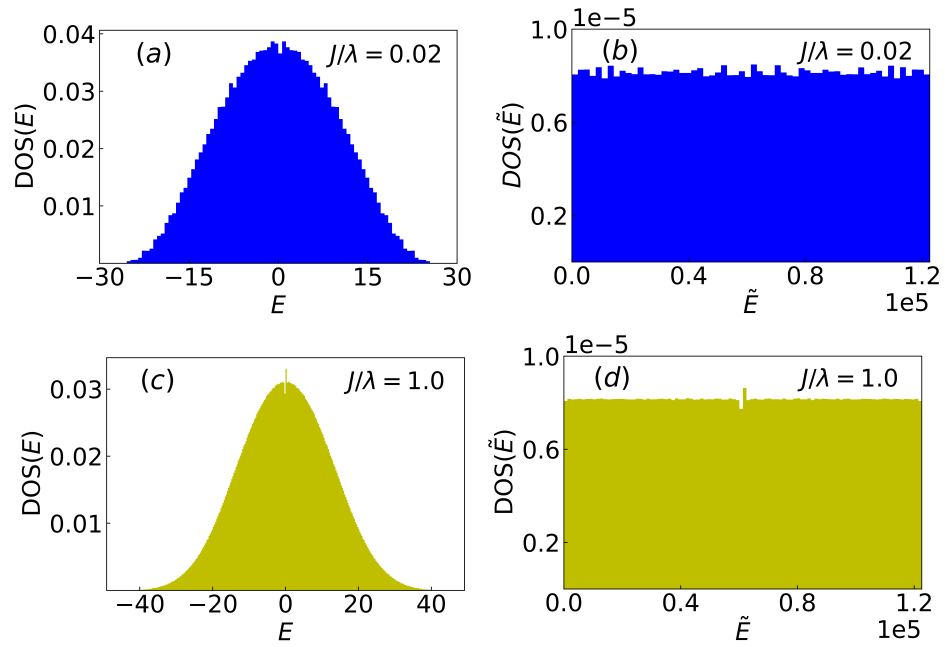


Figure A.1: Density of states (DOS) of the Tavis-Cummings Lattice [Eq. (4.1) in the main text]. (Left panel) Before unfolding. (Right panel) After unfolding. Spectra are computed in the reflection-symmetric sector with  $L = 3$ ,  $S = 8$ ,  $N_{\text{ex}} = 36$ , and  $\lambda = 1.0$  for (a, b) weak hopping  $J/\lambda = 0.02$ , and (c, d) strong hopping  $J/\lambda = 1.0$

# Appendix B

## Mean-field relation between lattice and impurity spectral form factors

In this Appendix, we use a mean-field approach to motivate the impurity model presented in the Chapter [4]. The mean-field approximation is a standard approach to computing thermodynamics but, here, we perform it in the setting of computing the spectral form factor (SFF). We work in the context of the Tavis-Cummings Hamiltonian on a “mean-field lattice” with all-to-all couplings between the  $L$  sites, where  $L$  is large,

$$H = \sum_{i=1}^L h_i - \frac{J}{L} \sum_{i,j=1}^L a_i^\dagger a_j, \quad (\text{B.1})$$

$$h_i = \omega_c a_i^\dagger a_i + \omega_s S_i^z + \frac{\lambda}{\sqrt{S}} \left( a_i^\dagger S_i^- + a_i S_i^+ \right). \quad (\text{B.2})$$

We have scaled the hopping term by  $1/L$ , which is the standard convention consistent with a non-trivial thermodynamic limit. The above Hamiltonian is  $U(1)$ -symmetric which corresponds to the conservation law  $[H, N] = 0$  with  $N = \sum_{i=1}^L n_i$  where  $n_i := a_i^\dagger a_i + S_i^z + \frac{S}{2}$ . Additionally, the Hamiltonian is symmetric under permutations of the sites. This extra symmetry, an artifact of the all-to-all geometry, introduces a subtlety in that the SFF which is relevant for diagnosing quantum chaotic features should in principle be computed in a given sector of the permutation group. A proper treatment of this permutation symmetry is technically challenging and we postpone this computation to future work. Here below we adopt the following strategy:

- We first present a detailed computation that avoids this subtlety by explicitly

breaking the permutation symmetry, therefore computing the mean-field SFF from the untruncated spectrum (yet properly accounting for the  $U(1)$  symmetry). This will yield a simple relation between the lattice and impurity SFFs, see Eq. (B.19).

- Secondly, we present a speculative discussion on how to modify the results of the former computation to account for the permutation symmetry group and we speculate the simple relation [ Eq. (B.22)] between the lattice and impurity SFFs.

**Explicitly breaking permutation symmetry.** Let us first avoid the technicalities related to the permutation group by explicitly breaking this extra symmetry. This can be done by adding disorder with random onsite energy shifts:  $h_i \rightarrow h_i + \delta_i (a_i^\dagger a_i + S_i^z)$  where  $\delta_i$  is random-valued. We shall later take  $\delta_i \rightarrow 0$ .

Working in the sector with  $N = L\rho$  particles, where  $\rho$  is the particle density, we define the corresponding SFF as

$$K_L^\rho(t) := \langle |\tilde{Z}_L(t, \rho)|^2 \rangle, \quad t \geq 0, \quad (\text{B.3})$$

where  $\langle \dots \rangle$  correspond to disorder averaging and  $\tilde{Z}_L(t, \rho)$  is the imaginary-temperature partition function of the lattice model in the  $N = L\rho$  particle sector and for a given realization of the disorder. It is defined as,

$$\tilde{Z}_L(t, \rho) := \text{Tr} \left[^{-Ht} \delta(L\rho - N) \right], \quad (\text{B.4})$$

where  $\text{Tr}$  is the trace over the full lattice Hilbert space and the delta function implements the partial trace on those states with exactly  $N = L\rho$  particles. It can be expressed in terms of an imaginary-temperature grand-canonical partition function via

$$\tilde{Z}_L(t, \rho) = \int_{-\infty}^{+\infty} \frac{\nu^{-L\rho\nu}}{2\pi} Z_L(t, \nu), \quad (\text{B.5})$$

where  $\nu$  plays the role of a chemical potential and the grand-canonical lattice partition function is defined as

$$Z_L(t, \nu) := \text{Tr} \left[ -[H - \frac{\nu}{t} N] t \right]. \quad (\text{B.6})$$

We now relate the partition function of the lattice to that of impurity by employing

a standard Hubbard-Stratonovich decoupling of the hopping term in the Hamiltonian, and a subsequent saddle-point approximation. The latter is sometimes dubbed the strong-coupling random phase approximation (RPA) in the Bose-Einstein condensation literature. The saddle-point approximation will become exact in  $L \rightarrow \infty$  limit.

Introducing complex Hubbard-Stratonovich fields  $\Phi(\tau)$  and  $\Phi^*(\tau)$  for  $\tau \in [0, t]$ ,  $Z_L(t, \nu)$  can be rewritten as

$$\begin{aligned} Z_L(t, \nu) &= \int_{\Phi(t)=\Phi(0)} \mathcal{D}[\Phi, \Phi^*]^{JL \int_0^t \tau \Phi^*(\tau) \Phi(\tau)} \\ &\quad \times \text{Tr} \left[ \overleftarrow{\mathcal{T}}^{-\int_0^t \tau \sum_{i=1}^L [h_i - \frac{\nu}{i} n_i + J(\Phi^*(\tau) a_i + a_i^\dagger \Phi(\tau))]} \right] \\ &= \int_{\Phi(t)=\Phi(0)} \mathcal{D}[\Phi, \Phi^*]^{JL \int_0^t \tau \Phi^*(\tau) \Phi(\tau)} \prod_{i=1}^L \mathfrak{z}_i(t, \nu; [\Phi, \Phi^*]), \end{aligned} \quad (\text{B.7})$$

where  $\mathcal{D}[\Phi, \Phi^*]$  is the functional integral measure over complex functions on  $[0, t]$ .  $\overleftarrow{\mathcal{T}}$  is the time-ordering operator.  $\mathfrak{z}_i$  is the partition function of a local impurity model, namely the single site  $i$  in the presence of auxiliary Hubbard-Stratonovich fields which act as external drives. It reads

$$\mathfrak{z}_i(t, \nu, [\Phi, \Phi^*]) := \text{tr} \left[ \overleftarrow{\mathcal{T}}^{-\int_0^t \tau [h_i - \frac{\nu}{i} n + J(\Phi^*(\tau) a + a^\dagger \Phi(\tau))]} \right]. \quad (\text{B.8})$$

where  $\text{tr}$  is the trace in the local Hilbert space at site  $i$ . Sending the random onsite energy shifts to zero,  $\delta_i \rightarrow 0$ , we now get  $\mathfrak{z}_i \rightarrow \mathfrak{z}$  for all sites with

$$\mathfrak{z}(t, \nu, [\Phi, \Phi^*]) := \text{tr} \left[ \overleftarrow{\mathcal{T}}^{-\int_0^t \tau [h - \frac{\nu}{i} n + J(\Phi^*(\tau) a + a^\dagger \Phi(\tau))]} \right]. \quad (\text{B.9})$$

We have

$$Z_L(t, \nu) = \int_{\Phi(t)=\Phi(0)} \mathcal{D}[\Phi, \Phi^*]^{L [J \int_0^t \tau \Phi^*(\tau) \Phi(\tau) - \ln \mathfrak{z}(t, \nu, [\Phi, \Phi^*])]} \quad (\text{B.10})$$

We now estimate the above path integral by a saddle-point approximation, *i.e.* by extremizing the action over  $\Phi(\tau)$ , which becomes exact in  $L \rightarrow \infty$  limit. Restricting to

time-independent solutions  $\bar{\Phi}$  and  $\bar{\Phi}^*$ , the latter are governed by self-consistent equations

$$\bar{\Phi} = \frac{\text{tr} [a - h_{\text{imp}}(t, \nu, \bar{\Phi}, \bar{\Phi}^*) t]}{\mathfrak{z}(t, \nu, \bar{\Phi}, \bar{\Phi}^*)}, \quad \bar{\Phi}^* = \frac{\text{tr} [a^\dagger - h_{\text{imp}}(t, \nu, \bar{\Phi}, \bar{\Phi}^*) t]}{\mathfrak{z}(t, \nu, \bar{\Phi}, \bar{\Phi}^*)}, \quad (\text{B.11})$$

with the impurity partition function

$$\mathfrak{z}(t, \nu, \bar{\Phi}, \bar{\Phi}^*) = \text{tr} \left[ -h_{\text{imp}}(t, \nu, \bar{\Phi}, \bar{\Phi}^*) t \right], \quad (\text{B.12})$$

and where we have introduced the impurity Hamiltonian

$$h_{\text{imp}}(t, \nu, \bar{\Phi}, \bar{\Phi}^*) := h - \frac{\nu}{t} n + J (\bar{\Phi}^* a + a^\dagger \bar{\Phi}). \quad (\text{B.13})$$

We can now express the lattice partition function in terms of the impurity partition function as

$$Z_L(t, \nu) \stackrel{L \rightarrow \infty}{\approx} e^{L J \bar{\Phi}^* \bar{\Phi} t} [\mathfrak{z}(t, \nu, \bar{\Phi}, \bar{\Phi}^*)]^L. \quad (\text{B.14})$$

Using Eq. (B.14) in Eq. (B.5), and evaluating  $\nu$  integral by means of another saddle-point approximation, we obtain

$$\tilde{Z}_L(t, \rho) \stackrel{L \rightarrow \infty}{\approx} e^{-L \rho \bar{\nu} + J L \bar{\Phi}^* \bar{\Phi} t} [\mathfrak{z}(t, \bar{\nu}, \bar{\Phi}, \bar{\Phi}^*)]^L, \quad (\text{B.15})$$

where the saddle-point value of the chemical potential  $\bar{\nu}$  is governed by the equation

$$\rho = \frac{\text{tr} \left[ n e^{-it \left[ h - \frac{\bar{\nu}}{t} n + J (\bar{\Phi}^* a + a^\dagger \bar{\Phi}) \right]} \right]}{\mathfrak{z}(t, \bar{\nu}, \bar{\Phi}, \bar{\Phi}^*)}. \quad (\text{B.16})$$

The SFF of the lattice model can now be expressed in terms of that of the impurity model as,

$$K_L^\rho(t) \stackrel{L \rightarrow \infty}{\approx} |e^{-i \rho \bar{\nu} + i J \bar{\Phi}^* \bar{\Phi} t}|^2 k(t)^L, \quad (\text{B.17})$$

where  $k(t)$  is the impurity SFF, defined as

$$k(t) := |\mathfrak{z}(t, \bar{\nu}, \bar{\Phi}, \bar{\Phi}^*)|^2, \quad (\text{B.18})$$

and  $\bar{\Phi}$ ,  $\bar{\Phi}^*$  and  $\bar{\nu}$  are determined from the saddle-point equations Eqs. (B.11, B.16). Note that the hermiticity of the impurity Hamiltonian at the saddle point requires  $\bar{\nu}$  to be real and  $\bar{\Phi}$  and  $\bar{\Phi}^*$  to be complex conjugate of each other. Under those assumptions, we obtain

$$K_L^\rho(t) \stackrel{L \rightarrow \infty}{\approx} k(t)^L, \quad (\text{B.19})$$

where  $K_L^\rho(t)$  is the SFF of the all-to-all lattice model defined in Eq. (B.1) and  $k(t)$  is the one of the impurity model defined in Eq. (B.13). The above equality has to be understood as a mean-field factorization of the lattice SFF into a product of those of the local impurity sites. This result is naturally consistent with the general expectation that a mean-field approach formally decouples the lattice partition function in terms of a product of local partition functions. Eq. (B.19) is trivially obeyed at  $t \rightarrow \infty$  and at  $t = 0$ . Indeed, in the former case, the SFFs simply reduce to their respective Hilbert space dimensions, and they reduce to their square in the latter case.

**Speculation in the totally-symmetric sector.** Computing the lattice SFF constrained to the totally-symmetric sector of the permutation group relies on estimating the partition function

$$\tilde{Z}_L(t, \rho) := \text{Tr} [e^{-iHt} \delta(L\rho - N) \mathbb{P}_S], \quad (\text{B.20})$$

where  $\mathbb{P}_S$  is the projector onto the totally-symmetric subspace. Let us now present arguments leading to an educated guess for this lattice SFF. The idea is to start from the factorized result in Eq. (B.19) and rework it in order to see it as resulting from a single trace of a permutation-symmetric operator.

Let us first introduce the eigen-basis of the impurity Hamiltonian  $h_{\text{imp}}$  evaluated at the saddle point:  $h_{\text{imp}}|e_n\rangle = e_n|e_n\rangle$  for  $n = 1 \dots d$  where  $d$  is the dimension of the local Hilbert space. Rewriting the RHS of Eq. (B.19) as  $k(t)^L = k(t) \times k(t) \times \dots \times k(t) = |\sum_{n_1, \dots, n_L} \langle e_{n_1} | e^{-i h_{\text{imp}} t} | e_{n_1} \rangle \dots \langle e_{n_L} | e^{-i h_{\text{imp}} t} | e_{n_L} \rangle|^2$ , and given that, in the mean-field approach, the relevant part of the lattice Hilbert space is composed of factorized states of the form  $|e_n, \dots, e_n\rangle := |e_n\rangle^{(1)} \dots |e_n\rangle^{(L)}$ , we propose the following expression for the lattice SFF in the permutation-symmetric sector at large  $L$ :  $K_L^\rho(t) \stackrel{?}{\approx} |\sum_n \langle e_n | e^{-i h_{\text{imp}} t} | e_n \rangle \dots \langle e_n | e^{-i h_{\text{imp}} t} | e_n \rangle|^2 = |\sum_n \langle e_n, \dots, e_n | e^{-i(h_{\text{imp}}^{(1)} + \dots + h_{\text{imp}}^{(L)})t} | e_n, \dots, e_n \rangle|^2$

where the latter expression clearly displays the permutation symmetry. This amounts in speculating that in the permutation-symmetric sector, and at large  $L$ , the lattice SFF is related to the impurity SFF via

$$K_L^\rho(t) \stackrel{?}{\approx}_{L \rightarrow \infty} k(Lt) \tag{B.21}$$

rather than the relation in Eq. (B.19) which was derived without consideration for permutation symmetry. In the RHS,  $L$  enters as a multiplicative scale to the impurity spectrum. However, this scale is simply gauged out if one computes the SFF from unfolded spectra as is customary (see Appendix [A]). Ultimately, this amounts in speculating the simple relation

$$K_L^\rho(t) \stackrel{?}{\approx} k(t), \tag{B.22}$$

where  $K_L^\rho(t)$  is the SFF computed from the totally-symmetric sector of the unfolded spectrum of the all-to-all lattice model in defined in Eq. (B.1) and  $k(t)$  is the SFF of the unfolded impurity model defined in Eq. (B.13).

# Appendix C

## DOS effects on the connected SFF for Poisson numbers

Let us consider the Poisson numbers generated as shown in Eq. (2.20) which has the 2-point probability distribution  $P(E_n, n; E_m, m)$  given by

$$P(E_n, n; E_m, m) = p(E_n, n) p(E_m - E_n, m - n), \quad (\text{C.1})$$

where  $p(E_k, k)$  is the well known Poisson distribution

$$p(E_k, k) = \begin{cases} \frac{e^{-\frac{E_k}{\mu}}}{\mu^{(k-1)!}} \left(\frac{E_k}{\mu}\right)^{k-1} & E_k \geq 0 \\ 0 & E_k < 0 \end{cases} \quad (\text{C.2})$$

with  $E_k > 0$  and  $k = 1, 2, 3, \dots$ . As mentioned in the main text, the SFF and CSFF can be computed to get the following expressions (see Ref. [84] and the supplementary materials of Ref. [83] for the derivation)

$$K(\tau, N) = N + \frac{2}{(\mu\tau)^2} - \frac{(1 + i\mu\tau)^{1-N} + (1 - i\mu\tau)^{1-N}}{(\mu\tau)^2}, \quad (\text{C.3})$$

$$K_c(\tau, N) = N + \frac{1}{(\mu\tau)^2} - \frac{(1 + (\mu\tau)^2)^{-N}}{(\mu\tau)^2} - \frac{i}{\mu\tau} [(1 + i\mu\tau)^{-N} - (1 - i\mu\tau)^{-N}]. \quad (\text{C.4})$$

We now focus on the intermediate  $\tau$  regime  $\frac{1}{N} < \mu\tau < 1$  where the expressions reduce

to

$$K(\tau, N) - N = \frac{2}{(\mu\tau)^2} + \dots \quad (\text{C.5})$$

$$K_c(\tau, N) - N = \frac{1}{(\mu\tau)^2} + \dots \quad (\text{C.6})$$

A noticeable feature in Eqs. (C.5, C.6) is that the SFF and the CSFF have different overall coefficients in the power-law scaling. The reason for this is in the nature of the density of states (DOS) for the Poisson numbers discussed in the main text - since the energies are chosen to be positive definite, the ensemble-averaged DOS has a sharp edge at  $E = 0$  as shown in Fig. 5.5. We argued that the sharp edge in the DOS has no effect on the SFF. To understand the effect on the connected SFF, let us rewrite the expression for the SFF and CSFF in terms of the DOS. For this, let us introduce the quantity  $Z(\tau, N)$  which relates the SFF ( $K(\tau, N)$ ) and CSFF ( $K_c(\tau, N)$ ) as follows

$$K(\tau, N) = K_c(\tau, N) + |Z(\tau, N)|^2, \quad (\text{C.7})$$

$$Z(\tau, N) = \left\langle \sum_{m=1}^N e^{i\tau E_m} \right\rangle = N \int_{-\infty}^{\infty} dE e^{-\tau E} \rho(E, N). \quad (\text{C.8})$$

This means that  $Z(\tau, N)$  is related to the Fourier transform of the many-body density of states. It is important to note that the effect of a hard edge in the spectrum by shifting the lowest energy state to zero, will have a strong effect in the Fourier transform as follows

$$Z(\tau, N) = \frac{1}{\mu\tau} + \mathcal{O}\left(\frac{1}{N}\right), \quad (\text{C.9})$$

$$|Z(\tau, N)|^2 = \frac{1}{(\mu\tau)^2} + \mathcal{O}\left(\frac{1}{N}\right), \quad (\text{C.10})$$

Eq. (C.7) tells us that the difference in the coefficient of the power-law scaling between  $K(\tau, N)$  and  $K_c(\tau, N)$  arises precisely from the sharp spectral edge. On the other hand, energy levels selected from an ensemble of levels that do not have a sharp edge such as

those considered in Sections [5.1,5.2] have

$$Z(\tau, N) = \mathcal{O}\left(\frac{1}{N}\right), \quad (\text{C.11})$$

$$K(\tau, N) \sim K_c(\tau, N) \sim N + \frac{2}{(\mu\tau)^2} + \dots \quad (\text{C.12})$$

i.e. both  $K(\tau, N)$  and  $K_c(\tau, N)$  have the same coefficient for the power-law scaling form. In summary, the sharp features in the DOS have no effect on the SFF but double the coefficient of the power-law scaling form in the connected SFF. Eliminating sharp features in the DOS has the desirable effect of leaving the power-law scaling form identical for the SFF and CSFF.



# Appendix D

## Sensitivity of $\chi(0, N)$ data on binning size

The plots on the lower column of Fig. 5.3 were presented for a specific size of histogram bins used to produce  $\chi(x, N)$  from which  $\chi(0, N)$  was extracted. In Fig. D.1, we see that the curves are robust to a range of bin sizes (60/1500, 60/3000, 60/6000). In particular, the location of disorder strength where the curves for different system sizes cross, which estimates the transition between MBL and ergodic phases is unchanged. However, in order to use  $N\chi(0, N)$  as an order parameter as we have done in Fig. 5.3, we need to make sure that the size is not smaller than  $\delta_L$  as defined in Section [5.3.1], where it probes the finite-size level repulsions.

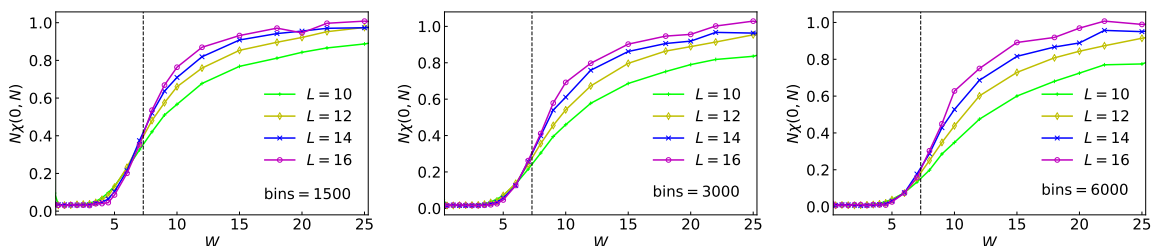


Figure D.1: Plots of  $N\chi(0, N)$  for the disordered spin chain Eq. (5.1) versus disorder strength  $W$  computed using different number of bins to construct histograms. Data averaged over 50000, 30000, 20000, 5000 disorder samples for system sizes  $L = 10, 12, 14, 16$  respectively. The estimate for critical disorder strength  $W^*$  (dashed line) corresponding to the location where curves of different system sizes cross is unchanged with binning sizes.  $N = 20$  levels used from middle of spectrum of each disorder sample and scaled to set mean level spacing to unity.



# Appendix E

## Numerical parameters used to produce main text figures

We list the details of various numerical parameters (number of disorder samples) used to produce Figs (5.1, 5.2, 5.3, 5.5, 5.8, 5.4) in Chapter [5].

20,000	30,000	30,000
17,500	44,000	20,000.

Table E.1: Number of disorder samples used to produce plots in Fig. 5.1.

30,000	30,000	30,000
30,000	30,000	30,000.

Table E.2: Number of disorder samples used to produce plots in Fig. 5.2. To produce the histograms, 1500 bins are used for values of  $x \in [-30, 30]$  (also see Appendix [D] for details on sensitivity to binning).

L=10: 50,000	L=8: 40,000	L=10: 50,000
L=12: 30,000	L=10: 30,000	L=12: 30,000
L=14: 20,000	L=12: 2,000	L=14: 20,000
L=16: 5,000		L=16: 5,000
L=10: 50,000	L=8: 40,000	L=10: 50,000
L=12: 30,000	L=10: 30,000	L=12: 30,000
L=14: 20,000	L=12: 2,000	L=14: 20,000
L=16: 5,000		L=16: 5,000

Table E.3: Number of disorder samples used to produce plots in Fig. 5.3. To produce the histograms, 1500 bins are used for values of  $x$  between  $-30$  to  $30$  (also see Appendix [D] for details on sensitivity to binning).

L=10: 20,000
L=12: 20,000
L=14: 20,000
L=16: 10,000
L=12: 20,000
L=14: 20,000
L=16: 10,000

Table E.4: The number of disorder samples used to produce plots in Fig. 5.4.

NA	NA	2,500
40,000	40,000	17,500.

Table E.5: Number of disorder samples used to produce plots in Fig. 5.5. The entries marked NA correspond to exact analytical plots.

L=10: 50,000
L=12: 30,000
L=14: 20,000
L=10: 50,000
L=12: 30,000
L=14: 20,000
L=16: 5,000

Table E.6: The number of disorder samples used to produce plots in Fig. 5.8.

# Bibliography

- [1] Linda E Reichl. *The transition to chaos*, volume 6. Springer, 1992. [1](#)
- [2] Steven H. Strogatz. *Nonlinear Dynamics and Chaos*. Perseus Books, 1996. [1](#)
- [3] H. Goldstein, C.P. Poole, and J.L. Safko. *Classical Mechanics*. Addison Wesley, 2002. [1](#), [44](#)
- [4] Vladimir Igorevich Arnol'd. *Mathematical methods of classical mechanics*, volume 60. Springer Science & Business Media, 2013. [1](#)
- [5] Muthusamy Lakshmanan and Shanmuganathan Rajaseekar. *Nonlinear dynamics: integrability, chaos and patterns*. Springer Science & Business Media, 2012. [1](#), [44](#)
- [6] J.M.T. Thompson and H.B. Stewart. *Nonlinear Dynamics and Chaos*. Wiley, 2002. [1](#)
- [7] George M Zaslavsky. *Hamiltonian chaos and fractional dynamics*. Oxford University Press, 2004. [1](#)
- [8] K.T. Alligood, T.D. Sauer, and J.A. Yorke. *Chaos: An Introduction to Dynamical Systems*. Textbooks in Mathematical Sciences. Springer, 2000. [1](#)
- [9] T. Tél, M. Gruiz, K. Kulacsy, and S. Hadobas. *Chaotic Dynamics: An Introduction Based on Classical Mechanics*. Chaotic Dynamics: An Introduction Based on Classical Mechanics. Cambridge University Press, 2006. [1](#)
- [10] P Cvitanovic, R Artuso, R Mainieri, G Tanner, and G Vattay. *Chaos: Classical and Quantum*. Niels Bohr Institute, Copenhagen, 2005. [1](#)
- [11] Aleksandr Mikhailovich Lyapunov. The general problem of the stability of motion. *Int. J. Control*, 55(3):531–534, 1992. [1](#)

- [12] J. P. Eckmann and D. Ruelle. Ergodic theory of chaos and strange attractors. *Rev. Mod. Phys.*, 57:617–656, Jul 1985. [1](#)
- [13] Ludwig Arnold and V Wihstutz. *Lyapunov Exponents*. Lecture Notes in Mathematics. Springer-Verlag, 1986. [1](#)
- [14] M.L. Mehta. *Random Matrices*. ISSN. Elsevier Science, 2004. [1](#), [7](#), [9](#), [15](#), [18](#), [19](#)
- [15] Gernot Akemann, Jinho Baik, and Philippe Di Francesco. *The Oxford handbook of random matrix theory*. Oxford University Press, 2011. [1](#)
- [16] Thomas Guhr, Axel Müller-Groeling, and Hans A. Weidenmüller. Random-matrix theories in quantum physics: common concepts. *Phys. Rep.*, 299(4):189–425, 1998. [1](#), [73](#)
- [17] Fritz Haake. *Quantum signatures of chaos*. Quantum Coherence in Mesoscopic Systems. Springer, 2010. [1](#), [3](#), [25](#), [26](#), [28](#)
- [18] Hans-Jürgen Stöckmann. *Quantum Chaos: An Introduction*. Cambridge University Press, 1999. [1](#)
- [19] Martin C Gutzwiller. *Chaos in classical and quantum mechanics*, volume 1. Springer Science & Business Media, 2013. [1](#), [14](#)
- [20] Mark Srednicki. Chaos and quantum thermalization. *Phys. Rev. E*, 50:888–901, Aug 1994. [1](#), [2](#)
- [21] J. M. Deutsch. Quantum statistical mechanics in a closed system. *Phys. Rev. A*, 43:2046–2049, Feb 1991. [1](#)
- [22] Mark Srednicki. The approach to thermal equilibrium in quantized chaotic systems. *Journal of Physics A: Mathematical and General*, 32(7):1163–1175, jan 1999. [1](#), [21](#)
- [23] S. Schmidt, D. Gerace, A. A. Houck, G. Blatter, and H. E. Türeci. Nonequilibrium delocalization-localization transition of photons in circuit quantum electrodynamics. *Phys. Rev. B*, 82:100507, Sep 2010. [1](#)

- [24] J. Raftery, D. Sadri, S. Schmidt, H. E. Türeci, and A. A. Houck. Observation of a dissipation-induced classical to quantum transition. *Phys. Rev. X*, 4:031043, Sep 2014. [1](#)
- [25] C. E. Creffield, G. Hur, and T. S. Monteiro. Localization-delocalization transition in a system of quantum kicked rotors. *Phys. Rev. Lett.*, 96:024103, Jan 2006. [1](#)
- [26] Fritz Haake. *Quantum Signatures of Chaos*, volume 54 of *Quantum Coherence in Mesoscopic Systems*. Springer, 2010. [1](#), [41](#), [42](#)
- [27] Michael Victor Berry and Michael Tabor. Level clustering in the regular spectrum. *Proceedings of the Royal Society of London. A. Mathematical and Physical Sciences*, 356(1686):375–394, 1977. [2](#)
- [28] O. Bohigas, M. J. Giannoni, and C. Schmit. Characterization of chaotic quantum spectra and universality of level fluctuation laws. *Phys. Rev. Lett.*, 52:1–4, Jan 1984. [2](#), [36](#)
- [29] Rainer Grobe, Fritz Haake, and Hans-Jürgen Sommers. Quantum distinction of regular and chaotic dissipative motion. *Phys. Rev. Lett.*, 61:1899–1902, Oct 1988. [2](#), [10](#), [28](#)
- [30] T. A. Brody, J. Flores, J. B. French, P. A. Mello, A. Pandey, and S. S. M. Wong. Random-matrix physics: spectrum and strength fluctuations. *Rev. Mod. Phys.*, 53:385–479, Jul 1981. [2](#), [10](#)
- [31] Theodore C. Hsu and J. C. Anglès d’Auriac. Level repulsion in integrable and almost-integrable quantum spin models. *Phys. Rev. B*, 47:14291–14296, Jun 1993. [2](#), [10](#)
- [32] Vladimir Zelevinsky, B.Alex Brown, Njema Frazier, and Mihai Horoi. The nuclear shell model as a testing ground for many-body quantum chaos. *Phys. Rep.*, 276(2):85–176, 1996. [2](#), [10](#)
- [33] V.K.B. Kota. Embedded random matrix ensembles for complexity and chaos in finite interacting particle systems. *Phys. Rep.*, 347(3):223–288, 2001. [2](#), [10](#), [39](#)
- [34] L F Santos. Integrability of a disordered Heisenberg spin-1/2 chain. *J. Phys. A*, 37(17):4723–4729, apr 2004. [2](#), [10](#)

- [35] Kazue Kudo and Tetsuo Deguchi. Level statistics of xxz spin chains with discrete symmetries: Analysis through finite-size effects. *J. Phys. Soc. Jpn.*, 74(7):1992–2000, 2005. [2](#), [10](#)
- [36] Lea F. Santos and Marcos Rigol. Onset of quantum chaos in one-dimensional bosonic and fermionic systems and its relation to thermalization. *Phys. Rev. E*, 81:036206, Mar 2010. [2](#), [10](#)
- [37] Arijeet Pal and David A. Huse. Many-body localization phase transition. *Phys. Rev. B*, 82:174411, Nov 2010. [2](#), [10](#)
- [38] Aviva Gubin and Lea F. Santos. Quantum chaos: An introduction via chains of interacting spins 1/2. *Am. J. Phys.*, 80(3):246–251, 2012. [2](#), [10](#)
- [39] Dmitry A. Abanin, Ehud Altman, Immanuel Bloch, and Maksym Serbyn. Colloquium: Many-body localization, thermalization, and entanglement. *Rev. Mod. Phys.*, 91:021001, May 2019. [2](#), [10](#)
- [40] Ryusuke Hamazaki, Kohei Kawabata, and Masahito Ueda. Non-hermitian many-body localization. *Phys. Rev. Lett.*, 123:090603, Aug 2019. [2](#)
- [41] Lucas Sá, Pedro Ribeiro, and Tomaž Prosen. Complex spacing ratios: A signature of dissipative quantum chaos. *Phys. Rev. X*, 10:021019, Apr 2020. [2](#)
- [42] Soumi Ghosh, Sparsh Gupta, and Manas Kulkarni. Spectral properties of disordered interacting non-hermitian systems. *Phys. Rev. B*, 106:134202, Oct 2022. [2](#)
- [43] AI Larkin and Yu N Ovchinnikov. Quasiclassical method in the theory of superconductivity. *Sov. Phys. JETP*, 28(6):1200–1205, 1969. [2](#)
- [44] Yasuhiro Sekino and L. Susskind. Fast scramblers. *Journal of High Energy Physics*, 2008(10):065, oct 2008. [2](#)
- [45] Juan Maldacena, Stephen H Shenker, and Douglas Stanford. A bound on chaos. *J. High Energy Phys.*, 2016(8):1–17, 2016. [2](#)
- [46] Brian Swingle. Unscrambling the physics of out-of-time-order correlators. *Nature Physics*, 14(10):988–990, 2018. [2](#)

- [47] E. Fermi, P Pasta, S Ulam, and M Tsingou. Studies of the nonlinear problems. Technical report, Los Alamos National Laboratory (LANL), Los Alamos, NM (United States), 05 1955. [2](#)
- [48] Thierry Dauxois. Fermi, pasta, ulam, and a mysterious lady. *Physics Today*, 61(1):55–57, 01 2008. [2](#)
- [49] Frederick Reif. Fundamentals of statistical and thermal physics. 1973. [2](#)
- [50] Marcos Rigol, Vanja Dunjko, and Maxim Olshanii. Thermalization and its mechanism for generic isolated quantum systems. *Nature*, 452(7189):854–858, 2008. [2](#)
- [51] Anatoli Polkovnikov Luca D’Alessio, Yariv Kafri and Marcos Rigol. From quantum chaos and eigenstate thermalization to statistical mechanics and thermodynamics. *Advances in Physics*, 65(3):239–362, 2016. [2](#)
- [52] Hyungwon Kim, Tatsuhiko N. Ikeda, and David A. Huse. Testing whether all eigenstates obey the eigenstate thermalization hypothesis. *Phys. Rev. E*, 90:052105, Nov 2014. [3](#), [50](#)
- [53] Rahul Nandkishore and David A Huse. Many-body localization and thermalization in quantum statistical mechanics. *Annu. Rev. Condens. Matter Phys.*, 6(1):15–38, 2015. [3](#), [21](#)
- [54] Dmitry A Abanin, Ehud Altman, Immanuel Bloch, and Maksym Serbyn. Colloquium: Many-body localization, thermalization, and entanglement. *Reviews of Modern Physics*, 91(2):021001, 2019. [3](#), [21](#)
- [55] Sarang Gopalakrishnan and SA Parameswaran. Dynamics and transport at the threshold of many-body localization. *Physics Reports*, 2020. [3](#), [21](#)
- [56] Dong-Ling Deng, Sriram Ganeshan, Xiaopeng Li, Ranjan Modak, Subroto Mukerjee, and JH Pixley. Many-body localization in incommensurate models with a mobility edge. *Annalen der Physik*, 529(7):1600399, 2017. [3](#), [21](#)
- [57] John Z. Imbrie. On Many-Body Localization for Quantum Spin Chains. *Journal of Statistical Physics*, 163(5):998–1048, June 2016. [3](#), [21](#)

- [58] Bill Sutherland. *Beautiful models: 70 years of exactly solved quantum many-body problems*. World Scientific, 2004. [3](#), [21](#)
- [59] Toshiya Kinoshita, Trevor Wenger, and David S Weiss. A quantum newton’s cradle. *Nature*, 440(7086):900–903, 2006. [3](#), [21](#)
- [60] Marcos Rigol. Breakdown of thermalization in finite one-dimensional systems. *Phys. Rev. Lett.*, 103:100403, Sep 2009. [3](#), [21](#)
- [61] Maksym Serbyn, Dmitry A Abanin, and Zlatko Papić. Quantum many-body scars and weak breaking of ergodicity. *Nature Physics*, 17(6):675–685, 2021. [3](#), [21](#)
- [62] Sanjay Moudgalya, B Andrei Bernevig, and Nicolas Regnault. Quantum many-body scars and hilbert space fragmentation: a review of exact results. *Reports on Progress in Physics*, 85(8):086501, jul 2022. [3](#), [21](#)
- [63] Michael Schreiber, Sean S Hodgman, Pranjal Bordia, Henrik P Lüschen, Mark H Fischer, Ronen Vosk, Ehud Altman, Ulrich Schneider, and Immanuel Bloch. Observation of many-body localization of interacting fermions in a quasirandom optical lattice. *Science*, 349(6250):842–845, 2015. [3](#)
- [64] Jae-yoon Choi, Sebastian Hild, Johannes Zeiher, Peter Schauß, Antonio Rubio-Abadal, Tarik Yefsah, Vedika Khemani, David A Huse, Immanuel Bloch, and Christian Gross. Exploring the many-body localization transition in two dimensions. *Science*, 352(6293):1547–1552, 2016. [3](#)
- [65] Alexander Lukin, Matthew Rispoli, Robert Schittko, M Eric Tai, Adam M Kaufman, Soonwon Choi, Vedika Khemani, Julian Léonard, and Markus Greiner. Probing entanglement in a many-body-localized system. *Science*, 364(6437):256–260, 2019. [3](#)
- [66] J. Smith, A. Lee, P. Richerme, B. Neyenhuis, P. W. Hess, P. Hauke, M. Heyl, D. A. Huse, and C. Monroe. Many-body localization in a quantum simulator with programmable random disorder. *Nature Physics*, 12(10):907–911, Jun 2016. [3](#)
- [67] Pedram Roushan, C Neill, J Tangpanitanon, VM Bastidas, A Megrant, R Barends, Yu Chen, Z Chen, B Chiaro, A Dunsworth, et al. Spectroscopic signatures

- of localization with interacting photons in superconducting qubits. *Science*, 358(6367):1175–1179, 2017. [3](#)
- [68] Kai Xu, Jin-Jun Chen, Yu Zeng, Yu-Ran Zhang, Chao Song, Wuxin Liu, Qiu-jiang Guo, Pengfei Zhang, Da Xu, Hui Deng, Keqiang Huang, H. Wang, Xiaobo Zhu, Dongning Zheng, and Heng Fan. Emulating many-body localization with a superconducting quantum processor. *Phys. Rev. Lett.*, 120:050507, Feb 2018. [3](#)
- [69] Ken Xuan Wei, Chandrasekhar Ramanathan, and Paola Cappellaro. Exploring localization in nuclear spin chains. *Phys. Rev. Lett.*, 120:070501, Feb 2018. [3](#)
- [70] Vadim Oganesyan and David A. Huse. Localization of interacting fermions at high temperature. *Phys. Rev. B*, 75:155111, Apr 2007. [3](#), [11](#), [30](#), [39](#)
- [71] Fritz Haake. *Quantum Signatures of Chaos*, volume 54. 2010. [3](#), [13](#), [14](#), [15](#), [16](#)
- [72] Jordan Cotler, Nicholas Hunter-Jones, Junyu Liu, and Beni Yoshida. Chaos, complexity, and random matrices. *Journal of High Energy Physics*, 2017(11), Nov 2017. [3](#), [13](#), [15](#), [16](#), [19](#)
- [73] Hrant Gharibyan, Masanori Hanada, Stephen H Shenker, and Masaki Tezuka. Onset of random matrix behavior in scrambling systems. *Journal of High Energy Physics*, 2018(7):124, 2018. [3](#), [13](#), [15](#), [16](#)
- [74] Junyu Liu. Spectral form factors and late time quantum chaos. *Phys. Rev. D*, 98:086026, Oct 2018. [3](#), [13](#), [15](#), [16](#), [19](#)
- [75] Xiao Chen and Andreas W. W. Ludwig. Universal spectral correlations in the chaotic wave function and the development of quantum chaos. *Phys. Rev. B*, 98:064309, Aug 2018. [3](#), [13](#), [15](#), [19](#)
- [76] Bruno Bertini, Pavel Kos, and Tomaž Prosen. Exact spectral form factor in a minimal model of many-body quantum chaos. *Phys. Rev. Lett.*, 121:264101, Dec 2018. [3](#), [13](#), [15](#)
- [77] Pavel Kos, Marko Ljubotina, and Tomaž Prosen. Many-body quantum chaos: Analytic connection to random matrix theory. *Phys. Rev. X*, 8:021062, Jun 2018. [3](#), [13](#), [15](#)

- [78] Maksym Serbyn and Joel E. Moore. Spectral statistics across the many-body localization transition. *Phys. Rev. B*, 93:041424, Jan 2016. [3](#)
- [79] Vadim Oganesyan and David A. Huse. Localization of interacting fermions at high temperature. *Phys. Rev. B*, 75:155111, Apr 2007. [3](#)
- [80] Piotr Sierant and Jakub Zakrzewski. Level statistics across the many-body localization transition. *Phys. Rev. B*, 99:104205, Mar 2019. [3](#)
- [81] Wouter Buijsman, Vadim Cheianov, and Vladimir Gritsev. Random matrix ensemble for the level statistics of many-body localization. *Phys. Rev. Lett.*, 122:180601, May 2019. [3](#)
- [82] Piotr Sierant and Jakub Zakrzewski. Model of level statistics for disordered interacting quantum many-body systems. *Phys. Rev. B*, 101:104201, Mar 2020. [3](#)
- [83] Abhishodh Prakash, J. H. Pixley, and Manas Kulkarni. Universal spectral form factor for many-body localization. *Phys. Rev. Research*, 3:L012019, Feb 2021. [3](#), [13](#), [14](#), [15](#), [16](#), [17](#), [47](#), [49](#), [50](#), [52](#), [54](#), [56](#), [59](#), [81](#)
- [84] Roman Riser, Vladimir Al Osipov, and Eugene Kanzieper. Nonperturbative theory of power spectrum in complex systems. *Annals of Physics*, 413:168065, 2020. [3](#), [16](#), [17](#), [59](#), [81](#)
- [85] Roman Riser and Eugene Kanzieper. Power spectrum and form factor in random diagonal matrices and integrable billiards. *Annals of Physics*, 425:168393, 2021. [3](#), [16](#)
- [86] Nikolay V. Vitanov, Andon A. Rangelov, Bruce W. Shore, and Klaas Bergmann. Stimulated raman adiabatic passage in physics, chemistry, and beyond. *Rev. Mod. Phys.*, 89:015006, Mar 2017. [3](#)
- [87] Amit Dey, Doron Cohen, and Amichay Vardi. Adiabatic passage through chaos. *Phys. Rev. Lett.*, 121:250405, Dec 2018. [3](#)
- [88] Amit Dey, Doron Cohen, and Amichay Vardi. Many-body adiabatic passage: Quantum detours around chaos. *Phys. Rev. A*, 99:033623, Mar 2019. [3](#)

- [89] Amit Dey and Manas Kulkarni. Emergence of chaos and controlled photon transfer in a cavity-qed network. *Phys. Rev. Res.*, 2:042004, Oct 2020. [3](#)
- [90] C. M. Lóbez and A. Relaño. Can we retrieve information from quantum thermalized states? *J. Stat. Mech.: Theory Exp.*, 2021(8):083104, aug 2021. [3](#)
- [91] Christoph Berke, Evangelos Varvelis, Simon Trebst, Alexander Altland, and David P DiVincenzo. Transmon platform for quantum computing challenged by chaotic fluctuations. *Nat. Commun.*, 13(1):1, 2022. [3](#)
- [92] Ze-Liang Xiang, Sahel Ashhab, J. Q. You, and Franco Nori. Hybrid quantum circuits: Superconducting circuits interacting with other quantum systems. *Rev. Mod. Phys.*, 85:623–653, Apr 2013. [4](#)
- [93] Markus Aspelmeyer, Tobias J. Kippenberg, and Florian Marquardt. Cavity optomechanics. *Rev. Mod. Phys.*, 86:1391–1452, Dec 2014. [4](#)
- [94] Gershon Kurizki, Patrice Bertet, Yuimaru Kubo, Klaus Mølmer, David Petrosyan, Peter Rabl, and Jörg Schmiedmayer. Quantum technologies with hybrid systems. *Proc. Natl. Acad. Sci. USA*, 112(13):3866–3873, 2015. [4](#)
- [95] Changsuk Noh and Dimitris G Angelakis. Quantum simulations and many-body physics with light. *Rep. Prog. Phys.*, 80(1):016401, nov 2016. [4](#)
- [96] Karyn Le Hur, Loïc Henriët, Alexandru Petrescu, Kirill Plekhanov, Guillaume Roux, and Marco Schiró. Many-body quantum electrodynamics networks: Non-equilibrium condensed matter physics with light. *C. R. Phys.*, 17(8):808–835, 2016. [4](#)
- [97] Audrey Cottet, Matthieu C Dartiailh, Matthieu M Desjardins, Tino Cubaynes, Lauriane C Contamin, Matthieu Delbecq, Jérémie J Viennot, Laure E Bruhat, Benoit Douçot, and Takis Kontos. Cavity QED with hybrid nanocircuits: from atomic-like physics to condensed matter phenomena. *J. Phys. Condens. Matter*, 29(43):433002, sep 2017. [4](#)
- [98] A. A. Clerk, K. W. Lehnert, P. Bertet, J. R. Petta, and Y. Nakamura. Hybrid quantum systems with circuit quantum electrodynamics. *Nat. Phys.*, 16(3):257–267, 2020. [4](#)

- [99] Jirawat Tangpanitanon and Dimitris G Angelakis. Many-body physics and quantum simulations with strongly interacting photons. *Nanoscale Quantum Optics*, 204:169, 2020. [4](#)
- [100] S. Haroche, M. Brune, and J. M. Raimond. From cavity to circuit quantum electrodynamics. *Nat. Phys.*, 16(3):243–246, 2020. [4](#)
- [101] Alexandre Blais, Steven M. Girvin, and William D. Oliver. Quantum information processing and quantum optics with circuit quantum electrodynamics. *Nat. Phys.*, 16(3):247–256, 2020. [4](#)
- [102] Alexandre Blais, Arne L. Grimsmo, S. M. Girvin, and Andreas Wallraff. Circuit quantum electrodynamics. *Rev. Mod. Phys.*, 93:025005, May 2021. [4](#)
- [103] Yoshiro Hirayama, Koji Ishibashi, and Kae Nemoto. *Hybrid Quantum Systems*. Springer, 2021. [4](#)
- [104] I. ANTONIOU, V. BASIOS, and F. BOSCO. Probabilistic control of chaos: The -adic renyi map under control. *International Journal of Bifurcation and Chaos*, 06(08):1563–1573, 1996. [4](#), [63](#)
- [105] I. Antoniou, V. Basios, and F. Bosco. Probabilistic control of chaos: Chaotic maps under control. *Computers Mathematics with Applications*, 34(2):373–389, 1997. [4](#), [63](#)
- [106] I. Antoniou, V. Basios, and F. Bosco. Absolute controllability condition for probabilistic control of chaos. *International Journal of Bifurcation and Chaos*, 08(02):409–413, 1998. [4](#), [63](#)
- [107] Thomas Iadecola, Sriram Ganeshan, J. H. Pixley, and Justin H. Wilson. Measurement and feedback driven entanglement transition in the probabilistic control of chaos. *Phys. Rev. Lett.*, 131:060403, Aug 2023. [4](#), [72](#)
- [108] Martin C. Gutzwiller. Periodic Orbits and Classical Quantization Conditions. *Journal of Mathematical Physics*, 12(3):343–358, 03 1971. [7](#)
- [109] Eugene P. Wigner. Characteristic vectors of bordered matrices with infinite dimensions. *Annals of Mathematics*, 62(3):548–564, 1955. [7](#)

- [110] Eugene P. Wigner. Characteristics vectors of bordered matrices with infinite dimensions ii. *Annals of Mathematics*, 65(2):203–207, 1957. [7](#)
- [111] Eugene P. Wigner. On the distribution of the roots of certain symmetric matrices. *Annals of Mathematics*, 67(2):325–327, 1958. [7](#)
- [112] Freeman J. Dyson. Statistical Theory of the Energy Levels of Complex Systems. I. *Journal of Mathematical Physics*, 3(1):140–156, 01 1962. [7](#)
- [113] Y. Alhassid. The statistical theory of quantum dots. *Rev. Mod. Phys.*, 72:895–968, Oct 2000. [8](#), [9](#)
- [114] Thomas Guhr, Axel Müller–Groeling, and Hans A. Weidenmüller. Random-matrix theories in quantum physics: common concepts. *Physics Reports*, 299(4):189–425, 1998. [9](#)
- [115] O. Bohigas, M.J. Giannoni, and C. Schmit. Spectral properties of the laplacian and random matrix theories. *J. Physique Lett.*, 45(21):1015–1022, 1984. [9](#)
- [116] Michael Victor Berry and Michael Tabor. Level clustering in the regular spectrum. *Proc. R. Soc. London, Ser. A*, 356(1686):375–394, 1977. [10](#)
- [117] Gernot Akemann, Mario Kieburg, Adam Mielke, and Tomaž Prosen. Universal signature from integrability to chaos in dissipative open quantum systems. *Phys. Rev. Lett.*, 123:254101, Dec 2019. [10](#), [11](#), [27](#), [28](#)
- [118] Jean Ginibre. Statistical Ensembles of Complex, Quaternion, and Real Matrices. *Journal of Mathematical Physics*, 6(3):440–449, 03 1965. [11](#)
- [119] Ryusuke Hamazaki, Kohei Kawabata, and Masahito Ueda. Non-hermitian many-body localization. *Phys. Rev. Lett.*, 123:090603, Aug 2019. [11](#)
- [120] Yi Huang and BI Shklovskii. Anderson transition in three-dimensional systems with non-hermitian disorder. *Physical Review B*, 101(1):014204, 2020. [11](#)
- [121] Y. Y. Atas, E. Bogomolny, O. Giraud, and G. Roux. Distribution of the ratio of consecutive level spacings in random matrix ensembles. *Phys. Rev. Lett.*, 110:084101, Feb 2013. [11](#), [30](#), [40](#)

- [122] Y Y Atas, E Bogomolny, O Giraud, P Vivo, and E Vivo. Joint probability densities of level spacing ratios in random matrices. *J. Phys. A*, 46(35):355204, aug 2013. [11](#), [40](#)
- [123] Olivier Giraud, Nicolas Macé, Éric Vernier, and Fabien Alet. Probing symmetries of quantum many-body systems through gap ratio statistics. *Phys. Rev. X*, 12:011006, Jan 2022. [11](#), [40](#)
- [124] Lucas Sá, Pedro Ribeiro, and Tomaž Prosen. Complex spacing ratios: A signature of dissipative quantum chaos. *Phys. Rev. X*, 10:021019, Apr 2020. [12](#), [30](#), [32](#)
- [125] D. J. Thouless. Maximum metallic resistance in thin wires. *Phys. Rev. Lett.*, 39:1167–1169, Oct 1977. [14](#)
- [126] O. L. Al'tshuler and B. I. Shklovskii. Repulsion of energy levels and conductivity of small metal samples. *Soviet Journal of Experimental and Theoretical Physics*, 64(1):127, July 1986. [14](#)
- [127] Amos Chan, Andrea De Luca, and J. T. Chalker. Spectral statistics in spatially extended chaotic quantum many-body systems. *Phys. Rev. Lett.*, 121:060601, Aug 2018. [14](#)
- [128] Mauro Schiulaz, E. Jonathan Torres-Herrera, and Lea F. Santos. Thouless and relaxation time scales in many-body quantum systems. *Phys. Rev. B*, 99:174313, May 2019. [14](#)
- [129] David A. Zarate-Herrada, Lea F. Santos, and E. Jonathan Torres-Herrera. Generalized survival probability. *Entropy*, 25(2), 2023. [15](#)
- [130] Ceren B Dağ, Simeon I Mistakidis, Amos Chan, and Hossein R Sadeghpour. Many-body quantum chaos in stroboscopically-driven cold atoms. *Communications Physics*, 6(1):136, 2023. [15](#)
- [131] Michael Winer and Brian Swingle. Hydrodynamic theory of the connected spectral form factor. *Phys. Rev. X*, 12:021009, Apr 2022. [15](#)
- [132] J. M. Deutsch. Quantum statistical mechanics in a closed system. *Phys. Rev. A*, 43:2046–2049, Feb 1991. [21](#)

- [133] R. H. Dicke. Coherence in spontaneous radiation processes. *Phys. Rev.*, 93:99–110, Jan 1954. [23](#)
- [134] M Gross and S Haroche. Superradiance: An essay on the theory of collective spontaneous emission. *Phys. Rep.*, 93(5):301–396, 1982. [23](#)
- [135] Barry M. Garraway. The Dicke model in quantum optics: Dicke model revisited. *Philos. Trans. R. Soc. London, Ser. A*, 369(1939):1137–1155, 2011. [23](#)
- [136] Klaus Hepp and Elliott H Lieb. On the superradiant phase transition for molecules in a quantized radiation field: the Dicke maser model. *Ann. Phys. (N.Y.)*, 76(2):360–404, 1973. [23](#)
- [137] Peter Kirton, Mor M. Roses, Jonathan Keeling, and Emanuele G. Dalla Torre. Introduction to the Dicke model: From equilibrium to nonequilibrium, and vice versa. *Adv. Quantum Technol.*, 2(1-2):1800043, 2019. [23](#), [24](#)
- [138] Clive Emary and Tobias Brandes. Quantum chaos triggered by precursors of a quantum phase transition: The Dicke model. *Phys. Rev. Lett.*, 90:044101, Jan 2003. [23](#), [35](#)
- [139] Clive Emary and Tobias Brandes. Chaos and the quantum phase transition in the Dicke model. *Phys. Rev. E*, 67:066203, Jun 2003. [23](#), [29](#), [37](#), [43](#)
- [140] Victor V. Albert and Liang Jiang. Symmetries and conserved quantities in lindblad master equations. *Phys. Rev. A*, 89:022118, Feb 2014. [24](#), [25](#)
- [141] Berislav Buča and Tomaz Prosen. A note on symmetry reductions of the lindblad equation: transport in constrained open spin chains. *New J. Phys.*, 14(7):073007, jul 2012.
- [142] Simon Lieu, Ron Belyansky, Jeremy T. Young, Rex Lundgren, Victor V. Albert, and Alexey V. Gorshkov. Symmetry breaking and error correction in open quantum systems. *Phys. Rev. Lett.*, 125:240405, Dec 2020. [24](#), [25](#)
- [143] *Supplementary material.* [24](#)

- [144] F. Dimer, B. Estienne, A. S. Parkins, and H. J. Carmichael. Proposed realization of the Dicke-model quantum phase transition in an optical cavity qed system. *Phys. Rev. A*, 75:013804, Jan 2007. [24](#)
- [145] Mor M Roses and Emanuele G Dalla Torre. Dicke model. *PLoS ONE*, 15(9):1–8, 2020. [24](#), [35](#)
- [146] Shaul Mukamel. *Principles of nonlinear optical spectroscopy*. Number 6. Oxford University Press, 1999. [25](#)
- [147] Norbert Rosenzweig and Charles E. Porter. "repulsion of energy levels" in complex atomic spectra. *Phys. Rev.*, 120:1698–1714, Dec 1960. [26](#)
- [148] H. Markum, R. Pullirsch, and T. Wettig. Non-hermitian random matrix theory and lattice qed with chemical potential. *Phys. Rev. Lett.*, 83:484–487, Jul 1999. [27](#)
- [149] Ryusuke Hamazaki, Kohei Kawabata, Naoto Kura, and Masahito Ueda. Universality classes of non-hermitian random matrices. *Phys. Rev. Res.*, 2:023286, Jun 2020. [27](#), [28](#)
- [150] Denis Bernard and André LeClair. A classification of non-hermitian random matrices. In *Statistical Field Theories*, page 207. Springer, 2002. [28](#)
- [151] Takuya Kanazawa and Tilo Wettig. New universality classes of the non-hermitian dirac operator in qed-like theories. *Phys. Rev. D*, 104:014509, Jul 2021. [28](#)
- [152] Antonio M García-García, Lucas Sá, and Jacobus JM Verbaarschot. Symmetry classification and universality in non-hermitian many-body quantum chaos by the sachdev-ye-kitaev model. *arXiv preprint arXiv:2110.03444*, 2021. [28](#)
- [153] BI Shklovskii, B Shapiro, BR Sears, P Lambrianides, and HB Shore. Statistics of spectra of disordered systems near the metal-insulator transition. *Physical Review B*, 47(17):11487, 1993. [29](#)
- [154] B Georgeot and DL Shepelyansky. Integrability and quantum chaos in spin glass shards. *Phys. Rev. Lett.*, 81(23):5129, 1998. [29](#)

- [155] Michael Tavis and Frederick W. Cummings. Exact solution for an  $n$ -molecule—radiation-field hamiltonian. *Phys. Rev.*, 170:379–384, Jun 1968. [33](#)
- [156] Davide Rossini and Rosario Fazio. Mott-insulating and glassy phases of polaritons in 1d arrays of coupled cavities. *Phys. Rev. Lett.*, 99:186401, Oct 2007. [33](#)
- [157] M Gaudin. Diagonalisation d’une classe d’hamiltoniens de spin. *Journal de Physique*, 37(10):1087–1098, 1976. [33](#), [35](#)
- [158] Klaus Hepp and Elliott H Lieb. On the superradiant phase transition for molecules in a quantized radiation field: the Dicke maser model. *Ann. Phys. (N.Y.)*, 76(2):360–404, 1973. [35](#)
- [159] F. T. Hioe. Phase transitions in some generalized Dicke models of superradiance. *Phys. Rev. A*, 8:1440–1445, Sep 1973. [35](#)
- [160] Y. K. Wang and F. T. Hioe. Phase transition in the Dicke model of superradiance. *Phys. Rev. A*, 7:831–836, Mar 1973. [35](#)
- [161] Klaus Hepp and Elliott H. Lieb. Equilibrium statistical mechanics of matter interacting with the quantized radiation field. *Phys. Rev. A*, 8:2517–2525, Nov 1973. [35](#)
- [162] C.H Lewenkopf, M.C Nemes, V Marvulle, M.P Pato, and W.F Wreszinski. Level statistics transitions in the spin-boson model. *Phys. Lett. A*, 155(2):113–116, 1991. [35](#)
- [163] Wouter Buijsman, Vladimir Gritsev, and Rudolf Sprik. Nonergodicity in the anisotropic Dicke model. *Phys. Rev. Lett.*, 118:080601, Feb 2017. [35](#)
- [164] Vir B. Bulchandani, David A. Huse, and Sarang Gopalakrishnan. Onset of many-body quantum chaos due to breaking integrability. *Phys. Rev. B*, 105:214308, Jun 2022. [35](#), [36](#), [40](#)
- [165] J. P. Provost, F. Rocca, G. Vallee, and M. Sirugue. Lack of phase transition in the Dicke model with external fields. *Physica A*, 85(1):202–206, 1976. [36](#)
- [166] Ángel L Corps, Rafael A Molina, and Armando Relaño. Chaos in a deformed dicke model. *J. Phys. A*, 55(8):084001, feb 2022. [36](#), [43](#), [46](#)

- [167] M. A. Bastarrachea-Magnani, S Lerma-Hernández, and J. G. Hirsch. Comparative quantum and semiclassical analysis of atom-field systems. ii. chaos and regularity. *Phys. Rev. A*, 89:032102, Mar 2014. [37](#), [46](#)
- [168] Jorge Chávez-Carlos, B. López-del Carpio, Miguel A. Bastarrachea-Magnani, Pavel Stránský, Sergio Lerma-Hernández, Lea F. Santos, and Jorge G. Hirsch. Quantum and classical lyapunov exponents in atom-field interaction systems. *Phys. Rev. Lett.*, 122:024101, Jan 2019. [37](#)
- [169] Pragna Das and Auditya Sharma. Revisiting the phase transitions of the Dicke model. *Phys. Rev. A*, 105:033716, Mar 2022. [37](#)
- [170] Qing Li, Jin-Lou Ma, and Lei Tan. Eigenstate thermalization and quantum chaos in the jaynes-cummings hubbard model. *Phys. Scr.*, 96(12):125709, 2021. [38](#)
- [171] T Prosen and M Robnik. Energy level statistics in the transition region between integrability and chaos. *Journal of Physics A: Mathematical and General*, 26(10):2371, may 1993. [39](#)
- [172] Frank Schweiner, Jörg Main, and Günter Wunner. Goe-gue-poisson transitions in the nearest-neighbor spacing distribution of magnetoexcitons. *Phys. Rev. E*, 95:062205, Jun 2017. [39](#)
- [173] Pragya Shukla. Disorder perturbed flat bands. ii. search for criticality. *Phys. Rev. B*, 98:184202, Nov 2018. [39](#)
- [174] Antonio M. García-García and Kazutaka Takahashi. Long range disorder and anderson transition in systems with chiral symmetry. *Nuclear Physics B*, 700(1):361–384, 2004. [39](#)
- [175] V E Kravtsov, I M Khaymovich, E Cuevas, and M Amini. A random matrix model with localization and ergodic transitions. *New Journal of Physics*, 17(12):122002, dec 2015. [39](#)
- [176] T. A. Brody, J. Flores, J. B. French, P. A. Mello, A. Pandey, and S. S. M. Wong. Random-matrix physics: spectrum and strength fluctuations. *Rev. Mod. Phys.*, 53:385–479, Jul 1981. [39](#)

- [177] Jordan Cotler, Nicholas Hunter-Jones, Junyu Liu, and Beni Yoshida. Chaos, complexity, and random matrices. *J. High Energy Phys.*, 2017(11):1–60, 2017. [42](#)
- [178] Hrant Gharibyan, Masanori Hanada, Stephen H Shenker, and Masaki Tezuka. Onset of random matrix behavior in scrambling systems. *J. High Energy Phys.*, 2018(7):1–62, 2018. [42](#)
- [179] Junyu Liu. Spectral form factors and late time quantum chaos. *Phys. Rev. D*, 98:086026, Oct 2018. [42](#)
- [180] Xiao Chen and Andreas W. W. Ludwig. Universal spectral correlations in the chaotic wave function and the development of quantum chaos. *Phys. Rev. B*, 98:064309, Aug 2018. [42](#)
- [181] Bruno Bertini, Pavel Kos, and Tomaž Prosen. Exact spectral form factor in a minimal model of many-body quantum chaos. *Phys. Rev. Lett.*, 121:264101, Dec 2018. [42](#)
- [182] Pavel Kos, Marko Ljubotina, and Tomaž Prosen. Many-body quantum chaos: Analytic connection to random matrix theory. *Phys. Rev. X*, 8:021062, Jun 2018. [42](#)
- [183] Miguel Angel Bastarrachea-Magnani, Baldemar López-del Carpio, Jorge Chávez-Carlos, Sergio Lerma-Hernández, and Jorge G Hirsch. Regularity and chaos in cavity QED. *Phys. Scr.*, 92(5):054003, apr 2017. [46](#)
- [184] R. J. Lewis-Swan, Arghavan Safavi-Naini, John J. Bollinger, and Ana M. Rey. Unifying scrambling, thermalization and entanglement through measurement of fidelity out-of-time-order correlators in the Dicke model. *Nat. Commun.*, 10(1):1, 2019. [46](#)
- [185] Alexander Altland and Fritz Haake. Equilibration and macroscopic quantum fluctuations in the Dicke model. *New J. Phys.*, 14(7):073011, 2012. [46](#)
- [186] Jan Šuntajs, Janez Bonča, Tomaž Prosen, and Lev Vidmar. Quantum chaos challenges many-body localization. *Physical Review E*, 102(6):062144, 2020. [49](#), [50](#), [57](#), [58](#)

- [187] Vedika Khemani, S. P. Lim, D. N. Sheng, and David A. Huse. Critical properties of the many-body localization transition. *Phys. Rev. X*, 7:021013, Apr 2017. [50](#)
- [188] Vedika Khemani, D. N. Sheng, and David A. Huse. Two universality classes for the many-body localization transition. *Phys. Rev. Lett.*, 119:075702, Aug 2017. [50](#), [51](#), [52](#)
- [189] Liangsheng Zhang, Vedika Khemani, and David A. Huse. A floquet model for the many-body localization transition. *Phys. Rev. B*, 94:224202, Dec 2016. [50](#)
- [190] Michael Sonner, Maksym Serbyn, Zlatko Papić, and Dmitry A. Abanin. Thouless energy across the many-body localization transition in floquet systems. *Phys. Rev. B*, 104:L081112, Aug 2021. [51](#)
- [191] Shankar Iyer, Vadim Oganesyan, Gil Refael, and David A. Huse. Many-body localization in a quasiperiodic system. *Phys. Rev. B*, 87:134202, Apr 2013. [51](#)
- [192] Xiaopeng Li, Sriram Ganeshan, J. H. Pixley, and S. Das Sarma. Many-body localization and quantum nonergodicity in a model with a single-particle mobility edge. *Phys. Rev. Lett.*, 115:186601, Oct 2015. [51](#)
- [193] Xiaopeng Li, J. H. Pixley, Dong-Ling Deng, Sriram Ganeshan, and S. Das Sarma. Quantum nonergodicity and fermion localization in a system with a single-particle mobility edge. *Phys. Rev. B*, 93:184204, May 2016. [51](#)
- [194] Yevgeny Bar Lev, Dante M Kennes, Christian Klöckner, David R Reichman, and Christoph Karrasch. Transport in quasiperiodic interacting systems: From superdiffusion to subdiffusion. *EPL (Europhysics Letters)*, 119(3):37003, 2017. [51](#)
- [195] F. Setiawan, Dong-Ling Deng, and J. H. Pixley. Transport properties across the many-body localization transition in quasiperiodic and random systems. *Phys. Rev. B*, 96:104205, Sep 2017. [51](#)
- [196] A. Chandran and C. R. Laumann. Localization and symmetry breaking in the quantum quasiperiodic ising glass. *Phys. Rev. X*, 7:031061, Sep 2017. [51](#)
- [197] Marko Žnidarič and Marko Ljubotina. Interaction instability of localization in quasiperiodic systems. *Proceedings of the National Academy of Sciences*, 115(18):4595–4600, 2018. [51](#)

- [198] Shenglong Xu, Xiao Li, Yi-Ting Hsu, Brian Swingle, and S. Das Sarma. Butterfly effect in interacting aubry-andre model: Thermalization, slow scrambling, and many-body localization. *Phys. Rev. Research*, 1:032039, Dec 2019. [51](#)
- [199] Yongchan Yoo, Junhyun Lee, and Brian Swingle. Nonequilibrium steady state phases of the interacting aubry-andré-harper model. *Phys. Rev. B*, 102:195142, Nov 2020. [51](#)
- [200] Utkarsh Agrawal, Sarang Gopalakrishnan, and Romain Vasseur. Universality and quantum criticality in quasiperiodic spin chains. *Nature communications*, 11(1):1–7, 2020. [51](#)
- [201] Jan Šuntajs, Janez Bonča, Tomaž Prosen, and Lev Vidmar. Ergodicity breaking transition in finite disordered spin chains. *Phys. Rev. B*, 102:064207, Aug 2020. [54](#), [55](#)
- [202] J.B. French and S.S.M. Wong. Some random-matrix level and spacing distributions for fixed-particle-rank interactions. *Physics Letters B*, 35(1):5–7, 1971. [59](#), [73](#)
- [203] H. Meyer, J.-C. Anglès d’Auriac, and J.-M. Maillard. Random matrix theory and classical statistical mechanics: Vertex models. *Phys. Rev. E*, 55:5380–5392, May 1997. [59](#)
- [204] Henrik Bruus and Jean-Christian Anglès d’Auriac. Energy level statistics of the two-dimensional hubbard model at low filling. *Phys. Rev. B*, 55:9142–9159, Apr 1997. [59](#)
- [205] T. Guhr, J.-Z. Ma, S. Meyer, and T. Wilke. Statistical analysis and the equivalent of a thouless energy in lattice qcd dirac spectra. *Phys. Rev. D*, 59:054501, Jan 1999. [59](#)
- [206] Wojciech De Roeck and François Huveneers. Stability and instability towards delocalization in many-body localization systems. *Phys. Rev. B*, 95:155129, Apr 2017. [60](#)
- [207] Wojciech De Roeck and John Z Imbrie. Many-body localization: stability and instability. *Philosophical Transactions of the Royal Society A: Mathematical, Physical and Engineering Sciences*, 375(2108):20160422, 2017. [60](#)

- [208] S. J. Garratt, Sthitadhi Roy, and J. T. Chalker. Local resonances and parametric level dynamics in the many-body localized phase. *Phys. Rev. B*, 104:184203, Nov 2021. [60](#), [61](#)
- [209] S. J. Garratt and J. T. Chalker. Many-body delocalization as symmetry breaking. *Phys. Rev. Lett.*, 127:026802, Jul 2021. [62](#)
- [210] Edward Ott, Celso Grebogi, and James A. Yorke. Controlling chaos. *Phys. Rev. Lett.*, 64:1196–1199, Mar 1990. [63](#)
- [211] Fritz Haake, M Kuś, and Rainer Scharf. Classical and quantum chaos for a kicked top. *Zeitschrift für Physik B Condensed Matter*, 65(3):381–395, 1987. [63](#), [64](#), [65](#)
- [212] Giancarlo Benettin, Luigi Galgani, and Jean-Marie Strelcyn. Kolmogorov entropy and numerical experiments. *Phys. Rev. A*, 14:2338–2345, Dec 1976. [67](#)
- [213] Mahaveer Prasad, Hari Kumar Yadalam, Camille Aron, and Manas Kulkarni. Dissipative quantum dynamics, phase transitions, and non-hermitian random matrices. *Phys. Rev. A*, 105:L050201, May 2022. [71](#)
- [214] Haining Pan, Sriram Ganeshan, Thomas Iadecola, Justin H. Wilson, and J. H. Pixley. Local and nonlocal stochastic control of quantum chaos: Measurement- and control-induced criticality. *Phys. Rev. B*, 110:054308, Aug 2024. [72](#)
- [215] Oriol Bohigas. Random matrix theories and chaotic dynamics. In *Chaos et Physique Quantique Chaos And Quantum Physics*, pages 87–199, Les Houches, France, August 1989. North-Holland. [73](#)
- [216] H. Meyer, J. C. Anglès d’Auriac, and J. M. Maillard. Random matrix theory and classical statistical mechanics: Vertex models. *Phys. Rev. E*, 55:5380–5392, May 1997. [73](#)
- [217] Henrik Bruus and Jean-Christian Anglès d’Auriac. Energy level statistics of the two-dimensional hubbard model at low filling. *Phys. Rev. B*, 55:9142–9159, Apr 1997. [73](#)
- [218] T. Guhr, J.-Z. Ma, S. Meyer, and T. Wilke. Statistical analysis and the equivalent of a thoulless energy in lattice qcd dirac spectra. *Phys. Rev. D*, 59:054501, Jan 1999. [73](#)

- [219] V. Paar, D. Vorkapić, K. Heyde, A. G. M. van Hees, and A. A. Wolters. Broken isospin symmetry in the shell model and chaotic behavior. *Phys. Lett. B*, 271(1):1–6, 1991. [73](#)
- [220] Ashraf A. Abul-Magd and Adel Y. Abul-Magd. Unfolding of the spectrum for chaotic and mixed systems. *Physica A*, 396:185–194, 2014. [73](#)



# List of publications

## Published Articles

1. **Mahaveer Prasad**, Hari Kumar Yadalam, Camille Aron, Manas Kulkarni. *Dissipative quantum dynamics, phase transitions and non-Hermitian random matrices* [Phys. Rev. A 105, L050201 \(Letter\), May 2022.](#)
2. **Mahaveer Prasad**, Abhishodh Prakash, Jedediah H. Pixley, Manas Kulkarni. *Long-ranged spectral correlations in eigenstate phases* [Journal of Physics A: Mathematical and Theoretical, 57\(1\):015003, Dec 2023.](#)
3. **Mahaveer Prasad**, Hari Kumar Yadalam, Manas Kulkarni, Camille Aron. *Transition to chaos in extended systems and their quantum impurity models* [Journal of Physics A: Mathematical and Theoretical, 57\(1\):015308, Dec 2023.](#)

## Manuscript in preparation

1. **Mahaveer Prasad**, Ahana Chakraborty, Tom Iadecola, Manas Kulkarni, Jedediah H. Pixley, Sriram Ganeshan and Justin Wilson *Measurement and feedback driven adaptive dynamics in the classical and quantum kicked top*